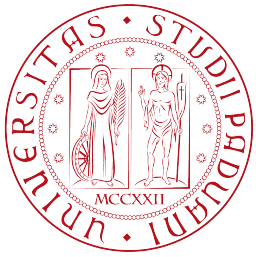

UNIVERSITY OF PADOVA

PADOVA NEUROSCIENCE CENTER

Ph.D. School in Neuroscience - Cycle: XXXIV

Beyond Static Functional Connectivity: Hidden Markov Models to Investigate the BOLD Signal Dynamics in Resting State

---

Candidate:
Manuela Moretto

Headmaster of the school:
Prof. Antonino Vallesi

Supervisor:
Prof. Alessandra Bertoldo

Cosupervisor:
Prof. Maurizio Corbetta

To my family

Life is not easy for any of us, but what of that?
We must have perseverance and above all confidence in ourselves.
We must believe that we are gifted in something, and that this thing, at whatever cost, must be attained.
Marie Curie

Contents

Abstract

In recent years, the neuroscience community has paid growing attention to the study of brain functional connectivity (FC) both in healthy and pathological conditions. FC is defined as a statistical dependency among remote neurophysiological events, and it is typically inferred through the correlations between neuronal activity signals. In the brain, two regions are functionally connected if exists a statistical relationship between their activity.
Many techniques have been introduced in this field to assess such relationship and, among them, the functional Magnetic Resonance Imaging (fMRI) is the most used until now, especially if acquired in resting state (rs-fMRI). Indeed, rs-fMRI has a reduced invasiveness and does not require the cooperation of the patient in performing specific tasks.
Two categories of approaches exist for investigating FC: static and dynamic approaches. Static approaches assess FC between brain regions after averaging the fMRI signal over the entire acquisition scan, usually lasting between 5 and 10 minutes. Dynamic approaches, on the other hand, aim to evaluate the sequence of FC patterns (i.e., brain states) that occur over time and that, typically, have a duration of a few tens of seconds.
Dynamic FC is becoming of paramount importance in this field as it allows to investigate how much the neural dynamics of specific brain areas or networks slow down or up both during the disease and in a healthy brain.
This thesis presents a data-driven framework for the analysis of rs-fMRI data to study FC, using both static and dynamic approaches. Particular emphasis is given to Hidden Markov Models (HMMs), a statistical approach recently introduced for inferring dynamic brain states, which overcomes some limitations of the state-of-the-art approach for dynamic FC analysis based on sliding windows and clustering.
Firstly, to obtain a high spatial resolution functional parcellation of the whole brain in the major RSNs, we applied an independent component analysis on a large group of healthy subjects. This parcellation was then exploited in a static FC analysis to characterize networks alteration in patients with brain tumors at the single-subject level.
Secondly, the parcellation was exploited in a dynamic FC analysis based on HMMs

to study the effects of healthy aging on the dynamics of brain states. After overcoming the model selection problem, we introduced a new index for the quantification of the uncertainty of the model estimates and we performed a graph-based analysis to characterize brain states in terms of integration or segregation of the networks.
Finally, using the developed dynamic analytical framework, we investigated whether brain gliomas can cause alterations in temporal properties of dynamic brain states. The results obtained with HMMs were then compared for validation with the approach based on sliding windows and clustering and showed that HMM is better in separating patients from controls.
The contributions presented in this dissertation provided evidence of the existence of functional alterations in network topography that can occur away from the tumoral area in brain tumors patients and encourage the application of data-driven dynamic FC approaches, as HMMs, to better capture the transitions between brain states at the individual level and characterize clinical populations.

Sommario

Negli ultimi decenni, lo studio della connettività funzionale (FC) nel cervello, in condizioni sia patologiche che sane, ha suscitato sempre più interesse nel campo delle neuroscienze. La FC è definita come una dipendenza statistica tra eventi neurofisiologici remoti, ed è tipicamente valutata attraverso la correlazione tra segnali neuronali di aree cerebrali. Nel cervello, due regioni sono considerate funzionalmente connesse se esiste una relazione statistica tra le loro attività.
Molte tecniche sono state introdotte in questo ambito per valutare tale relazione e, tra queste, la più utilizzata è la Risonanza Magnetica funzionale (fMRI). Attraverso l'impiego di protocolli di acquisizione fMRI in stato di riposo (rs-fMRI), questa tecnica può essere facilmente applicata nella pratica clinica, essendo poco invasiva e non richiedendo la cooperazione del paziente nell'esecuzione di compiti specifici.
La connettività funzionale può essere distinta in statica o dinamica, a seconda dell'approccio che viene usato per valutarla. Gli approcci statici valutano la FC tra regioni cerebrali, basandosi su una media del segnale fMRI sull'intera scansione, solitamente di durata compresa tra i 5 e i 10 minuti. Gli approcci dinamici, invece, sono stati introdotti più recentemente e hanno lo scopo di determinare la sequenza di stati cerebrali che si susseguono nel tempo, ad intervalli di decine di secondi, caratterizzati da specifiche configurazioni di connettività. Lo studio della connettività dinamica sta diventando di fondamentale importanza in questo campo poiché permette di indagare quanto le dinamiche neurali di specifiche aree o reti cerebrali rallentino o aumentino sia in un cervello sano che in uno colpito da una specifica patologia.
In questo lavoro di tesi è stato messo a punto un quadro generale per studiare la FC attraverso approcci sia statici che dinamici, usando dati rs-fMRI. Particolare enfasi è stata data all'applicazione dei modelli di Markov (HMM), modelli statistici che consentono di stimare gli stati cerebrali dinamici e che superano alcune delle limitazioni di quello che è l'approccio più usato in letteratura per l'analisi dinamica della FC.
Inizialmente, per ottenere una parcellizzazione ad alta risoluzione spaziale dell'intero cervello nelle principali reti funzionali, è stata applicata un'analisi di componenti indipendenti su un ampio gruppo di soggetti sani. La parcellizzazione ot-

tenuta è stata poi sfruttata in un'analisi di connettività statica per caratterizzare l'alterazione delle reti funzionali in pazienti con tumore cerebrale e a livello di singolo soggetto.
In secondo luogo, la parcellizzazione è stata usata in un'analisi di connettività dinamica basata su HMM per studiare, in soggetti sani, gli effetti dell'invecchiamento sulla dinamica degli stati cerebrali. Dopo aver affrontato il problema di selezione del modello, abbiamo introdotto un nuovo indice per la quantificazione dell'incertezza delle stime del modello e abbiamo eseguito un'analisi basata su grafi per caratterizzare gli stati cerebrali in termini di integrazione o segregazione delle reti funzionali.
Infine, usando lo schema di analisi sviluppato precedentemente, abbiamo investigato possibili alterazioni di connettività dinamica in pazienti con glioma cerebrale. I risultati ottenuti con HMM sono stati poi confrontati con quelli ottenuti attraverso l'approccio comunemente usato e hanno dimostrato che HMM sono migliori nel separare le dinamiche dei pazienti da quelle dei controlli.
I contributi presentati in questa tesi hanno dimostrato che la topografia delle reti cerebrali funzionali può essere alterata e può verificarsi in aree distanti da quella affetta dal tumore, inoltre incoraggiano l'applicazione di approcci di connettività dinamica, come HMM, per catturare le transizioni temporali tra stati cerebrali a livello individuale e per caratterizzare le popolazioni cliniche.

List of Figures

List of Tables

Acronyms

AIC = Akaike information criterion
ASS = assortativity
AUD = auditory network
avLL = average log-likelihood
BC = betweenness centrality
BIC = bayes information criterion
BOLD = blood oxygen level dependent
CC = clustering coefficient
CCN = cognitive-control network
CON = cingulo-opercular network
CS = cosine similarity
CSF = cerebrospinal fluid
CV = coefficient of variation
DAN = dorsal attention network
dFC = dynamic functional connectivity
DMN = default mode network
EG = global efficiency
EL = local efficiency
FC = functional connectivity
FD = framewise displacement
FE = free energy
fMRI = functional MRI
FO = fractional occupancy
FOV = field ov view
FPN = fronto-parietal network
FRN = frontal network
GM = grey matter
HC = healthy control
HMM = hidden markov model
IC = independent component
ICA = independent component analysis
IDH = isocitrate dehydrogenase gene

LANG = language network network
MRI = magnetic resonance imaging
PCA = principal component analysis
RSN = resting state network
rs-fMRI = resting state functional magnetic resonance imaging
SMN = sensory-motor network
std = standard deviation
STR = strength
SW = sliding window
TE = echo time
TR = repetition time
VB = variational bayes
VIS = visual network
WM = white matter

Chapter 1

Introduction and Motivation

The human brain is a complex machine made up of about 86 billion of neurons and 84 billion of glial cells that cooperate with neurons for the correct functioning of the nervous system (Lent et al. 2012).
Physiological studies have demonstrated that neurons and glial cells are structurally well organized and that communicate with cells of the brain vasculature forming the "neurovascular unit" that enables tight regulation of blood flow (McConnell et al. 2017). Neurons are connected by thousands of links, called "synapses", which are responsible for modulating neuronal function and, more interestingly, can be modified by learning, allowing higher level functions such as adaptation and memory (Mayford, Siegelbaum, and Kandel 2012).
In the last decades, the neuroscience community has begun to focus its research to the study of the mechanisms through which different brain areas are able to communicate together at higher level. In this context, the brain is viewed as a communication system where neural populations interact with each other in an orchestrated manner and pools of neurons cluster together when it's functionally convenient. From a functional perspective, studies in this filed divide the whole brain in functionally sub-regions, each assigned to a specific function as voluntary actions or cognitive tasks.
This research field of neuroscience opened more than 40 years ago, with the seminal work of Legendy (Legéndy 1975) about "brain connectivity", referred to the study of the topological structure of the brain seen as a set of interconnected and functionally homogenous areas. From this first report in 1975, around 77000 articles on PubMed were documented on the brain connectivity topic. Among them, some investigate structural connectivity others functional connectivity between brain areas. Structural connectivity, which forms the connectome, is typically measured in vivo using diffusion tensor imaging (DTI) techniques and concerns the quantification of white matter (WM) tracts physically interconnecting pools of neurons in spatially distant brain regions (Uddin 2013).

On the other hand, functional connectivity (FC), which is usually inferred on the basis of correlations or covariations between neuronal activity signals, is defined as a statistical dependency among remote neurophysiological events (Karl J. Friston 2011). Two brain regions are therefore functionally connected if exists a statistical relationship between their measured activity.
Many techniques have been proposed in the literature for the study of brain connectivity, each of which differs from the other based on the physiological principle observed and on the spatial and temporal resolution that can achieve. These techniques comprise microelectrode array to study electrophysiology at the cell level, electroencephalography (EEG) and magnetoencephalography (MEG) for investigating neuronal electrical activity at high temporal resolution, blood-oxygen-level dependent (BOLD, Ogawa et al. 1990) functional Magnetic Resonance Imaging (fMRI) to study neural activation at high spatial resolution (B. Biswal et al. 1995). The physical principle underlying fMRI is called "neuro-vascular coupling": the local neural activity yields measurable hemodynamic changes by means of blood oxygenation imbalance, ultimately making fMRI a relatively inexpensive and non-invasive indirect neural activity biomarker (Logothetis et al. 2001). Although EEG and MEG give a direct measure of the neural electrical activity, while fMRI an indirect measure of it, the latter is the most employed for investigating FC, probably due to the ease of use of MR scanners in clinical practice.
fMRI allows researchers to study the FC between brain networks during specific tasks or during resting conditions. In fact, the first study of rs-fMRI conducted by Biswal and colleagues in 1995 (B. Biswal et al. 1995) demonstrated the existence of ongoing FC between the left and right somatosensory cortex during rest. Starting from this pioneer study, in the last years, a myriad of groups has used rs-fMRI and proved its utility in describing and characterizing FC alterations in several pathologies, such as Alzheimer's disease (Supekar et al. 2008; Koch et al. 2012), schizophrenia (Bassett et al. 2012; Shen, Wang, et al. 2010), brain tumors (Nenning et al. 2020; Kocher et al. 2020) and stroke (Siegel et al. 2016; Adhikari et al. 2017). In these studies, FC was computed in a "static" way, that is by averaging the BOLD signal over a whole resting state scan and then evaluating the statistical dependencies between BOLD time series derived from different brain regions.
However, recently, the concept of "time-varying" or "dynamic FC" (dFC) has been introduced in the neuroscience filed (R Matthew Hutchison et al. 2013; V. D. Calhoun et al. 2014), referring to the fluctuations of FC over time and even at the temporal scale of seconds. Many methods have been developed to study dFC (Lurie et al. 2020) and among them many attempt to estimate "brain states", that are patterns of FC reoccurring in time and then summarize them through temporal features such as the amount of time spent by each subject in each state

during the resting scan.
The first approach introduced in the literature to discover brain states is based on sliding windows followed by a clustering analysis (Allen et al. 2014) and, because of its simplicity, it has been employed in many studies to characterize brain states in different pathologies such as schizophrenia (Damaraju et al. 2014), multiple sclerosis (Valsasina et al. 2019), autism (Rashid, Blanken, et al. 2018), Alzheimer's and (Jones et al. 2012) Parkinson's (Díez-Cirarda et al. 2018) disease. Although applicable to many clinical populations, it requires the selection of many parameters such as the window size, the window shape, the step size, and the number of clusters (Preti, Bolton, and Van De Ville 2017). To overcome these limitations, the data driven approach of HMM, introduced in the field of rs-fMRI by Vidaurre and colleagues in 2017 (Vidaurre, Stephen M. Smith, and Woolrich 2017), can be employed to explore brain states dynamics. Defined in a statistical framework, it allows the choice of the optimal model order by monitoring the cost function defined in this context called free energy (FE). Although this method is mathematically complex and computationally demanding, the features that can be extrapolated from the states have been shown to well separate healthy from clinical populations, such as in multiple sclerosis (Van Schependom et al. 2019), schizophrenia (Kottaram et al. 2019) and disorder of consciousness (Cao 2019). However, in all these recent studies employing HMM, standard features have been extrapolated from the states, but in none of them a deeper characterization of the FC patterns of states through graph-based analysis to quantify integration or segregation of the networks has been performed.

1.1 Aim

The aim of this thesis was to develop a data-driven framework for dynamic functional connectivity analysis of fMRI data acquired in resting state, based on HMMs. To this scope, we firstly developed a high spatial resolution functional parcellation of resting state networks (RSNs) from and independent component analysis (ICA) covering the whole brain. To verify its suitability for the study of neurological disease, the obtain parcellation was exploited in a static FC analysis of patients with brain tumors. Hence verified it, the parcellation was employed in a dynamic FC analysis based on HMMs, where the time courses of the ICs served as input for the model. In particular, HMMs were applied to two different clinical studies: the first, presented in chapter 4, concerns healthy aging, whereas the second, presented in chapter 5, concerns brain tumors and, in particular, here we analyzed an extended pool of patients previously employed in the first static FC study. Several aspects were faced during these studies, ranging from the selection of the number of components to the implementation of methods to assess func-

tional alterations in the first study and from the selection of the optimal model order to the quantification of the accuracy of the parameter estimates in the last two studies of dynamic FC.

1.2 Thesis Contributions and Outline

In the following list a brief description of the topics covered by each chapter and the contributions is reported.

- **Chapter 1: Introduction and Motivation**
  This current chapter provides an introductory overview and motivation for the studies described in this dissertation.

- **Chapter 2: Functional Magnetic Resonance Imaging**
  This chapter introduces the principles of rs-fMRI. Methods for the analysis of FC will be presented, distinguishing between static and dynamic approaches. In particular, a detailed description of two main methods that have been employed in the studies presented in this dissertation will be provided.

- **Chapter 3: Alterations of static functional connectivity in brain tumors patients**
  This chapter studies the alterations of RSNs in patients suffering from brain tumors through a static FC analysis. After applying the data-driven method based on ICA we obtained a spatial high-resolution template of the networks, starting from rs-fMRI data. This template will be exploited for the analysis conducted in chapters 4 and 5.
  The purpose and contribution of this chapter is to provide an approach that is able to detect at the single subject level, the functional alterations that a brain tumor can cause. Compared to previous studies, we did not limited the observation to specific networks, but we performed a whole-brain characterization of them, giving a 360-degree view of what happens in the brain. Secondly, this chapter wants to demonstrate the existence of functional alterations in network topography that can occur away from the tumor core or the edema, with regions in the cortex near the lesion that are potentially preserved.

- **Chapter 4: Brain states functional dynamics in healthy aging**
  This chapter builds upon the limitations of static FC approaches in capturing the dynamics of the fMRI signal that occur even in resting conditions. The purposes of this chapter are: 1) to overcome the limitations of commonly used approaches for dynamic FC analysis by employing HMMs; 2)

to apply the proposed method for differentiating young from elderly people on the basis of brain states features. The contribution of this chapter is, in addition to applying this approach to healthy aging for the first time, to introduce a new index for the quantification of the uncertainty of the estimates. With the analyses performed in this chapter, we demonstrate the sensitivity of HMM in decoding the whole-brain dynamics of FC and in capturing the individual transitions between brain states. We also show that old subjects tend to persist in states characterized by a general increase of integration between networks.

- **Chapter 5: Dynamic FC in patients with high-grade gliomas**
  In this chapter, by applying HMM, we investigate whether brain gliomas can cause alterations in temporal properties of dynamic brain states. To this end we exploit the template of independent components obtained in the study presented in chapter 3 and the analytical framework developed in chapter 4.
  The contributions of this chapter are mainly two: 1) to apply, to our knowledge for the first time, a dynamic connectivity approach to characterize functional dynamics in patients with brain tumor; 2) to compare the results obtained through HMM with a second approach based on sliding windows+clustering. We demonstrate that patients tend to persist in few dynamic brain states compared to healthy controls and that, these states, are characterized by an overall decrease of connectivity. Moreover, HMM is better in separating patients from controls than the approach based on sliding windows+clustering.

- **Chapter 6: Conclusions**
  This final chapter summarizes the dissertation contributions discussing the perspectives of studied topics.

Chapter 2

Functional Magnetic Resonance Imaging

Our brain is a very efficient network that controls all the complex functions in the human body.
From a functional point of view the brain is organized in subspecialized areas that work together to enable body functions and human behavior.
When a brain area is required to be active for a particular function, neurons inside it are provided with more energy by the adjacent capillaries through a mechanism called the hemodynamic response, which supplies them with increased regional cerebral blood flow and oxygen (Ogawa et al. 1990). This process causes a change in the levels of oxyhemoglobin and deoxyhemoglobin that can be detected by MRI on the basis of their different content of iron and thus in their magnetic susceptibilities.
The imaging technique based on this phenomenon is called fMRI. The change in the BOLD signal is the cornerstone of fMRI (Ogawa et al. 1990; Kwong et al. 1992) which was initially used to visualize brain regions that are activated during specific tasks (Chee et al. 1999; Schlosser et al. 1998; LaBar et al. 1999; Banich et al. 2000).

2.1 Resting-state fMRI

Some years after the invention of fMRI, studies started to investigate the possibility of measuring spontaneous fluctuations of BOLD signal recorded during rest, through the so called resting state fMRI (B. B. Biswal, Kylen, and Hyde 1997; Greicius et al. 2003; Lowe et al. 2000). The frequencies of neural activity fluctuations measured by rs-fMRI are at low-frequency (0.01-0.1Hz) and indirectly measured using BOLD signal.
The functional significance of these fluctuations was first demonstrated by Biswal

and colleagues in 1995 (B. Biswal et al. 1995). During their rs-fMRI study, volunteers were told to relax and not to perform any cognitive, language, or motor tasks, while their level of spontaneous brain activity was measured throughout the period of acquisition.
The authors found that the BOLD time-series of the left somatosensory cortex were highly correlated with those of the homologous areas in the contralateral hemisphere, suggesting ongoing information processing and ongoing FC between these regions during rest. The existence of synchronous spontaneous fluctuations between primary and higher order somatosensory regions was further confirmed by later studies (B. B. Biswal, Kylen, and Hyde 1997; Cordes, V. M. Haughton, et al. 2000; Beckmann et al. 2005).
The use of rs-fMRI has allowed the identification of many RSNs, which are spatially distinct areas of the brain that demonstrate synchronous BOLD fluctuations at rest. Among these networks, the default mode network (DMN) was the first identified in resting conditions by Raichle et al. (Raichle et al. 2001). In their study, the authors performed a Positron Emission Tomography (PET) study and analyzed data of healthy volunteers in resting conditions. They found that coherent regions in the brain were active at rest but decreased their activity during cognitive tasks. The DMN was later identified by Greicius et al. (Greicius et al. 2003) by using fMRI and confirmed in many other studies by using a variety of analysis approaches. Based on these findings, studies have hypothesized that there are two opposing systems in our brain: one including the DMN ("intrinsic system") and the other composed of attentive or task-based systems, such as somatosensory, visual, or attention networks ("extrinsic system").
There are several ways to pre-processed the BOLD signal before applying any analysis method. Standard pre-processing steps generally include slice-timing correction and data normalization. This are followed by regression of head motion and other nuisance regressors, such as the signal of regions located in the ventricles and WM, which are thought to include high proportions of noise related to cardiac and respiratory signals (Dagli, Ingeholm, and Haxby 1999; Munck et al. 2008). Finally, a band-pass filter in the 0.01-0.1Hz band is often applied to help removing non-neuronal causes from the signal.
After these pre-processing steps, many methods can be used to analyze rs-fMRI data and, in particular, to investigate the existence of functional connections between spatially distant brain regions (i.e., the functional connectivity) and in many review articles (M. P. v. d. Heuvel and H. E. Hulshoff Pol 2010; Lv et al. 2018; M. Lee, Smyser, and Shimony 2013), they are briefly described, highlighting advantages and limitations of each. In the next section, we provide a brief overview of some of the most employed methods used to explore FC among brain areas.

2.2 Methods to assess FC

Functional connectivity is defined as the statistical dependency of neuronal activation patterns of anatomically distant brain regions (Karl J. Friston 2011).
There are several methods to assess FC between brain regions, including seed methods (Andrews-Hanna et al. 2007; B. Biswal et al. 1995; Cordes, V. M. Haughton, et al. 2000; Fransson 2005; M. Song et al. 2008), principal component analysis (PCA) (K. J. Friston et al. 1993), singular value decomposition (Worsley et al. 2005), independent component analysis (ICA) (Beckmann et al. 2005; V. Calhoun et al. 2001; Ven et al. 2004), clustering (Martijn van den Heuvel, Mandl, and H. Hulshoff Pol 2008; Cordes, V. Haughton, et al. 2002; Salvador et al. 2005; Thirion, Dodel, and Poline 2006) and graph-based analysis (Bullmore and Sporns 2009).
In the next paragraphs we will briefly introduce the most commonly employed methods for FC analyses, that are the seed-based, the ICA, the clustering and the graph-based analysis.

2.2.1 Seed-based FC

Seed-based FC consists in the computation of the correlation between the time-series of the depicted seed region and the time-series of all other regions. The coupling of neural activation between different brain regions indicates that they are involved in the same functional process and thus interpreted as functionally connected (B. B. Biswal, Kylen, and Hyde 1997; Cordes, V. M. Haughton, et al. 2000). Several metrics (e.g., cross-correlation coefficient, partial correlations) can be used to assess associations between time-series of brain regions.
The seed region can be a single voxel/vertex or a region defined a priori by an atlas or it can be selected from a task-based activation map acquired in a separate fMRI session. If the seed region is a ROI defined a priori for example, from a functional atlas (e.g., Thomas Yeo et al. 2011; Gordon et al. 2016), the FC is better known as ROI- or atlas-based FC.
The connectivity between brain areas can be visualized using a FC map that defines the strength of all functional connections between seed regions within the brain.
The advantage of this analysis is its relative simplicity, together with the immediate interpretation of the results. In fact, FC maps provide a clear view of the functional connections between the seed region and the other brain areas. However, the information of a FC map computed at the voxel/vertex level is limited to the connections of the selected seed region, making it difficult to investigate functional connections patterns on a whole-brain level. Furthermore, another disadvantage of seed analysis is that its results could be biased by the selection

of the seed region.

2.2.2 Data-driven FC methods: ICA and clustering

Compared to model-dependent methods, model-free methods enable to explore FC patterns without the need of defining an a priori seed region.
ICA consists in the separation of the BOLD signal into several sources or independent components (ICs), maximally independent from each other, in the form of spatial maps, which are temporally correlated (Beckmann et al. 2005; Kiviniemi et al. 2003). After performing an ICA, the resulting ICs can be classified as noise or networks of neurons with synchronized BOLD activity (Griffanti et al. 2014). The result of and ICA is a spatial map of the z-scores derived from the correlation between the time-series of each voxel and the mean time-series of one specific network. The average z-score for each IC indicates the magnitude of connectivity within the network.
Several RSNs commonly emerge from an ICA, including the sensory-motor network (SMN), auditory network (AUD), cingulo-opercular network (CON), dorsal attention network (DAN), fronto-parietal network (FPN), default mode network (DMN), cognitive-control network (CCN), frontal network (FRN), language network (LANG), cerebellar network (CER) and basal ganglia network (BG) (Beckmann et al. 2005; Shirer et al. 2012).
While seed analysis performed at the voxel-level extracts only the regions functionally connected to the ROI, ICA extracts all detectable networks within the subject. ICA can be performed without any a priori assumptions, except the selection of the number of ICs to identify.
A possible disadvantage of ICA might include that it only presents the spatial patterns of the brain areas involved in a specific network without easily allowing an investigation of the single brain nodes composing it. Additional issue is that a single network could be broken into several sub-networks, depending on the number of ICs specified by the user.
Another data-driven approach is clustering. It consists in grouping data into sub-groups, where the similarity between data is maximal (Salvador et al. 2005). Thus, clustering results may be more easily comparable to ROI-based FC maps, as they more directly reflect functional connections between brain regions.
One example of a clustering algorithm is hierarchical clustering (Salvador et al. 2005; Cordes, V. Haughton, et al. 2002) which builds a dendrogram of all members. Another clustering algorithm that group together data on the basis of their distances from the cluster centers or centroids, is called 'K-means' (Golland et al. 2008). This algorithms iterates to update memberships and cluster centers until convergence is achieved.
Although seed-based analysis, ICA and clustering analysis are based on different

mathematical principles, they tend to show a high level of overlap between their results. For example, studies employing group ICA have consistently reported the formation of the DMN during rest (Beckmann et al. 2005; J. Damoiseaux et al. 2008; J. S. Damoiseaux et al. 2006), which have been extensively confirmed by both seed-based (Greicius et al. 2003; Whitfield-Gabrieli et al. 2009) and clustering approaches (M. van den Heuvel et al. 2008; Martijn van den Heuvel, Mandl, and H. Hulshoff Pol 2008).

2.2.3 Graph-based FC

Graph based analysis provides a theoretic framework for studying the topology of brain networks by examining both the local and global organization of neural networks (Bullmore and Sporns 2009; Sporns, Honey, and Kötter 2007).
In graph theory, RSNs can be defined as a graph (G) consisting of a pair of two sets: N, the set of nodes, and L, the set of links/edges connecting pairs of nodes. G is thus seen as a function of V and E: *G=f(N,E)*. The elements of N=$n_1, n_2, ...n_M$ represent the fundamental units of the system, while the elements of L=$l_1, l_2, ...l_K$ represent the connections between pairs of nodes that is, the relationships between the elements of the system. M is the number of nodes and indicates the dimension of the graph, whereas K is the number of the edges in the system. A node is identified by its $i-th$ position, while a link (l_{ij}) is defined by a pair of connected nodes i and j.
Using rs-fMRI data, nodes may represent voxels or ROIs or ICs, and edges the functional connectivity between two nodes. A graph representation of the functional brain network is constructed using a predefined cutoff threshold of E.
On the basis of the intensity of the connections between nodes, two categories of links can be distinguished:

- **unweighted/binary link**: specify the state of connection between two nodes, expressed as the presence or absence of the link. A value of 1 indicates the presence of the connection, 0 indicates the absence of the link between two nodes. Consequently, all the links are equally important.

- **weighted/binary link**: each edge is assigned a real number w_{ij} which determines its weight, i.e. the strength of the connection between two nodes.

Thus, on the basis of this classification, a graph can be defined "unweighted" or "weighted".
For each graph, we can quantify many measures, each of which can represent one of these four categories:

- **Measures of elasticity**: quantify the anatomical characteristics that reflect the vulnerability of the system to external perturbations.

- **Measures of centrality**: analyze the role that some nodes assume within the network, classifying them according to the centrality that they hold in the management of signal transmission between one region and another of the network.
- **Measures of integration**: quantify the efficiency of the system in the global transmission of information, even between distant nodes.
- **Measures of segregation**: quantify the tendency of nodes to cluster together in networks populated by nodes that are strongly interconnected with nodes in the same network and poorly with nodes outside the network.

Examples of key measures which can be derived from a graph-based analysis and used in this work of thesis are listed below.

- **Degree** (DEG) is the number of connections of a node. It helps identify the highly connected nodes within the network.

$$DEG = \sum_{j \in N} a_{ij}$$

  where a_{ij} identifies the presence/absence of connections between node i and node j.

- **Strength** (STR) is a measure of elasticity and computed as the sum of weights of links connected to the node i.

$$STR = \sum_{j \in N} w_{ij}$$

- **Betweenness Centrality** (BC) is a measure of centrality and defined as the fraction of all shortest paths in the network that contain a given node. Nodes with high values of BC participate in a large number of shortest paths.

$$BC = \frac{1}{(M-1)(M-2)} \sum_{h,j \in N} \frac{\rho_{hj}(i)}{\rho_{hj}}$$

  where ρ_{hj} is the shortest path connecting h and j, while $\rho_{hj}(i)$ is the shortest path passing through h and connecting i and j.

- **Characteristic path length** (CPL) is a measure of integration and describes the average number of connections between all pairs of nodes. It reflects the global connectivity of the network, which reflects the efficiency of the network.

$$CPL = \frac{1}{M-1} \sum_{i,j \in N, j \neq i} d_{ij}$$

where d_{ij} is the length of the shortest path between i and j. If the graph is weighted, d_{ij} is the weighted distance.

- **Global efficiency** (EG) is a measure of integration, defined as the average inverse shortest path length in the network.

$$EG = \frac{1}{M(M-1)} \sum_{i,j \in N, j \neq i} d_{ij}^{-1}$$

- **Local efficiency** (EL) is a measure of segregation and defined as the global efficiency computed on the neighborhood of the node.

$$EL = \frac{1}{M} \sum_{i \in N} EG_i$$

where EG_i is the global efficiency of the sub-graph composed of the neighbors of node i.

- **Clustering coefficient** (CC) is a measure of segregation and describes the level of local neighborhood clustering. It reflects the level of local connectedness of a network.

$$CC = \frac{1}{M} \sum_{i \in N} \frac{2t_i}{k_i(k_i - 1)}$$

where t_i is the number of triangle in the system in which the node i is one of the vertices, on all the N nodes of the graph G.

- **Modularity** is a measure of segregation and describes the extent to which groups of nodes are connected to the members of their own group. It reflects the existence of subnetworks within the full network.

$$MOD = \frac{1}{K} \sum_{i,j \in N} (a_{ij} - \frac{DEG_i DEG_j}{K}) \delta_{m_i, m_j}$$

where m_i is the module containing the node i, $\delta_{m_i,m_j} = 1$ if $m_i = m_j$. In a weighted graph, the degree is replaced with the strength.

- **Assortativity** (ASS) is a correlation coefficient between the degrees of all nodes on two opposite ends of a link. The assortativity of a graph ranges between -1 and 1. A positive assortativity indicates that nodes tend to link to other nodes with the same or similar degree. A coefficient of -1 indicates that there is very low likelihood of two vertices with the same property

being connected.

$$ASS = \frac{\frac{\sum_{i,j\in N, i\neq j} STR_i STR_j}{K} - (\frac{\sum_{i,j\in N, i\neq j} 0.5(STR_i + STR_j)}{K})^2}{\frac{\sum_{i,j\in N, i\neq j} 0.5(STR_i^2 + STR_j^2)}{K} - (\frac{\sum_{i,j\in N, i\neq j} 0.5(STR_i + STR_j)}{K})^2}$$

In Figure 2.1 a depiction of these metrics is reported.

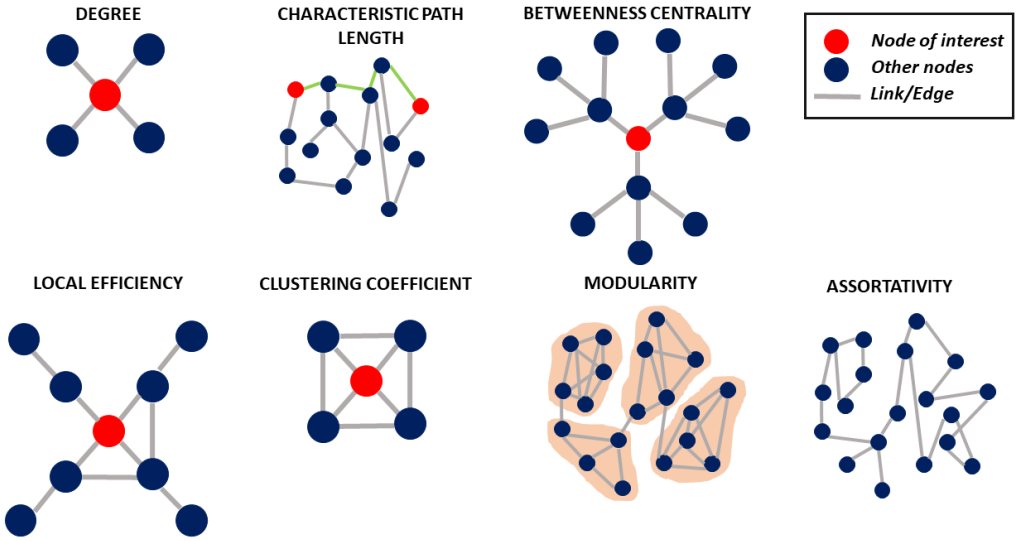

Figure 2.1: The figure depicts some of the graph measures described in the previous paragraph.

2.2.4 Differences between static and dynamic FC

FC analyses performed on rs-fMRI data allow the non-invasive investigation of neural interactions among functionally connected brain regions.
FC can be defined as "static" or "dynamic" on the basis of the type of approach adopted to compute it.
The underlying assumption of static approaches is that the connectivity among brain regions does not vary over time. Thus, static FC is calculated over a whole resting state scan of six minutes or more and, usually, it is computed as the correlation between the average time series derived from regions or networks.
On the contrary, “time-varying” or “dynamic FC” (dFC) is based on the assumption that FC fluctuates over time and even at the temporal scale of seconds. In this context, dFC cannot be evaluated as a simple average of the BOLD signal over the entire MR acquisition, but instead, requires the introduction of more sophisticated methods that we will introduce in the next section.

2.3 Dynamic FC

In the last years growing interest has been shown in studying fluctuations of FC over time (**dFC**, (R Matthew Hutchison et al. 2013; V. D. Calhoun et al. 2014)). Since the initial findings (Chang and Glover 2010), a large body of research has begun to develop methods for studying dFC. These methods can be divided into two branches (Lurie et al. 2020): methods that explicitly model the neural processes underlying changes in the observed BOLD data and methods that attempt to estimate changes in FC and/or identify FC states directly from the observed BOLD data.
Below, we provide illustrative examples of each of the two approaches.

2.3.1 Model-driven methods

This family of approaches aims to model the underlying neural fluctuations and interactions that give rise to dFC. The assumption underlying these approaches is that the observed BOLD time series are generated by nonlinear brain dynamics that are then corrupted by measurement noise.
Under this perspective, activity in large-scale neural systems is dynamic and these dynamics can be mathematically modeled by biophysical differential equations (Deco et al. 2008). Through the combination of mathematical equations with models describing the observational process (e.g., neurovascular coupling), it is possible to simulate how these underlying dynamics would manifest in the BOLD signal.
There is a large number of multiscale models describing interconnected pools of neurons, including neural mass and mean field models (Bojak et al. 2010; Breakspear 2017; Deco et al. 2008). Multiscale models can be used as generative models or as observation models, which are inverted given empirical data. Observational models can reproduce excitatory and inhibitory processes within a node. The resulting simulated neural activity can be converted into a FC that can then be compared with the empirical functional data to assess the predictive power of the model.
These models have shown to produce neural system-like behaviors such as generalized synchronization, metastability, and multistability (Breakspear 2017; Deco et al. 2008; Golos, Jirsa, and Daucé 2015; Heitmann and Breakspear 2018).
In summary, model-driven methods provide a rich parameterization to enable explicit investigation of how networks of neurons, modeled for example as populations of spiking neurons, may give rise to the observed BOLD signal.

2.3.2 Data-driven methods

This family of techniques typically aims to identify the time-resolved dependencies occurring between fMRI time series.
The most widely used approach belonging from this family is the so called "sliding window" (SW) (Sakoğlu et al. 2010). It consists in segmenting the time courses into a set of temporal sliding windows of length W, inside which their pairwise correlations is computed, resulting in time resolved correlation matrices.
Other methods estimate instantaneous FC in a time-frequency fashion exploiting phase synchrony (Chang and Glover 2010; Pedersen et al. 2018; Yaesoubi et al. 2015).
A common next step of data-driven methods is to summarize the temporal properties of the resulting time-resolved FC estimates, for example through the use of descriptive statistics (e.g., variance (Chang and Glover 2010; Kucyi, Salomons, and Davis 2013)) or through methods that attempt to identify FC brain "states" (i.e., transient patterns of whole-brain FC).
Methods for identifying brain states include sliding windows + clustering (Allen et al. 2014) and Hidden Markov Models (Shappell et al. 2019; Vidaurre, Stephen M. Smith, and Woolrich 2017). After identifying states, it is possible to estimate a variety of parameters such as mean fractional occupancy within a state, transition probabilities between states, and graph theoretic measures that describe the observed FC patterns.

There is no a best method for studying dFC: the choice depends on the available data and on the particular research question one wants to answer. Different approaches provide different perspectives on the data and the integration of them could provide a full understanding of the factors giving rise to dFC and its relationship with cognition and behavior.
Model-based approaches seek to model the biophysical parameters directly, while data-driven approaches make minimal or no explicit assumptions about the underlying biology. By improving the biological specificity, the model complexity as well as the model assumptions increases. Methods that directly model the observed BOLD signal can nonetheless be highly statistically articulated and are based on their own assumptions that are often as strong as assumptions made by biophysical models (Lurie et al. 2020).
Highly articulated data-driven methods, such as HMMs, may explain the data very well without recourse to biological assumptions, but do not provide information about the underlying neuronal dynamics without additional parameterization.
Since in this work of thesis we were interested not so much in exploring how networks of neurons give rise to the observed BOLD signal, but rather in applying data-driven methods to better exploit the information derived from the data at

disposal for studying populations that have not yet been studied from the perspective of dFC, we will focus on two data-driven methods for identifying brain states. In the next paragraphs we will introduce the advantages and disadvantages of both methods employing in the studies presented in the next chapters and discuss their applications.

Sliding windows + clustering

SW followed by K-means clustering allows the identification of recurring FC patterns (cluster centroids) of correlation or anti-correlation between brain regions and are mutually exclusive in time. This approach was introduced by Allen and colleagues (Allen et al. 2014) and subsequently adopted by other groups (Damaraju et al. 2014; Barttfeld et al. 2015; Gonzalez-Castillo et al. 2015; R. Matthew Hutchison et al. 2014; Shen, Li, et al. 2016; Rashid, Eswar Damaraju, et al. 2014). This approach has been widely used in many clinical populations (see Valsasina et al. 2019 for a review) such as schizophrenia (Damaraju et al. 2014), multiple sclerosis (d'Ambrosio et al. 2020), autism (Rashid, Blanken, et al. 2018), mild traumatic brain injury's (Vergara et al. 2018) and Parkinson's disease (Díez-Cirarda et al. 2018). In these clinical studies the number of subjects varied between 59 to 920, the TR between 2 and 3s, the total number of volumes per subject between 100 and 250 and the number of clusters identified between 2 and 5.
Besides its simplicity, this technique has some drawbacks. The most important to consider is the choice of the window length W. In fact, W too short could increase the risks of introducing spurious fluctuations in the observed dFC (R Matthew Hutchison et al. 2013; Leonardi and Van De Ville 2015; Zalesky and Breakspear 2015) and of having too few samples for computing the correlation in a reliable way, while, on the other hand, W too long could prevent the detection of FC temporal variations. Thus, a trade-off must be reached to keep both the specificity and sensitivity.
Commonly employed values for the window lengths range between 30 and 60s, the step size is fairly variable across studies but in many articles a step size equal to the window size was used and the number of data points per window varies between 20 and 100 in most studies (Preti, Bolton, and Van De Ville 2017).
However, until now there is no clear indication on the window length and step size which would best suit each analysis and the choice remains arbitrary.

Hidden Markov Model

HMM uses temporally concatenated rs-fMRI data to determine, in a full probabilistic approach, the time-varying neural processes represented as a sequence of brain states and their transition over time. A graphical representation of a HMM

is displayed in Figure 2.2.
An HMM is characterized by the following elements:

1. K, the number of hidden states in the model, where K must be set a priori. We denote the individual states as $S = S_1, S_2, ..., S_K$ and the state at time t as q_t. The states constitute the hidden layer of the model.

2. The state transition probability distribution Θ_{ij} where

$$\Theta_{ij} = P[q_{t+1} = S_j | q_t = S_i], \qquad 1 \leq i, j \leq K \tag{2.1}$$

   that describes how likely is to be in specific state j at time point t+1, if we were in state i at time point t.

3. The observation probability distribution in state l, $B = b_l(k)$ where

$$b_l(k) = P[q_t = S_l], \qquad 1 \leq l \leq K \tag{2.2}$$

4. The initial state distribution $\pi = \pi_i$ where

$$\pi_i = P[q_1 = S_i], \qquad 1 \leq i \leq K \tag{2.3}$$

Given appropriate values of K, Θ, B, π, the HMM can be used as generator of an observation sequence (the observational layer of the model)

$$X = X_1 X_2 ... X_T \tag{2.4}$$

(where T is the number of observations in the sequence), as follows:

- Choose an initial state $q_1 = S_i$ according to the initial state distribution π.
- Set t=1.
- Choose X_t according to the symbol probability distribution in state S_i, i.e., $b_i(k)$.
- Transit to a new state $q_{t+1} = S_j$ according to the state transition probability distribution for state S_i, i.e., Θ_{ij}.
- Set t=t+1; return to step 3)if t<T; otherwise terminate the procedure.

The procedure described above can be used as both a generator of observations and as a model for how a given observation sequence was generated by an HMM (Rabiner 1989).

A complete specification of an HMM requires the specification of the model parameters and the specification of three probability measures Θ_{ij}, B, π.
Different families of probability distributions can be employed to model the observations (Rezek and Roberts 2005). Here we briefly describe one of the most used for modeling rs-fMRI data (Vidaurre, Stephen M. Smith, and Woolrich 2017) and that was used in chapters 4 and 5 that is the multivariate Gaussian distribution. Under this assumption, the probability of observing the data at time point t (X_t) given a certain state k at time point t, follows a multivariate Gaussian distribution:

$$P(X_t|q_t = S_k) \sim N(\mu_k, \Omega_k) \tag{2.5}$$

where μ_k is a vector ([M×1], M=number of regions) containing the mean BOLD activation and Ω_k is a matrix ([M×M], M=number of regions) containing the precision. From the inversion of the precision matrix Ω_k, the covariance matrix Σ_k, codifying the variances and covariances between regions when state k is active, can be assessed.

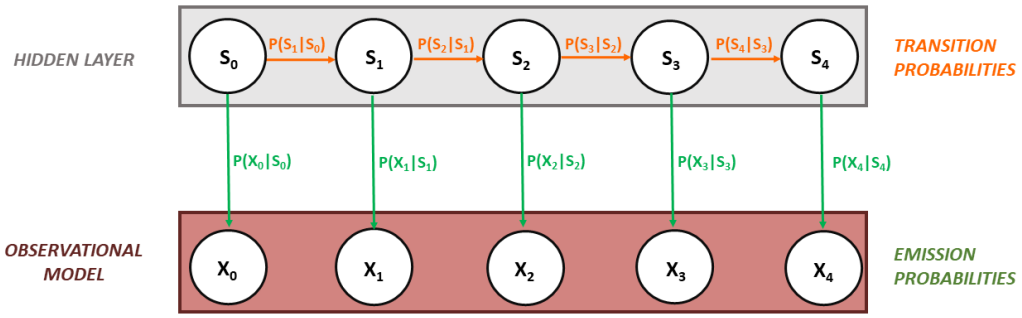

Figure 2.2: The figure represents the structure of a HMM with five states.

Parameters estimation

The parameters that need to be estimated are those defining the posterior distribution of each state (μ_k and Ω_k) and the three probability measures (Θ_{ij}, B, π) described above.
The most established method of training the parameters of an HMM uses the maximum-likelihood framework. However, models with many parameters cannot be computed without running into computational problems, such as near-singular covariance matrices. A model with many parameters is, for example, an HMM in which the observations are the BOLD signals of M brain regions.
An alternative framework for parameters estimation is the Bayesian one. A Bayesian estimator results in a distribution for the HMM parameters, which is known as the posterior. In computing this distribution, the estimator requires the

likelihood of the data under the model and the prior distributions of the model parameters:

$$P(\theta|x) = \frac{P(x|\theta)P(\theta)}{\int P(x|\theta)P(\theta)d\theta} \tag{2.6}$$

Unfortunately, for complex models there is not a closed-form, analytical solution for the values of these parameters given the data. On these grounds, the variational Bayes (VB) framework, which assumes additional factorization in the space of parameters and needs all prior distributions to be conjugate (Bishop 2006) can be used. Through an iterative algorithm that acts on one group of parameters at a time, the variational inference minimizes the cost function of the model called free energy (FE) (Rezek and Roberts 2005). This VB approach infers the parameters of the model alternating a variational expectation-step and maximization-step (Bishop 2006). The first step deals with the estimation of the hidden states probabilities (Θ_{ij}, B, π) and the second step estimates the model parameters (μ_k and Ω_k).
All the variational updating equations for the parameters are reported in (Vidaurre, Quinn, et al. 2016).
The convergence is guaranteed for this kind of algorithms and can be monitored by means of the FE.
The aim of the VB inference is, in fact, to minimize the FE, which includes three terms: the average log-likelihood (avLL, i.e., how well the model fits the data), the Kullback–Leibler divergence (how divergent are the approximate posterior distributions from the priors) and the negative entropy, computed for the distribution of the hidden states. The general formulation of the FE is described by the following formula:

$$FE = -\int q(S)q(\theta)logP(X,S|\theta)dSd\theta + \int q(S)logq(S)dS + \int q(\theta)log\frac{q(\theta)}{P(\theta)}d\theta \tag{2.7}$$

where the first term represents the avLL, the second term the Kullback–Leibler divergence and the last terms the negative entropy. P and Q are two densities, which have parameters indexed by q and p, θ is the set of model parameters and S the set of hidden state variables. Given the non-linear nature of the VB approach, which may lead to never reaching a global minimum of the cost function, it is better to make many realizations of the model and then chose the one with the lowest value of FE.
The FE is a trade-off between precision in representing the data and complexity; so it is an information criterion and not a biological criterion.

Parameter initialization

The expectation-maximization algorithm needs an initial estimation for the states

probabilities, which can be performed in two ways. The first one is to employ a mixture of Gaussian model, which can be itself initialised with a K-nearest neighbour algorithm. The second, is to run the entire HMM variational inference procedure a number of times, using random initialization and a low number of variational iterations, so that the one with the lowest free energy is then used as a starting point of an inference run that is eventually allowed to converge. Since there is not a best option to perform the initialization, a reasonable possibility is to try all different initialization, choosing the one with the best FE.

Prior distributions

To obtain approximate solutions for the posterior distributions, the prior distributions are required to be conjugate distributions. The approximate posterior distributions will then be functionally identical to the prior distributions (i.e. a Gaussian prior density is mapped to a Gaussian posterior density).

Referring to the implementation of the model described in (Vidaurre, Quinn, et al. 2016), which was employed for the studies presented in chapters 4 and 5, these prior distributions are assumed:

-K-dimensional Dirichlet density for the initial state probability π.

-K×K - dimensional Dirichlet densities for the transition probabilities Θ_{ij}.

-A multivariate gaussian distribution for the observations conditionate on the state. In particular, N-dimensional normal densities for the mean activation μ_k and N-dimensional Wishart densities for the precision matrix Ω_k.

Model selection

The FE can also be used for model selection purposes (Rezek and Roberts 2005). Indeed, after running the HMM for different model orders, the optimal one can be chosen as that minimizing the FE. In this way, HMM overcomes the limitations of SW + clustering approach regarding the selection of the optimal window size and clustering dimensionality, given that the model order can be chosen quantitatively.

Model outputs

After the model inference, many quantities of interest can be evaluated. On of these can be retrieved by $\gamma_t(i)$, defined as the probability of being in state S_i at time t, given the observation sequence and the model. Indeed, by summing $\gamma_t(i)$ over time, we get a quantity, Γ which can be interpreted as the expected (over time) number of times that state S_i is visited, or equivalently, the expected number of transitions made from state S_i:

$$\Gamma = \sum_{t=1}^{T-1} \gamma_t(i) \tag{2.8}$$

Another quantity of interest, computed through the Viterbi algorithm (Viterbi

1967) is the Viterbi path, that is the best sequence of the states, $Q = q_1, q_2, ..., q_T$, for the given observation sequence $X = X_1, X_2, ..., X_T$. In order to compute it, the following quantity must be defined:

$$\delta_t(i) = \max_{q_1,q_2,...q_{t-1}} P[q_1 q_2 ... q_t = i, X_1 X_2 ... X_t | \lambda] \tag{2.9}$$

where λ is the set of states probabilities (Θ_{ij}, B, π). $\delta_t(i)$ thus represents the highest probability along a single path, at time t, which accounts for the first t observations and ends in state S_i. By induction we have:

$$\delta_{t+1}(j) = [\max_i \delta_t(i)\Theta_{ij}]b_j(X_{t+1}) \tag{2.10}$$

To retrieve the state sequence, we need to keep track of the argument which maximized eq. 2.10, for each t and j. This can be done through $\psi_t(j)$. The complete procedure for finding the best state sequence of states, can now be stated as follows:

1. Initialization:

$$\delta_1(i) = \pi_i b_i X_1, \qquad 1 \leq i \leq K \tag{2.11}$$

$$\psi_1(i) = 0 \tag{2.12}$$

2. Recursion:

$$\delta_t(j) = \max_{1\leq i\leq K} [\delta_{t-1}(j)\Theta_{ij}]b_j X_t, \qquad 2 \leq t \leq T, 1 \leq j \leq K \tag{2.13}$$

$$\psi_t(j) = \operatorname*{argmax}_{1\leq i\leq K} [\delta_{t-1}(i)\Theta_{ij}], \qquad 2 \leq t \leq T, 1 \leq j \leq K \tag{2.14}$$

3. Termination:

$$P^\star = \max_{1\leq i\leq K} [\delta_T(i)] \tag{2.15}$$

$$q_T^\star = \operatorname*{argmax}_{1\leq i\leq K} [\delta_T(i)] \tag{2.16}$$

4. Path (state sequence) backtracking:

$$q_t^\star = \psi_{t+1}(q_{t+1}^\star), \qquad t = T-1, T-2, ..., 1 \tag{2.17}$$

Applications

Although its mathematical complexity, in recent years, HMM has been applied for characterizing brain states in healthy subjects during rest (Vidaurre, Stephen M. Smith, and Woolrich 2017) and tasks (Vidaurre, Abeysuriya, et al. 2018), as well as in clinical populations (Cao 2019; Kottaram et al. 2019; Van Schependom et al. 2019), demonstrating its ability to exploit and summarize the richness of

the rs-fMRI data. The number of brain states identified by a model selection procedure or a-priori fixed in these studies ranges between 8 and 16.

Chapter 3

Alterations of static functional connectivity in brain tumors patients

3.1 Introduction

In this chapter we introduce a study of static FC to assess resting state functional alterations in brain tumors patients compared to healthy controls (HCs). The analyses were performed at the whole brain level and in particular using the approach of ICA to achieve a high-resolution functional template of RSNs. Among the different possible methods to assess FC, we employed ICA because, being a data-driven approach, does not need a prior identification of specific regions of interest, which can be dislocated by the tumoral mass, such as the seed-based approach.
The results of ICA have been then exploited in the two studies presented in the next chapters.
Primary glioma tumors in adults represent a heterogeneous group of expansive lesions of the central nervous system (Lapointe, Perry, and Butowski 2018). Neurosurgical resection is the first line therapeutic approach to the treatment of brain tumors (Ghinda et al. 2018). Growing evidence suggests that gross total resection, as compared to subtotal resection, leads to an improved patient overall survival and progression free survival both in case of high- and low-grade tumors (Brown et al. 2016; Kreth et al. 2013; L. Xia et al. 2018). Nevertheless, the benefits of a prolonged survival must be balanced against the risks of significant decrements of quality of life of both patient and caregivers due to permanent neurological disfunctions following extensive resections. In this regard, the goal of the surgical planning is to preserve critical functional regions, or eloquent areas, and structural connections while removing most of the tumor (Ghinda et al. 2018).

The intraoperative direct brain stimulation during awake surgery is the gold standard for functional mapping of eloquent areas. However, this method requires specific instrumentation and increases the risk of epileptic seizures during the surgery (Pillai 2010; Castellano et al. 2017). In addition, fMRI has proven to be a valid non-invasive and highly sensitive alternative tool for localizing distinct eloquent cortical and subcortical areas before surgery in glioma (Castellano et al. 2017). Task-based fMRI is widely used (Volz et al. 2018) as a presurgical mapping (Ghinda et al. 2018) and potentially could play a role in monitoring treatment and prognosis (Castellano et al. 2017; M. E. Fox and King 2018). Unfortunately, task-based fMRI is demanding for the patient, it is heavily influenced by the patient's performance, and it is not easy to implement in a standard clinical setting (Castellano et al. 2017; Volz et al. 2018; Ding et al. 2019).
Recent studies (M. H. Lee et al. 2016; R. Esposito et al. 2012; Ghumman et al. 2016; Zhang et al. 2009) have proposed the use of rs-fMRI as a reliable technique to overcome these limitations proving its effectiveness in the mapping of eloquent areas of motor (Schneider et al. 2016) and language (Ghinda et al. 2018; Sair et al. 2016) functions. Published studies have restricted the analysis to mapping of eloquent functions in the perilesional area or specific functional networks such as the DMN (Jütten et al. 2020; Hacker et al. 2019; Ghumman et al. 2016). Nevertheless, distal regions or networks could be also functionally impacted by brain tumors (Hacker et al. 2019; Harris et al. 2014) through mechanisms of structural or functional disconnection. There have been only a handful of studies addressing this issue. Nenning and colleagues (Nenning et al. 2020) and Stoecklein and colleagues (Stoecklein et al. 2020) introduced two different indexes to quantify functional connectivity at the voxel level, and have reported significant functional changes at a distance from the tumor, as well as a significant correlation between functional connection alterations and clinical variables such as patient's cognitive status or tumor grade.
In the present study we investigated the effect of gliomas on the brain's main functional networks measured with rs-fMRI (RSNs), both near and far from the lesion. We were interested in examining if functional abnormalities involve predominantly the region near the tumor, the edema region, or structurally normal tissue. Patients often present to the hospital in the acute phase with focal neurological deficits that improve with high-dose steroid therapy. This may indicate a role of the edema region in modulating function.
We developed a novel whole-brain approach, based on ICA, to robustly detect impaired networks at the single patient level. This approach does not need a prior identification of specific regions of interest (Harris et al. 2014; Hart, Price, and Suckling 2016), and extensively exploits the richness of the data. The single patient abnormal connectivity detection involved the comparison of topological

distribution and within network connectivity strength with a healthy controls (HCs) group.

3.2 Materials and Methods

3.2.1 Dataset

Pre-surgical data of 24 patients (11 female, mean age 58.1±16.4y) with de novo brain tumors were collected at the University Hospital of Padova. All participants have regularly taken anticonvulsants for control of epilepsy and corticosteroids. The protocol had been approved by the local Ethics Committee of the University Hospital of Padova and carried out in accordance with the 1964 Helsinki declaration and its later amendments. Informed consent was obtained from all participants.
As HCs, we used a subset of the publicly available MPI-Leipzig Mind-Brain-Body dataset (Babayan et al. 2019). This dataset comprises rs-fMRI scans on n=318 subjects acquired on a 3T Siemens Magnetom Verio scanner with a T2*-weighted gradient-echo echo planar imaging (EPI) sequence (repetition time (TR)=1400ms, echo time (TE)=39.4ms, flip angle (FA)=69°, field of view (FOV)=202×202mm^2, voxel size=2.3×2.3×2.3mm^3, volumes=657, multi-band acceleration factor (MBAccFactor)=4, iPAT=0, phase encoding direction antero-posterior). Ten HCs were discarded due to scanner artefacts or data unavailability. The final HC group consisted of 308 subjects (125 females; mean age 36.96±18.40 years).

3.2.2 Data acquisition

Data were acquired on a 3T Siemens Biograph mMR scanner equipped with a 16-channel head-neck coil. Anatomical imaging included T1-weighted (T1w) 3D magnetization-prepared rapid acquisition gradient echo (TR=2400ms, TE=3.24ms, TI=1000ms, FA=8°, FOV=256×256 mm^2, voxel size=1×1×1mm^3) images acquired both before and after contrast agent injection, a 3D T2-weighted (T2w) image (TR=3200ms, TE=535ms, FOV=256×256mm^2, voxel size=1×1×1mm^3), a 3D fluid attenuation inversion recovery (FLAIR) (TR=5000ms, TE=284ms, TI=1800ms, FOV=256×256mm^2, voxel size=1×1×1mm^3) image. In addition, functional imaging comprised rs-fMRI EPI scans (TR=1260ms, TE=30ms, FA=68°, FOV=204×204mm^2, voxel size=3×3×3mm^3, volumes=750, MBAccFactor=2, iPAT=0, phase encoding direction antero-posterior) and two spin echo-EPI acquisitions with reverse phase encoding (TR=4200ms, TE=70ms, FOV=204 ×204mm^2, voxel size=3×3×3mm^3, MBAccFactor=1) for EPI distortion correction purposes.

3.2.3 Tumor segmentation

The anatomical images of each patient were linearly registered to the patient native T1w image with the Advanced Normalization Tools (ANTs26, v. 2.0.1). Employing these images, two masks were manually delineated through the ITK-SNAP software (http://www.itksnap.org/) by an expert neuroradiologist with more than five years of experience. The first mask, the TM, included the tumor core (contrast agent enhancing and non-enhancing regions) and the necrosis. The second mask, the TM+E, was created by adding the edema area to the TM.

3.2.4 Pre-processing of the data

Imaging data of patients and HCs underwent an analogous structural and functional pre-processing. Data were pre-processed with an in-house pipeline using the following software: ANTs, Statistical Parametric Mapping 12 (SPM12, v. 7219) and FSL (FMRIB's Software Library, www.fmrib.ox.ac.uk/fsl, v. 6.0.3).
Structural pre-processing consisted in bias field correction (N4BiasFieldCorrection (Tustison et al. 2010)), skull-stripping (Multi-Atlas Skull Stripping(Doshi et al. 2013)), tissue segmentation (into GM and WM and CSF, with the unified segmentation tool (Ashburner and Karl J. Friston 2005) of SPM12) and diffeomorphic non-linear registration (as implemented in ANTs SyN algorithm) to the symmetric MNI 2009c atlas. In the patient group, the last step was performed excluding the TM+E (Andersen, Rapcsak, and Beeson 2010).
Functional pre-processing of rs-fMRI data included slice timing, readout distortion (FSL's TOPUP (Andersson, Skare, and Ashburner 2003)) correction, affine realignment of volumes to the central image of the acquisition (FSL's mcflirt (Jenkinson et al. 2002)), a non-linear mapping to the symmetric MNI152 atlas exploiting the subject-specific T1w (via FSL's boundary based registration(Greve and Fischl 2009)) and high pass filtering (cut off frequency 0.008Hz). Since the MBAccFactor of the EPI acquisition sequence differed between the patients and HCs dataset, spurious variance related to scanner artefacts was regressed out from the patients' pre-processed data using an ICA-based approach(Salimi-Khorshidi et al. 2014). Thus, the ICs related to sequence MBAccFactor or broad head movement artefacts were manually identified and regressed out from the original pre-processed data.
Finally, to quantify the subject-specific head motion during the scan, we computed the framewise displacement (FD) as defined in (Power et al. 2012) and compared it between the patient population and controls cohort with the Wilcoxon rank sum test to ensure that the two groups did not significantly differ in terms of head motion.

3.2.5 Definition of an high-resolution template of RSNs

Functional pre-processed data were analysed with the Group ICA of fMRI toolbox (GIFT) (V. Calhoun et al. 2001) and custom codes written in Matlab (MATLAB 2019b, The MathWorks, Inc., Natick, MA).
To achieve a high-resolution functional parcellation of the main RSNs, we performed a group-level spatial ICA on a subset of 140 controls homogeneously selected from the 308 HCs in the available age range (35 between 20-30y, 27 between 30-40y, 8 between 40-50y, 7 between 50-60y, 41 between 60-70y and 22 between 70-80y). The high model order decomposition (Allen et al. 2014) was performed by using the Infomax algorithm and setting the number of ICs to 180. To confirm the stability of the result, the ICA was repeated 10 times within the ICASSO (Himberg, Hyvärinen, and F. Esposito 2004) framework and a central solution was selected using the modes of the component cluster. The goodness of the final decomposition was evaluated with the cluster stability/quality (Iq) index returned from ICASSO and compared with literature reports.
Then, following Griffanti et al. 2014, the group ICs were manually labelled into artefactual (i.e., related to head motion, physiological noise, MBAccFactor, etc.) or intrinsic connectivity network, the components, by visually inspecting their spatial maps and time courses power spectra.
Afterwards, components were grouped into 10 RSNs according to their spatial pattern: visual (VIS), sensorimotor (SMN), auditory (AUD), cingulo-opercular (CON), dorsal-attention (DAN), fronto-parietal (FPN), default-mode (DMN), cognitive-control (CCN), frontal (FRN) and language (LANG) network. Specifically, we computed their normalized spatial overlap with two functional atlases: the Yeo Atlas (7 networks) (Thomas Yeo et al. 2011), and the Gordon Atlas (Gordon et al. 2016), and assigned the component to the best matching RSN. In addition, RSN components with poor overlap with the previous two atlases were localized using the database NeuroSynth (https://www.neurosynth.org) using the peak activation position to find the best matching network.

3.2.6 Single-subject RSNs

Using the selected group-level components as spatial constraints, to accurately retrieve the single-subject RSNs spatial pattern (Salman et al. 2019), we employed the group-information guided ICA (GIG-ICA) back-reconstruction algorithm (Saha et al. 2020) as implemented in the GIFT toolbox. At the end, for each patient and HC, each back-reconstructed component consisted of a spatial z-score map reflecting the network's coherent activity across space.

3.2.7 Statistics: RSNs alterations

To determine whether a patient's component was impaired, we examined its topography and magnitude and compared it with that of the HC group. For each control/patient and each component, we quantified the similarity between the component spatial pattern obtained at the group and at the single-subject (SS) level with the cosine similarity measure (CS), computed as

$$CS(comp_i) = \frac{MAP_{group}(comp_i) \cdot MAP_{ss}(comp_i)}{||MAP_{group}(comp_i)|| \cdot ||MAP_{ss}(comp_i)||} \tag{3.1}$$

where $comp_i$ is the i^{th} component and $Map(comp_i)$ is the vectorization of the component's spatial map. We choose this index because it is sensitive to both component's spatial pattern and magnitude (i.e., connectivity strength) differences. To note that, as we were interested in the peak activations of each RSN, the CS was computed within a component-relevant mask obtained thresholding the group-level component at z-score=1 and filtering spurious voxels (i.e., only cluster with at least 200 connected voxels were included in the mask) and voxels belonging to cerebellum (defined according to Neuromorphometrics Inc. atlas (http://www.neuromorphometrics.com/)) out.
In this way, for each component we achieved a statistical description of the CS distribution in the control group, as shown in Figure 3.1.
Then, to evaluate whether a specific component was significantly altered in a single patient, we employed a permutation test to compare the CS of this patient with the HCs' distribution (50000 permutations, significance level of 0.05). In each permutation we compared the CS distribution of 200 out of 308 HCs against the single-patient CS value, using 3 standard deviations as strength of evidence against the null hypothesis that the patient's CS belonged from the healthy controls distribution.

3.2.8 Overlap with tumor core and edema

We examined whether the tumor location or the extent of edema affected the component topography, by computing for all patients the percentage overlap between the altered components and

1. the tumor mask
2. the edema
3. the remaining normal-appearing brain tissues

This computation was performed both considering separately each RSN and using a unique mask that included all altered RSNs. In the latter case, for each patient,

we created the patient altered RSNs mask, obtained as the union of the group RSNs masks (described in the previous paragraph) that were labelled as impaired for that specific patient. The percentage normalization was computed using the abnormal mask extent as reference, as follows:

$$overlap = \frac{alteredRSN_{mask} \cap tissue_{mask}}{alteredRSN_{mask}} \tag{3.2}$$

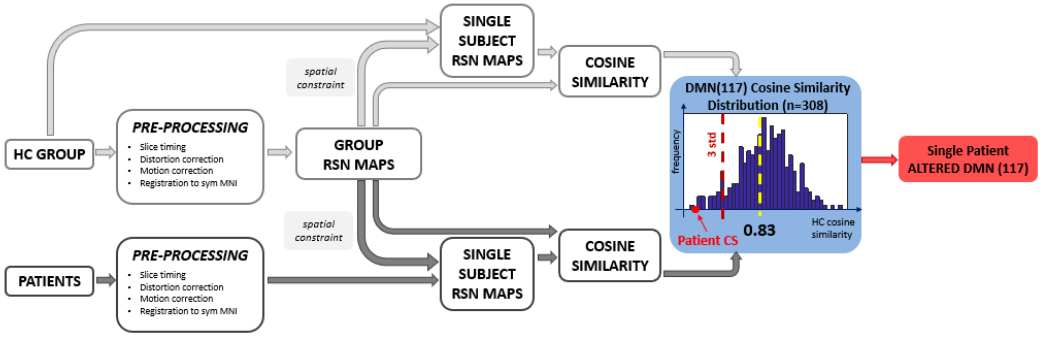

Figure 3.1: Schematic workflow of the analyses.

3.3 Results

3.3.1 Patients characteristics

The demographics and clinical data of the patients are reported in Table 3.1. Figure 3.2 shows the frequency maps of the lesions in the patient population. In Panel A the frequency map of the TM is reported, whereas in Panel B the frequency map of the TM+E masks. The distribution is sparse with tumors involving predominantly the right frontal and left temporal lobes, with a low spatial overlap (maximum value 20.8% of patients for the TM, and 33.3% of patients for the TM+E).
No statistically significant differences were found between the patients' and healthy controls' group in head motion during rs-fMRI acquisition: the median FD was respectively of 0.15±0.04mm and 0.14±0.04mm; and the p-value of the rank sum test was equal to 0.16.

3.3.2 High-resolution template of RSNs

Overall, 45 different ICs were identified. The obtained decomposition was highly reliable and reproducible with a cluster Iq of the selected components that ranged between 0.736 and 0.996 (in line with the findings of Saha et al. 2020).

Age	58.1±16.4y
Gender	
Female	11
Male	13
Tumor histology	
Astrocytoma	1
Diffuse astrocytoma	1
Glioblastoma	15
Gliosarcoma	1
Glioneuronal neoplasm	2
Oligodendroglioma	1
Other	3
Tumor Grade	
I	1
II	3
III	2
IV	17
n.a.	1
IDH-1/2 mutation status	
Wild type	14
Mutated	6
n.a.	4
Tumor site	
Left	14
Right	6
Bilateral	4

Table 3.1: Demographics and clinical variables collected for the patients. Abbreviations: n.a.=not available, IDH=isocitrate dehydrogenase gene.

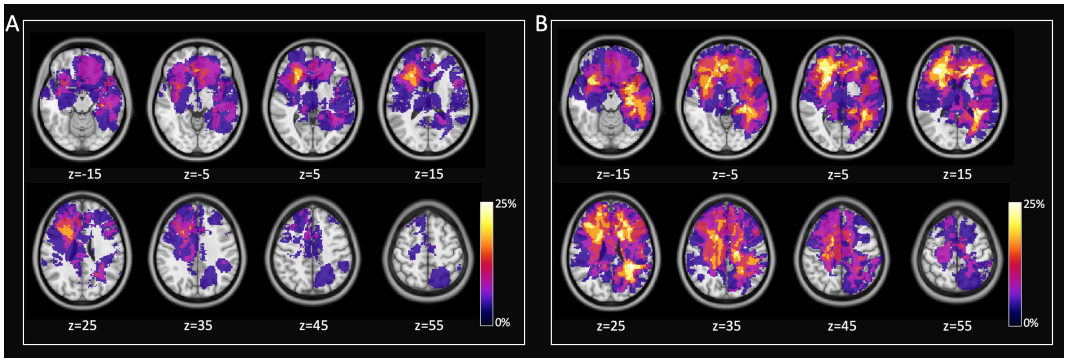

Figure 3.2: Lesion frequency map across patients. (A) Frequency map of tumor core, (B) map of tumor lesions including edema area. Maps are over imposed to the MNI atlas (grey scale). Radiological conventions.

To assign the component to a specific RSN, the overlap with two functional atlases approach worked well for VIS, SMN, AUD, CON, DAN, FPN and DMN, whereas for CCN, FRN and LANG networks the assignment of a component was based on the NeuroSynth meta-analysis. Eventually, we obtained 11 components in the VIS, 4 in the SMN, 1 in the AUD, 3 in the CON, 3 in the DAN, 4 in the FPN, 6 in the DMN, 9 in the CCN, 3 in the FRN and 1 in the LANG RSNs. The spatial pattern of these group components is depicted in Figures 3.3 and 3.4.

3.3.3 Assessment of RSNs alterations

In our patient cohort, several components revealed significantly different topography to that observed in the healthy controls.
Figure 3.5 shows examples of how the tumor affects the RSN spatial distribution in two patients suffering from IDH1 mutated high-grade glioblastoma of the left hemisphere. The first patient (#07) has a lesion in the WM of the left inferior parietal lobule (IPL). The DMN(117) component is strongly altered with a ΔCS_σ equal to -6.18. A relatively normal left IPL cortical component overlying the lesion contrasts with the loss of the praecuneus, contralateral right IPL, and ipsilateral left lateral and mesial frontal components. This pattern is consistent with the disconnection of WM pathways connecting the left IPL with the other nodes of the DMN. The second patient (17) has a large lesion involving occipital, parietal, and temporal WM with a cortical involvement. The VIS(153) component in HCs is bilateral in the occipital cortex and extends dorsally along the intraparietal sulcus. In the patient we observe some preservation of the ipsilateral occipital component, but a loss of contralateral occipital and bilateral parietal components (which leads to a ΔCS_σ of -5.55), again consistently with WM disconnection. The same patient also shows a significant alteration of the language network (ΔCS_σ equal to -4.09) with a weakened superior temporal and frontal components of the network.
These three examples highlight the effect of gliomas on the correlated activity of cortical regions that are distant from the site of the tumor but are functionally connected through altered WM pathways.
For each patient, we quantified the significant changes in the network topography (Figure 3.6). Overall, we detected in each patient a relatively high number of altered components ranging from 0 to 23 (mean value 6.9±5.2). Aggregating these findings by RSNs and ranking them by % of patients with at least one component affected, we found that 70.8% of the patients had alterations in the FPN, 70.8% in CCN, 62.5%, in VIS, 41.7% in DMN, 41.6% in FRN, 29.2% in CON, 25% in DAN, and 8.3% in LANG network. When averaging across patients, tumors caused alterations in 35.9% of FPN components, 21.7% of FRN, 17.4% of CON, 17.4% of CCN, 15.4% of VIS, 11.6% of DAN, 10.1% of DMN, and 8.7% of LANG.

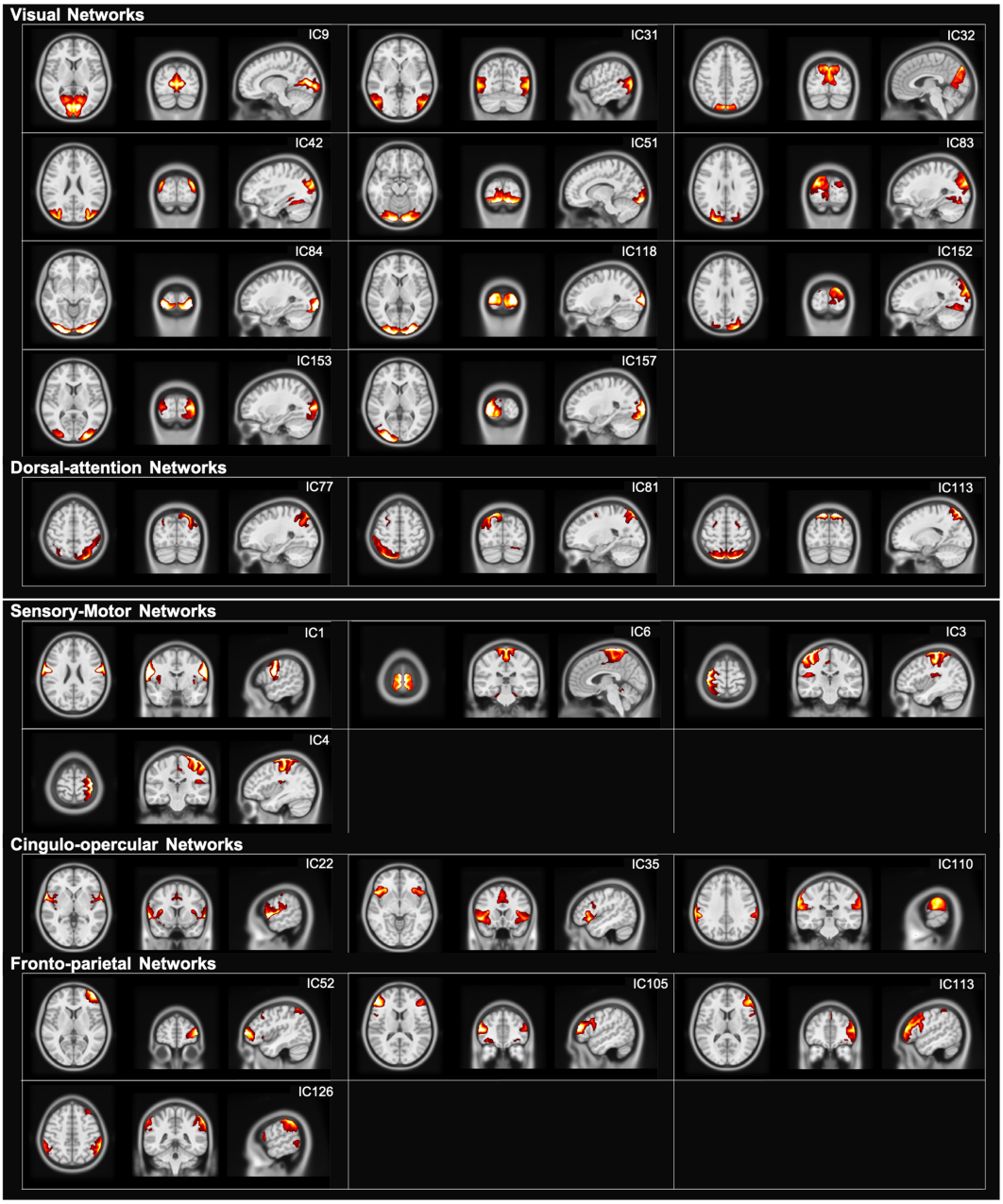

Figure 3.3: Spatial pattern of the peak activation clusters of the group ICs superimposed on the T1w image of the MNI152 symmetric atlas (in grey scale). Peak activation clusters are calculated by keeping only voxels with a z-score value greater than 5 and belonging to connected clusters of at least 200 voxels. Images are displayed in radiological conventions.

Interestingly, no altered components occurred in the SMN and AUD networks. While the relatively higher frequency of tumors in the frontal lobe explains the abnormalities of RSN components in FPN, CCN, CON, networks with a strong prefrontal representation, more surprising is the high frequency of abnormal VIS

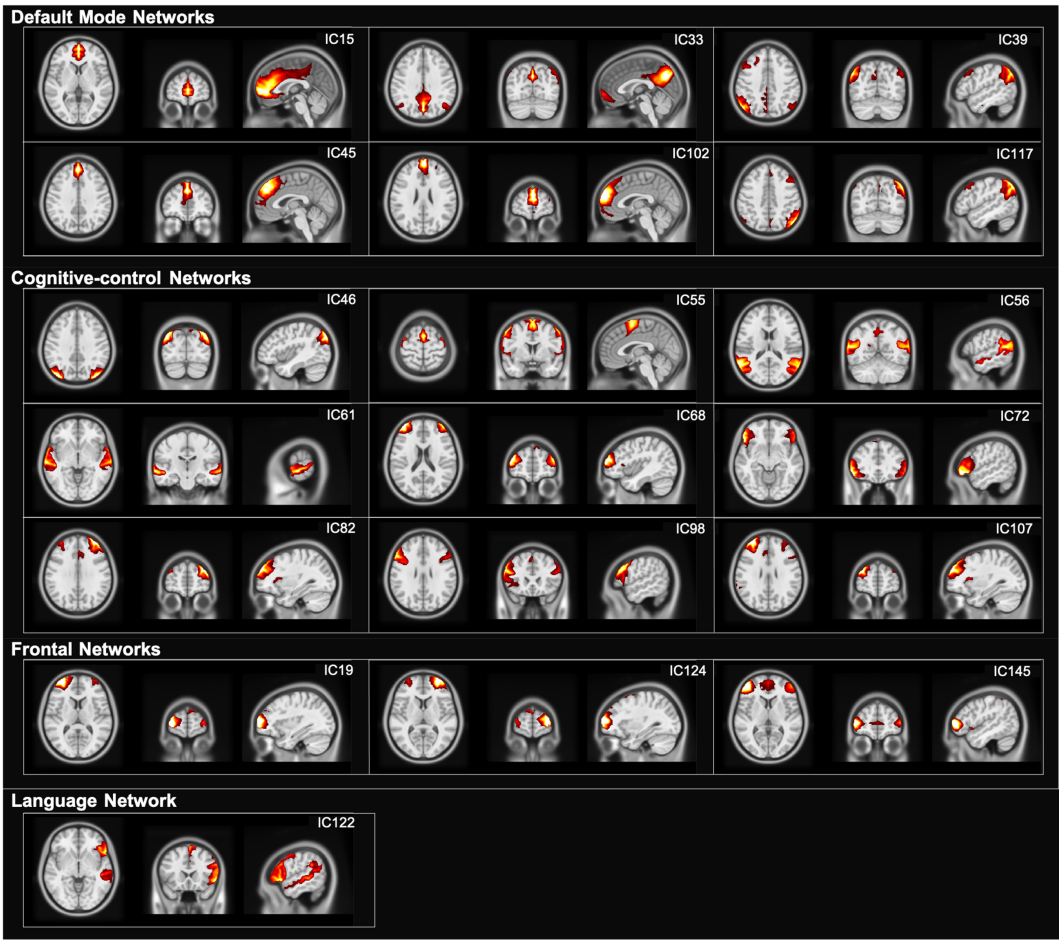

Figure 3.4: Spatial pattern of the peak activation clusters of the group ICs superimposed on the T1w image of the MNI152 symmetric atlas (in grey scale). Peak activation clusters are calculated by keeping only voxels with a z-score value greater than 5 and belonging to connected clusters of at least 200 voxels. Images are displayed in radiological conventions.

component, given their location in the occipital lobe, the least frequently involved structurally and farthest away from the most common frontal and temporal locations. It is also notable that in this group of glioma patients, enrolled for a neurosurgery, no functional abnormalities were detected in the sensory-motor network, and very few in the language network. This might reflect a selection bias toward lesions that are 'safer' to operate when they do not cause motor or language impairments after surgery.

3.3.4 Overlap between tumor and altered RSNs

Regarding the single component percentage overlap, we found overlaps with the TM mask ranging between 0 and 22.1%, with edema between 0 and 11.0%, and

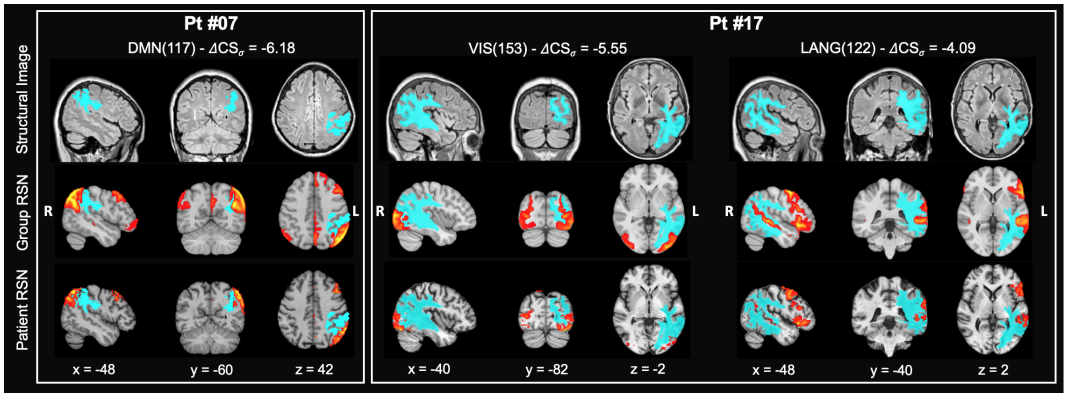

Figure 3.5: Example of altered RSNs in two representative patients. The patients were affected by IDH1 mutated high-grade glioblastomas in the left hemisphere. Structural image: FLAIR image with the segmentation of the tumor and edema (light blue) superimposed. Group RSN: T1w MNI atlas with RSN healthy controls group average component (red-yellow scale). Patient RSN: patient individual altered component. Left panel: default mode network component (DMN(117)) in patient #07. Right panel: visual network (VIS(153)) and language (LANG(122)) component in patient #17. ΔCS_{sigma} is the distance from the group average. Radiological conventions.

with normal tissue between 74.1 and 100%. Overall, the VIS, DAN, and LANG networks show the least overlap with the tumor mask with a maximum overlap of 6.3%, 2.4% and 4.3%. To quantify the impact of tumor at the level of individual subject, Table 3.2 reports the results of the overlap with tumor tissue (TM, edema, normal tissue) patient by patient. The mean percentage overlap was quite small with both TM (2.6%±2.3%) and edema (1.0%±1.5%). The range of overlap was also quite small: TM (0-8.2%), edema (0-4.9%). Most of the network alterations involved normally appearing tissue with a mean overlap of 96.3%(±2.7%) and range 91-100%. These findings strongly suggests that network alterations involve regions near the tumor or within the edema in a very limited way, but rather distant functionally connected regions. To examine this issue, we measured spatial pattern alteration of each component (quantified by the ΔCS_σ) and the overlap between these components and TM. There was a weak negative statistically significant Spearman's correlation between altered components ΔCS_σ and the overlap with the TM mask (ρ=-0.18, p=0.04), and no statistically significant correlation with the overlap with the edema area (ρ=-0.04, p>0.05). These findings indicate that RSN components were not altered in relation to the proximity with the tumor or overlap with the edema.

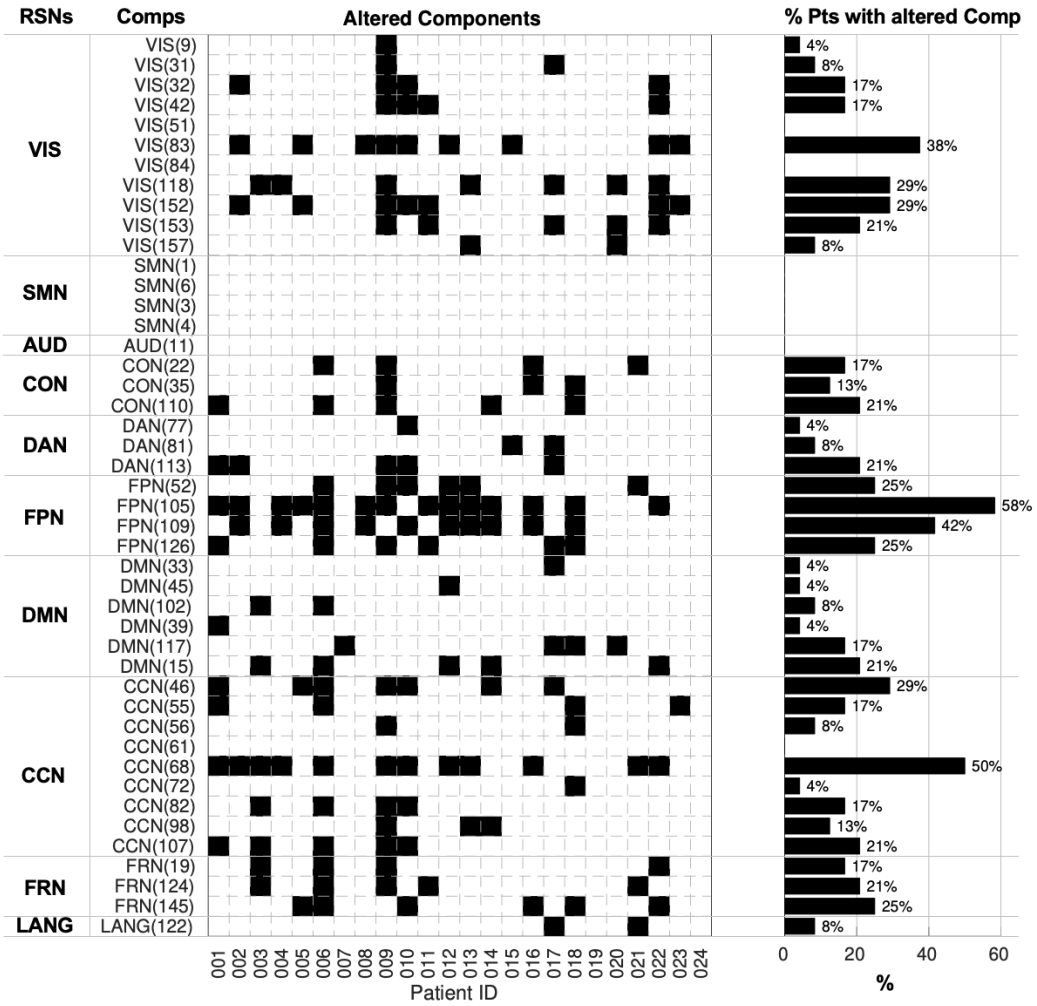

Figure 3.6: Altered RSNs. On the left, the matrix reports significant alterations, marked as black squares. Rows represent specific ICs organized by networks they belong to and columns single patients. On the right, for each component the bar plot shows the percentage of patients with that component damaged.

		Tissue	
Patient	**Tumor Core and Necrosis**	**Edema**	**Normal appearing**
1	0.1	0.3	99.6
2	4.7	0	95.3
3	0	4.8	95.1
4	1.7	0	98.3
5	2.4	0.2	97.5
6	0.5	0.1	99.4
7	1.5	1.9	96.6
8	3	2.4	94.6
9	5	0.2	94.8
10	0.3	0.7	99
11	2.6	0.7	96.6
12	6.3	1	92.7
13	1.5	0	98.5
14	6	3.1	90.9
16	1	0.5	98.5
17	4.2	0.9	94.9
20	1	4.9	94.1
21	8.2	0.6	91.3
22	-	-	-
23	0.1	0	99.9
24	4.6	0	99.9
26	0.5	0.2	99.3
27	2.9	0.4	96.6
28	-	-	-
Average	**2.6**	**1**	**96.3**
Std	**2.3**	**1.5**	**2.7**

Table 3.2: Single patient percentage overlap between the altered components and 1) the tumor mask (core and necrosis), 2) the edema and 3) the remaining normal-appearing brain tissues.

3.4 Discussion

The pre-surgical acquisition of task and resting-state fMRI is a viable and informative tool to support surgical planning and investigate the effects of brain tumor on human brain. Most studies to-date have focused on the functional mapping of eloquent areas or limited the investigation to the perilesional region (Ghinda et al. 2018, Schneider et al. 2016, Sair et al. 2016). Nevertheless, preliminary findings suggested that brain tumor affect broader systems such as brain networks (M. E. Fox and King 2018, Hacker et al. 2019) and proposed the lesion-network (Gleichgerrcht et al. 2017, Fornito, Zalesky, and Breakspear 2015) symptom mapping as an approach to get relevant insight on the impact of these expansive lesions. Here we propose a novel method to quantify changes in topography and strength of the RSNs across the whole brain after a high-resolution spatial decomposition based on a healthy control template. A whole-brain approach of rs-fMRI data allows to better exploit the richness of the data and yields a detailed description of functional network alterations at the level of individual patients both in the perilesional and in distal regions. This is highly valuable for clinical evaluation. The method was applied to a cohort of tumor patients with heterogeneous tumor location and histopathology.

The most important result is the discovery that a large fraction of the functional connections of the brain are altered in brain tumors. No matter how we aggregate the results, the effect is important. Out of 45 RSNs components identified in healthy controls a mean of 7±5 components were altered. When we aggregate by % patients with affected RSNs, the range across RSNs varies with 71% of the patients showing alteration of the FPN to 8% with alterations of the LANG network. When we average across patients and look at % of altered components in each RSN the range varies from 36% of the components in the FPN to 9% in the LANG network. Notably, we see no alterations in the sensory-motor network and auditory network, and very infrequent alterations in the language network. The relative predominance of networks with a frontal component (FPN, CON, CCN) is explained by the higher frequency of frontal tumors. The paucity of altered networks in eloquent regions (motor, auditory, language) is due to a sample bias. All our patients underwent surgery and were selected not to suffer post-operative neurological deficits of these functions. In fact, Figure 3.2 shows no tumor with a localization in the motor cortex, and very few with a localization near Broca's area. However, it is important to highlight, this is the second result, that functional network abnormalities did not fall in the region of structural damage or even within the much larger edema region. This can be appreciated in Figure 3.5 where individual RSNs components near the lesion are preserved, while those at a distance are affected. It is also evident in Table 3.2 with a mean overlap between RSNs alterations and tumor core/necrosis of 2.6%±2.3% (range 0-8.2%),

and with edema of 1.0%±1.5% (range 0-4.9%). 96.3% of RSN alterations fall within normally appearing structural tissue. This finding has two very important clinical implication. First, the consistent sparing of RSN component in the cortex overlying the tumor has implications for the surgical approach. While a straight perpendicular approach may be the shortest path to the subcortical WM lesion, this approach will hit functional synchronized cortex. More, parallel navigation to subcortical lesions has been proposed using tractography (e.g. by Essayed et al. 2017), but our single subject fMRI mapping provides a relatively easier way that uses a less operator dependent method.
Secondly, patients with brain tumors most often present to the clinician because of new onset neurological deficits. A scan typically shows the primary lesion and perilesional WM edema. Steroid therapy is started to decrease the extracellular edema caused by the tumor and patients' symptoms typically improve. In addition, anticonvulsants for control of epilepsy are also administered. Neurological symptoms are thought to improve due to the local resolution of the edema. However, our results clearly show that another explanation for the neurological symptoms is the remote dysfunction of functional brain networks in structurally normal areas. Our patients at the time of scan had received already several days of high dose steroid therapy, and we can only speculate if the effects on the RSN and relative overlap with edema were enhanced or minimized by the therapy. The likely mechanism of remote functional dysfunction is the disconnection, either structural or functional, caused by the lesion on WM pathways connecting different nodes of a network. This is evident in Figure 3.5 where the affected DMN shows a normal component in the IPL cortex overlying the lesion, but no synchronization in anatomically connected regions of the praecuneus, contralateral IPL, and frontal cortex. Since gliomas invade along preferential routes, such as those along WM tracts and in the perineuronal and perivascular spaces (Ferrer, Moura Neto, and Mentlein 2018), we can speculate that the lack of distant synchronization reflects a combination of structural and functional effects on WM pathways. For example, it is now increasingly recognized that neuronal activity robustly regulates central nervous system glial precursor proliferation as part of a process known as myelin plasticity, and that gliomas interact with neurons potentially altering neuronal activity (Gillespie and Monje 2018). Our results are consistent with De Baene and colleagues (De Baene, Rutten, and Sitskoorn 2019) and Nenning and colleagues (Nenning et al. 2020) who found altered inter-hemispheric functional connections in unilateral glioblastomas. These alterations were related to the proximity of the RSN to the tumor, and not the strict anatomical distance from it.
Despite promising results, this study has some limitations. The relatively small number of subjects prevents sensitive behavioural correlations. The genetic pro-

file of the tumors that certainly have an impact on prognosis and likely brain organization was not considered given the small sample size. The heterogeneity of the topography of the lesions that could not be quantitatively compared with the RSN altered topography.

3.5 Conclusions

In summary, in this study we developed a novel method to investigate the changes in RSNs in glioma patients. We showed that functional alterations in network topography and strength are widespread and occur far from the lesion or the edema, with cortical regions near the glioma that are potentially preserved. Our individualized approach could identify cortical regions to be carefully navigated during surgery, and widespread alterations of functional networks away from the tumor.

Chapter 4

Brain states functional dynamics in healthy aging

4.1 Introduction

In the last decades, rs-fMRI studies have investigated the effects of aging in healthy subjects, showing that the brain undergoes both structural and functional alterations (Betzel et al. 2014, Jessica S. Damoiseaux 2017, Ferreira 2013, Wang et al. 2012). The undoubtedly strongest result found among rs-fMRI studies performed at the network level, is a reduced functional segregation (Chan et al. 2014, J. Song et al. 2014) and increased between-network connectivity (Betzel et al. 2014) which underlines the tendency of RSNs to reorganize in a more integrated topology (Bagarinao et al. 2019) with the increase of age. Specifically, several works reported a weaker within-network FC with age in the default mode, (Andrews-Hanna et al. 2007, Betzel et al. 2014, J. Damoiseaux et al. 2008, Geerligs et al. 2015, J. Song et al. 2014, Tomasi and Volkow 2012, Varangis et al. 2019, Zonneveld 2019), ventral-attention (Andrews-Hanna et al. 2007, Betzel et al. 2014 Tomasi and Volkow 2012, Zonneveld 2019) and executive networks (Betzel et al. 2014, Geerligs et al. 2015, Varangis et al. 2019). Regarding sensorimotor and visual networks, the results were quite inconsistent among studies. Indeed, within the sensorimotor network, many groups found a FC increase (J. Song et al. 2014, Tomasi and Volkow 2012), other a decrease (Zonneveld 2019) or even no changes (Geerligs et al. 2015). FC was found to be increased with older age within the visual network in (Betzel et al. 2014, Chan et al. 2014, Yan et al. 2011), decreased in (Zonneveld 2019), or to remain stable across age (Geerligs et al. 2015, Varangis et al. 2019). Although these studies have investigated how RSNs are distributed across the lifespan, they are all based on static FC analysis. To our knowledge, only a few studies (Chen et al. 2019, Tian et al. 2018, Y. Xia et al. 2019) have investigated the relationship between aging and brain states de-

rived from dFC analyses. Both studies are based on SW + clustering approach in healthy subjects. Despite using comparable populations and the same methodological approach, the three studies reached conflicting results. Specifically, a different number of states was identified: three in Tian et al. 2018 and five in the other two studies. In addition, concerning the dwelling time (i.e., the duration of each state throughout the scanning time) and the number of transitions between states as a function of age, Chen and colleagues did not find any differences in the dwelling time, whereas both in Tian et al. 2018 and Y. Xia et al. 2019, significant differences were reported. In particular, Tian and colleagues observed a positive correlation between age and the dwell time of the "loose interaction state", characterized by an overall weak connectivity, whereas Xia and colleagues found a positive correlation between dwelling time and age. The number of transitions between states was found to be mostly negatively correlated with age in Y. Xia et al. 2019, whereas in Chen et al. 2019 an opposite direction was observed.
Given the discordant results of previous studies, in this work we investigated the developmental trajectories of dynamic brain states employing rs-fMRI data of 88 healthy subjects, using the model-based method of HMM.
Exploiting the ICA performed in the study presented in chapter 3, we used the ICs time courses within the HMM framework and we estimated the model parameters. Contrary to previous studies based on SW and clustering techniques, the choice of the number of states in the model was based on a quantitative approach: after introducing a new index to quantify the precision of the estimates, the goodness of the fit and the precision were assessed as the model order varied. Finally, to investigate the effects of aging on dynamic properties of brain states, we characterized the age-relation of temporal variability and organization of the states, using temporal metrics, derived from single-subject sequences of visited states, and a graph-theory approach. This study was divided into two parts: 1) methodological considerations related to the application of HMM and 2) assessment of the differences in brain states properties between young and old subjects.

4.2 Materials and Methods

4.2.1 Dataset

MRI data from 88 healthy participants from the publicly available MPI-Leipzig Mind-Brain-Body dataset (Babayan et al. 2019, Mendes et al. 2019) were analyzed. The original dataset consisted of 318 subjects, from which 10 subjects were excluded or for scanner artefacts or unavailability of rs-fMRI data or corrupted structural scans or failure of the pre-processing stages. Data selection were then

performed excluding participants with SKID diagnoses, drug abuse and a FD of functional scans greater than 0.3mm. The final pool of subjects was divided into two groups: the young group (Y: n = 44; 20 females, 24 males; age range = 20-25 years) and the old group (O: n = 44; 22 females, 22 males; age range = 60-80 years).

4.2.2 Data acquisition

Full details on MRI data acquisition are provided in Mendes et al. 2019. In brief, the acquisition was performed with a 3T Siemens Magnetom Verio scanner, equipped with a 32-channel head coil. The scanning protocol included the following sequences:

- T1-weighted 3D magnetization-prepared 2 rapid acquisition gradient echoes (MP2RAGE) (TR=5000ms, TE=2.92ms, TI1=700ms, TI2=2500ms, first flip angle=4°, second flip angle=5°, FOV=256×240×176mm^3, voxel size=1×1×1mm^3, multiband acceleration factor (MBAccFactor)=3)

- rs-fMRI scans (TR=1400ms, TE=39.4ms, flip angle=69°, FOV= 202×202mm^2, voxel size=2.3×2.3×2.3mm^3, volumes=657, MBAccFactor=4)

- two spin echo acquisitions (TR=2200ms, TE=52ms, flip angle=90°, FOV=202×202mm^2, voxel size=2.3×2.3×2.3mm^3)

During rs-fMRI scans, the subjects were asked to keep their eyes open and to lie down as still as possible.

4.2.3 Pre-processing of the data

A structural pre-processing was applied on the pseudo-T1w image, obtained by multiplying the T1w 3D-MP2RAGE image with its second inversion time image. The pipeline included bias field correction (N4BiasFieldCorrection (Tustison et al. 2010)), skull-stripping (MASS ((Doshi et al. 2013)) and non-linear diffeomorphic registration (Avants et al. 2011) to the symmetric MNI152 2009c atlas (Fonov et al. 2011).
Functional pre-processing of resting state data included slice timing (Stephen M. Smith et al. 2004), distortion (TOPUP Andersson, Skare, and Ashburner 2003) and motion correction (MCFLIRT Jenkinson et al. 2002) and non-linear registration to the symmetric MNI atlas (Fonov et al. 2011) passing through the single subject pseudo-T1w image (boundary-based registration, (Greve and Fischl 2009)).
Since we decided to use a data-driven approach, instead of using an atlas-based

parcellation, to achieve an high-resolution template of the main RSNs, we employed the GIFT toolbox (http://trendscenter.org/software/gift/) to decompose the functional pre-processed data into ICs, as previously explained in section 3.2.5. Firstly, we performed a group spatial-ICA, setting the number of ICs to 180. Among these, those related to banding artefacts, vascular or noise components were discarded, resulting in a set of 46 components (M=46). The ICs were first manually classified by visual inspection of both the spatial maps and the power spectra, in accordance with (Damaraju et al. 2014, Griffanti et al. 2014) and then they were matched with the Gordon (Gordon et al. 2016) and Yeo (Thomas Yeo et al. 2011) functional atlases. The RSNs were grouped into 11 functional domains: visual (VIS), sensorimotor (SMN), auditory (AUD), cingolo-opercularis (CON), dorsal-attention (DAN), fronto-parietal (FPN), default-mode (DMN), cognitive-control (CCN), frontal (FRN), cerebellum (CER) and basal ganglia (BG). Then, the group-information guided ICA (GIG-ICA) back-reconstruction algorithm (Du and Fan 2013) was used to estimate the subject-specific spatial maps and time series of each independent component.
The following steps were performed on the time courses of the 46 ICs to reduce the remaining noise: (1) despiking, applied with the *icatb despike tc* function of the GIFT toolbox, (2) multiple regression of the 6 head motion parameters, their temporal derivatives, mean WM and mean CSF signals (Jo et al. 2013), (3) high-pass filtering (cut-off frequency = 1/128 Hz). No global signal regression was applied.

4.2.4 Hidden Markov Model setup

As done in (Vidaurre, Stephen M. Smith, and Woolrich 2017), we applied HMM to the time courses of the 46 ICs and the inference was done at the group level using the HMM-MAR toolbox (Vidaurre, Quinn, et al. 2016), available in Matlab in a public repository (https://github.com/OHBA-analysis/HMM-MAR). Prior to running the inference, each subject-specific time course was standardized (i.e., each IC has mean equal to zero and standard deviation (std) equal to one), and then temporally concatenated across all participants, yielding a data matrix of dimensions 88 subjects x 46 ICs x 657 time points. In this way the model inference was performed at the population level.
We adopted a multivariate Gaussian distribution for the observational model, as described in section 2.3.2. Since the inference was performed on the demeaned and standardized ICs time courses, μ_k describes a change away from the grand-average zero activity level.

4.2.5 Choice of the initialization algorithm

The number of repetitions of the initialization algorithm was set to 5 and out of these the best in terms of FE was used as starting point for the inference run. Since there is not a gold standard to perform the initialization of the hidden states probabilities, we tried both a random initialization and an initialization with a mixture of Gaussian models.
Given the non-linear nature of the VB algorithm, and therefore the possibility of reaching a local minimum of the cost function, 200 realizations of the model were performed for each of the two types of initialization. Then, the 200 realizations were sorted on the basis of the FE and the one with the lowest value of FE was chosen. This procedure was performed for the two different initialization and the best realization in terms of FE was kept.
To ensure that the choice of the initialization did not lead to a large variation in the estimates, two indices between the best repetitions obtained with the two initialization were computed. The first one is the Spearman correlation (ρ), evaluated between the μ_k estimates of the different states and the second one is the similarity between Γ (i.e., the probability of visiting a state over time) of the two realizations after optimally reordering the states, evaluated through the Munkres algorithm (Munkres 1957).

4.2.6 Choice of model order

In the HMM framework, the number of states (K) assumed to model the dynamics of the BOLD signal must be set before running the inference. Given the modest amount of data employed in the study, we fit the model with a number of states ranging from 2 to 8 and then for each order we evaluated the following indices: the Free Energy (FE) and the average log-likelihood (avLL), as indices of goodness of the fit; the Akaike (AIC) (Akaike 1973) and the Bayes Information Criterion (BIC) (Schwarz 1978) as parsimony indices.
In addition, the uncertainty of the μ_k estimates was also assessed for each model order and for each IC within each state, by computing the coefficients of variation (CVs), defined as:

$$CV_k = 100 \cdot \sqrt{(diag(\Omega_k))}^{-1} \tag{4.1}$$

The CV value ranges from 0 to 100, where 0 represents no uncertainty.
To summarize the uncertainty associated with the μ_k estimates as the model order K increased, the average and standard deviation of the CVs inside each state were computed. Then, for each K, the ratio between the CV's mean standard deviation and CV's average value across states was evaluated. Therefore, the best model order was selected by taking into account not only the FE, avLL, AIC and BIC, but also the CV's ratio index.

Moreover, once the model order was fixed, to highlight the less and more precise μ_k estimates, we also computed the ΔCV, defined as the distance between each IC's CV and the average CV ($\overline{CV}$) among ICs within the same state:

$$\Delta CV = CV_{IC_m} - \overline{CV} \qquad m = 1, .., M \tag{4.2}$$

4.2.7 Chronnectome

Starting from the probability of each state to be active at each time point, i.e. Γ, for each subject the most likely sequence of states was computed exploiting the Viterbi algorithm.
Once obtained the Viterbi path, to describe subject-specific temporal characteristics of brain states, three metrics, that defined the so called "chronnectome", were evaluated starting from it:

- the fractional occupancy (FO), defined as the proportion of time that each subject spends in each state
- the lifetime (LT) of each state, defined as the duration of the visits to that particular state
- the switching rate (SR), defined as the frequency of transitions between different states.

To compare these chronnectome metrics among the two groups, we first averaged them within the group, then a two-sample Kolmogorov-Smirnov (K-S) test followed by multiple comparison correction (False Discovery Rate-FDR,α=0.05) was applied for statistical testing of differences between groups.

4.2.8 Brain states graph metrics

Strength and Local Efficiency

To detect the network organization of the estimated brain states, firstly the states Pearson's correlation matrices were derived from the corresponding covariance matrices Σ_k (Σ_k=Ω_k^-1). Then, a graph theory-based approach was exploited to summarize the FC properties. Two metrics were used: the strength (STR) to describe FC global properties, and the local efficiency (EL) to quantitatively investigate the behavior at the local level. The computation was performed with the Brain Connectivity Toolbox (BCT) (Rubinov and Sporns 2010). Before evaluating the graph measures, a proportional threshold approach (Achard and Bullmore 2007) was applied to FC of each state. The 20% of the strongest edges were retained ensuring equal density across states. A two-sample K-S test followed by

multiple comparison correction (FDR, α=0.05) was applied to test for significant differences between states graph metrics.
This analysis allowed us to characterize the topological properties of the states FC at the whole brain level, but it was blind to graph measures differences at the level of single RSNs. For this reason, to compare STR and EL across RSNs, we introduced two novel measures, nSTR and nEL, that were evaluated for each graph metric within each of the 11 functional domains (i), normalizing each measure specific for one state with respect to those computed across all the states:

$$nSTR = \frac{\overline{STR_{k,i}} - \overline{STR_{all,i}}}{std(STR_{all,i})} \qquad k = 1:6, i = 1:11 \tag{4.3}$$

$$nEL = \frac{\overline{EL_{k,i}} - \overline{EL_{all,i}}}{std(EL_{all,i})} \qquad k = 1:6, i = 1:11 \tag{4.4}$$

Modularity

To further investigate the organization of RSNs in each state at the functional module level, we applied the Louvain's community detection algorithm (Blondel et al. 2008) on the thresholded FCs. Given the non-deterministic nature of the algorithm, we repeated the community assignment 50000 times. Then, to obtain the most representative modularity, we first created for each state and each of the 50000 iterations, the corresponding modular matrix, assigning to each node the index of the module in output by the function, then, from these 50000 matrices, we computed the mode matrix and a binary matrix indicating the assignments which were present in more than 95% of the realizations. The final modular matrix of each state was hence obtained by multiplying the binary and the mode matrix.
To quantify the similarity of the community assignment obtained for each state, after binarizing the modular matrices, we computed the Sorensen-Dice similarity coefficient between each pair of states matrices or considering the intra-domains connections or the inter-domains ones, thus obtaining the intra-Dice and inter-Dice values, respectively.
To capture significant differences between states, the intra/inter-Dice values, lower than the 10^{th} percentile of the distribution of all intra/inter-Dice values,

were considered. The schematic workflow followed for the analysis is reported in Figure 4.1.

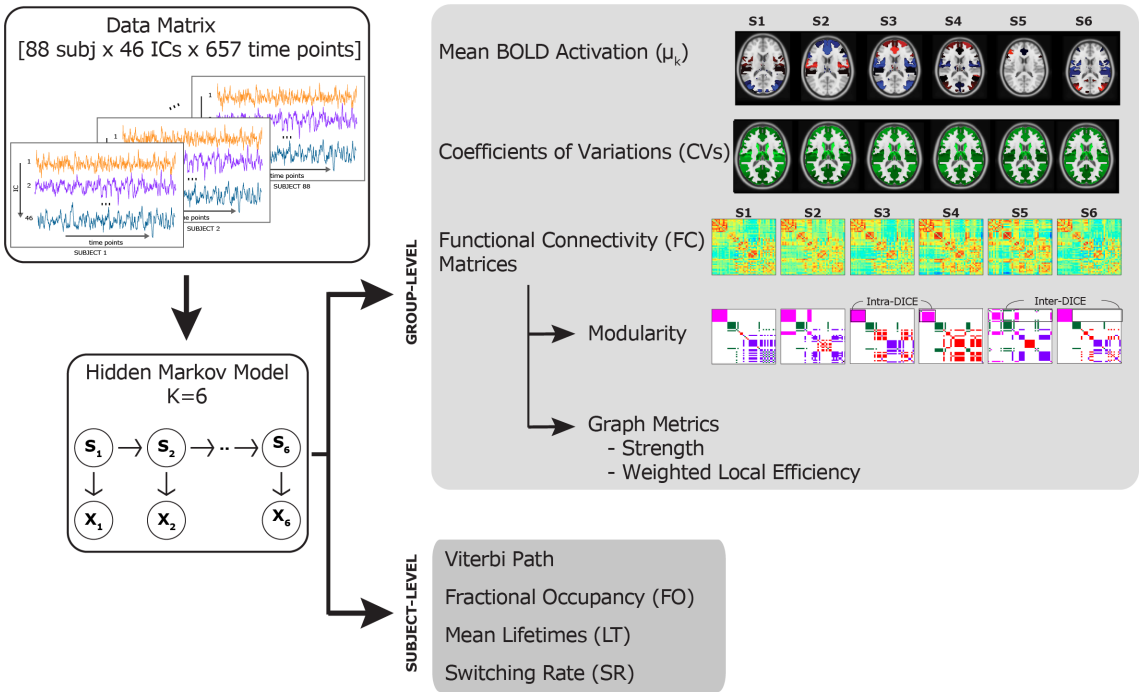

Figure 4.1: Scheme of the processing workflow employed for the analysis. Starting from the data (matrix of dimensions 88 subjects×46ICs×657 time points) a Hidden Markov Model with six states was inferred.

4.2.9 Relation between switching rate and behavior

Ultimately, we assessed whether there was a relation between switching rate and behavioral scores derived from cognitive tests.

Behavioral tests selection

Among the cognitive tests available in the public repository (Babayan et al. 2019), we selected the most informative test scores, some of which were then transformed or combined to facilitate the interpretation of the results. A brief description of these tests, as well as the transformations/aggregations done, are reported in Table 4.1.

Principal Component Analysis

The resulting set of behavioral metrics was then z-scored and used as input for a Principal Component Analysis (PCA) to identify the most important tests which were then used for the subsequent analysis. Specifically, the first three

PCs (which explained the 25.9%, 15.1% and 14% of variance, respectively) were subjected to oblique (Promax) rotation, then the scores with higher loadings in the first component were retained (threshold = 0.3). Four metrics were selected (i.e., CVLT, LPS, WST_IQ and TMT) and used as predictors in the subsequent logistic regression analysis.

Logistic regression model

A logistic regression model was built to predict individual SR values from behavioral scores of different cognitive domains. To this end, SR was first binarized using its mean as cut-off value: values above this cut-off were categorized as "high SR" (24 over 52 "high SR" were associated to young people), while values below were considered "low SR" (24 over 52 "low SR" were associated to young people). In the logistic regression model, the SR was used as dependent variable and the four metrics identified by the PCA as predictors.

Behavioral Tests				
Test	**Original metric code**	**Metric description**	**Transformation**	**Metric interpretation (code)**
CVLT	CVLT_6	Sum of all correct recalls from 1^{st} until 5^{th} trial	We performed a PCA on CVLT scores to reduce the redundancy of CVLT metrics and to avoid collinearity in the subsequent regression model. To this end, only CVLT PC1 (95% of explained variance) scores were used in the subsequent analysis.	PC1 of CVLT scores could be interpreted as a comprehensive memory score (CVLT)
	CVLT_8	Number of correct recalls from the interference task		
	CVLT_9	Number of correct recalls (short delay)		
	CVLT_11	Number of correct recalls after 20 minutes (long delay recall)		
LPS	LPS1	Number of symbol-rows correctly processed	-	Logical deductive thinking (LPS)
WST	WST3	IQ-scale	-	Intelligence Quotient (WST_IQ)

RWT	RWT_8	Number of s-words named in total (according to rules)	-	Phonemic fluency (RWT_pho)
	RWT_13	Number of animals named in the first minute (according to rules)	A global semantic fluency score across two minutes time was computed as: RWT_13 + RWT_17	Semantic fluency (RWT_sem)
	RWT_17	Number of animals named in the second minute (according to rules)		
TAP Alertness	TAP_A_15	Phasic alertness	-	Phasic alertness (TAP_PA)
TAP I	TAP_I_9	We computed the so-called Simon effect as follows: (TAP_I_9 – TAP_I_2) / TAP_I_2	-	Simon effect (TAP_Simon)
	TAP_I_2	Median time for compatible stimuli		

TAP Working Memory	TAP_WM_6	Number of correct matches	-	Working memory (TAP_WM)
TMT	TMT_1	Time it took to connect numbers (TMT-A)	We computed the ratio TMT_5/TMT_1 to isolate the set-switching component of the TMT	Task-switching performance (TMT)
	TMT_5	Time it took to connect numbers and letters (TMT-B)		

Table 4.1: Description of cognitive tests. The table shows the available metrics and the transformation that was eventually applied to ease their interpretation in the subsequent analyses. TAP I is for TAP Incompatibility.

4.3 Results

4.3.1 Choice of initialization algorithm

The lowest FE value of the best realization among the 200 for the two initialization algorithms tested and varying the model orders is reported in the first two columns of Table 4.2. The third column reports the range of the Spearman correlations (ρ) computed between the μ_k estimates of the best realization for the two distinct types of initialization. In the last column, the similarity between Γ obtained for the best realization for the two initialization and computed through the Munkres algorithm, is reported.
Given that the differences in the FE between the two types of initialization were almost negligible and that these differences did not affect the results obtained for the μ_k estimates and for Γ, the HMM-MAR initialization was employed for further analysis.

Model order	**Random initialization**	**HMM-MAR initialization**	**Range of ρ between μ_k**	**Munkes similarity between Γ**
2	2767676.8	2767676.6	0.99*	0.99
3	2746037.8	2746036.8	0.99*	0.99
4	2734664.2	2734664.4	0.99*	0.99
5	2725354.3	2725354.5	0.98-0.99	0.99
6	2717208.5	2717131.4	0.69-0.98	0.85
7	2710016.4	2709337.5	0.50-0.97	0.59
8	2702429.5	2702596.8	0.61-0.98	0.60

Table 4.2: In the first two columns the lowest value of free energy obtained among the 200 realizations of the model for the two initialization algorithms and for model order from 2 to 8 is reported. In the third column we reported the range of the Spearman correlations ρ computed between the μ_k estimates of the best realization for the two different types of initialization and in the last column the similarity between the Γ obtained for the best realization for the two initialization and computed through the Munkres algorithm. *All the values of ρ resulted to be equal to 0.99, thus a range is not provided.

4.3.2 Choice of the model order

Table 4.3 reports the values of the indices evaluated for the choice of the model order.
The FE had a decreasing trend as the number of states increased, showing no negative peaks, thus it was not informative for model selection purposes. Both AIC and BIC were not informative too, as they suggest the lowest order (K=2).

The avLL always assumed negative values. This is also the reason why, when implementing AIC and BIC formula, both the indices suggested the lowest order. However, the avLL showed a non-monotonous trend, with a maximum peak value reached for K=6, corresponding to the maximization of the log-likelihood in the tested range of K.
To investigate if the model with 6 states led to reliable estimates of the parameters, we also quantified the CVs of the estimates as the model order increases and then we computed the ratio between the standard deviation of the CVs and their average value, obtained by averaging across ICs and states.
As shown in the last column of Table 4.3 among different model orders, the ratio was almost comparable, and, as expected, showed an increasing trend as K increased. In terms of homogeneity within each state, the configuration with K=6 resulted the best.
Thus, considering avLL and the reliability of the estimates through the CVs, we set K equal to 6.

Model order	FE	avLL	AIC	BIC	std/mean
2	2767676	-18285	276680	1352976	0.17
3	2746036	-21496	403162	2017627	0.19
4	2734664	-28209	536653	2689307	0.19
5	2725354	-27130	654562	3345422	0.19
6	2717131	**-26139**	772651	4001735	**0.19**
7	2709337	-29693	899836	4667162	0.20
8	2702429	-28785	1018101	5323687	0.20

Table 4.3: Different indices for the choice of the model order obtained after the inference at the group level (i.e., combining young and old subjects together) are reported. In the first column the lowest free energy value, obtained among the 200 realizations is reported. Starting from this value, we computed the average log-likelihood (second column), Akaike (third column), Bayes Information Criterion (fourth column) and ratio between the std and mean values computed on the averaged CVs within a state (fifth column). The two indices that were informative for the model selection are marked in bold.

4.3.3 Group-level characteristics of brain states

Mean activation (μ_k)

For each brain state (henceforth referred to as S1, S2, S3, S4, S5 and S6), Figure 4.2 shows the spatial distribution of the μ_k estimates at the whole-brain level. For visualization purposes, the spatial map of each state was thresholded by setting the lower threshold to half of the maximum absolute mean value and the higher one to the maximum absolute mean value, respectively for positive and negative

μ_k values in that particular state. Negative activations are displayed in blue-scale and positive activations in red-scale.
The highest positive values in S1 are associated with the AUD and CON domains, whereas the negative with the VIS and DAN (Figure 4.2, panel A). In S2, the SMN, AUD and CON show higher positive deviations from the average, whereas the DMN, FRN and CER higher negative ones (Figure 4.2, panel B). S3 highlights positive values for the DMN, FRN and CER, whereas negative values are associated with SMN, AUD, DAN (Figure 4.2, panel C). In S4, positive values are associated with the AUD, FPN, FRN and CER, whereas negative values with the BG (Figure 4.2, panel C). S5 shows positive values associated with AUD, CON, FPN, CCN and FRN and negative values associated with DMN, CER, BG (Figure 4.2, panel E). S6 highlights positive values for the DAN, CER and for most ICs of the VIS and DMN. Negative mean values are associated with the AUD, CON, FRN, BG (Figure 4.2, panel F).
In Figure 4.3 for each IC and brain state the associated mean activation value is represented.

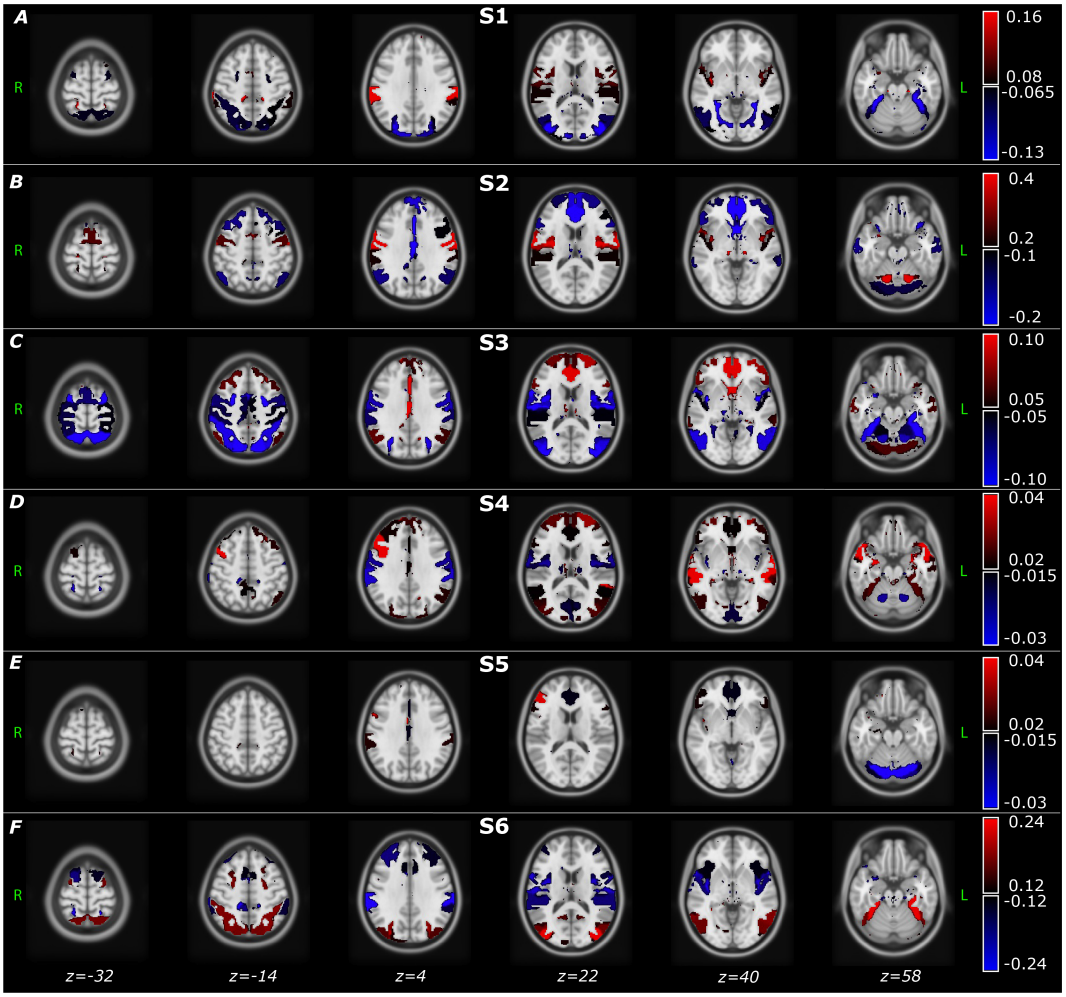

Figure 4.2: Each panel shows the axial view of the spatial distribution of the mean BOLD activation (μ_k) estimates, obtained for each brain state. Since the HMM was inferred at the population level, that is, concatenating the IC time courses of young and old participants, the μ_k values are group-level estimates. Color bar values range from half of the maximum absolute mean value to the maximum absolute mean value, respectively for positive and negative μ_k values obtained in each state. ICs with mean activation values out of these bounds are not displayed. Negative values are displayed in blue-scale, whereas positive values in red-scale. The spatial distributions are overlaid to the MNI atlas, shown in gray scale.

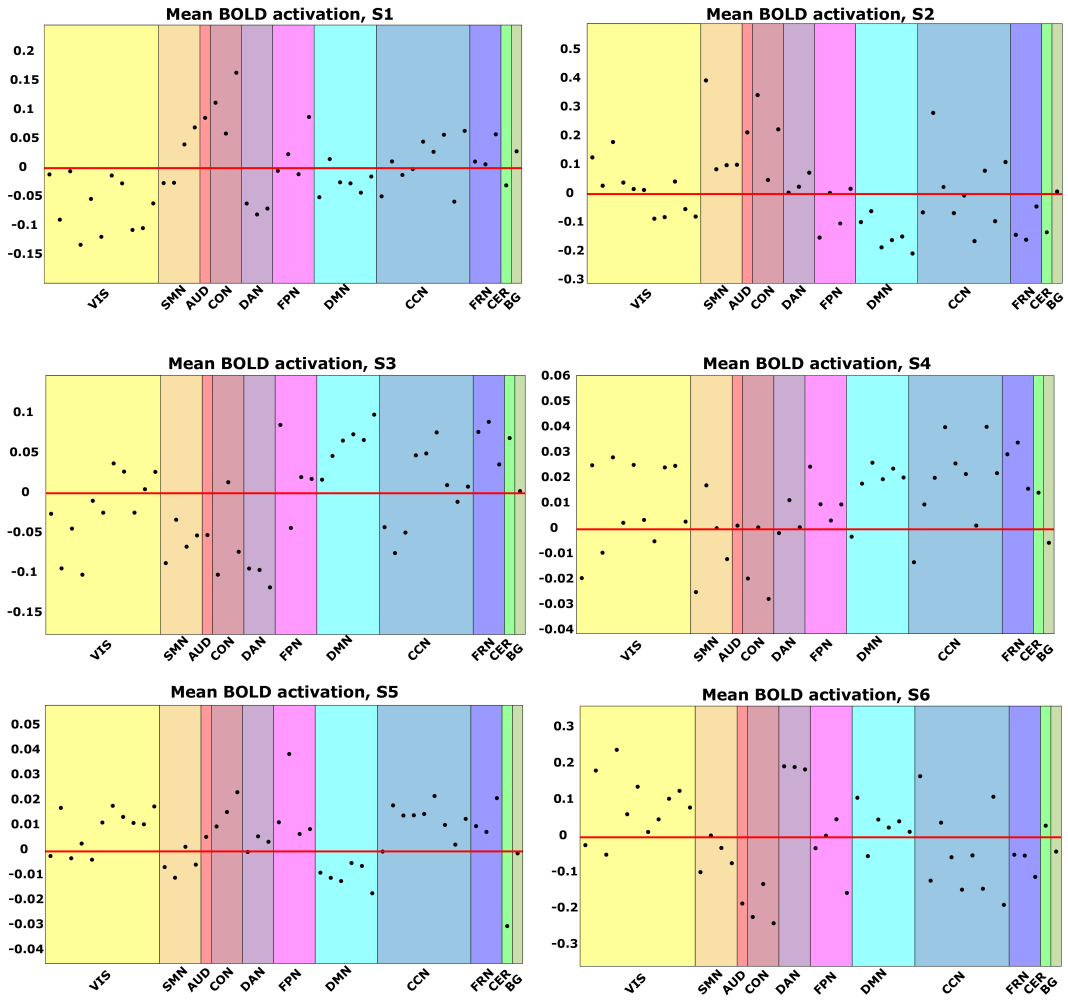

Figure 4.3: Each figure shows, for each brain state and each IC, the associated mean activation value (μ_k), depicted by black dots. The red line, set at 0, separates positive and negative μ_k values.

Reliability of the states

To quantify the precision of the μ_k estimates presented above, we computed the CVs.
In Figure 4.4, we reported for each IC and brain state the associated CVs.
Figure 4.5 shows the spatial distribution of the ΔCVs in green scale and, for a better comparison between the six states, the colorbar values range from -35% to 35% with respect to the average CV value within each state.
Ranking the most reliable states in terms of CVs, resulted in S4 ($\overline{CV} = 47.6\%$), S3 ($\overline{CV} = 51\%$), S5 ($\overline{CV} = 51.5\%$), S1 ($\overline{CV} = 53\%$), S6 ($\overline{CV} = 60.4\%$) and finally S2 ($\overline{CV} = 70.4\%$).
Overall, when comparing the reliability across states and within functional domains, the μ_k values associated with the DAN show the highest reliability, whereas those associated with FRN, CER and BG are the least reliable in all the states with CVs above the average level, as shown in Figure 4.5 in bright green.
These results imply that the DAN network is, among all, the most reliable, in terms of precision of the estimates, in its representation within each state. Although CV values of all the SMN components were over the average in S1, S2 and S6, for all the other functional domains the trend of the CVs could not be summarized among states.

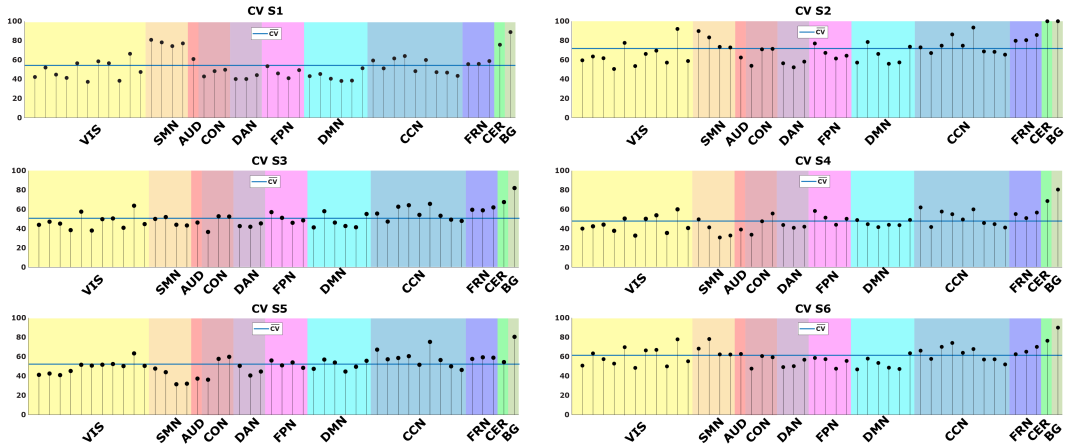

Figure 4.4: Each figure shows, for each brain state and each IC, the associated coefficients of variation (CVs), depicted by black stems. The blue line represents the average CV ($\overline{CV}$) within the state.

4.3.4 Subject-specific temporal characteristics

Transition probabilities matrices

In Figure 4.6, the Viterbi paths and the probabilities of transition, without considering the probabilities of persistence in the same state (i.e., the diagonal of the

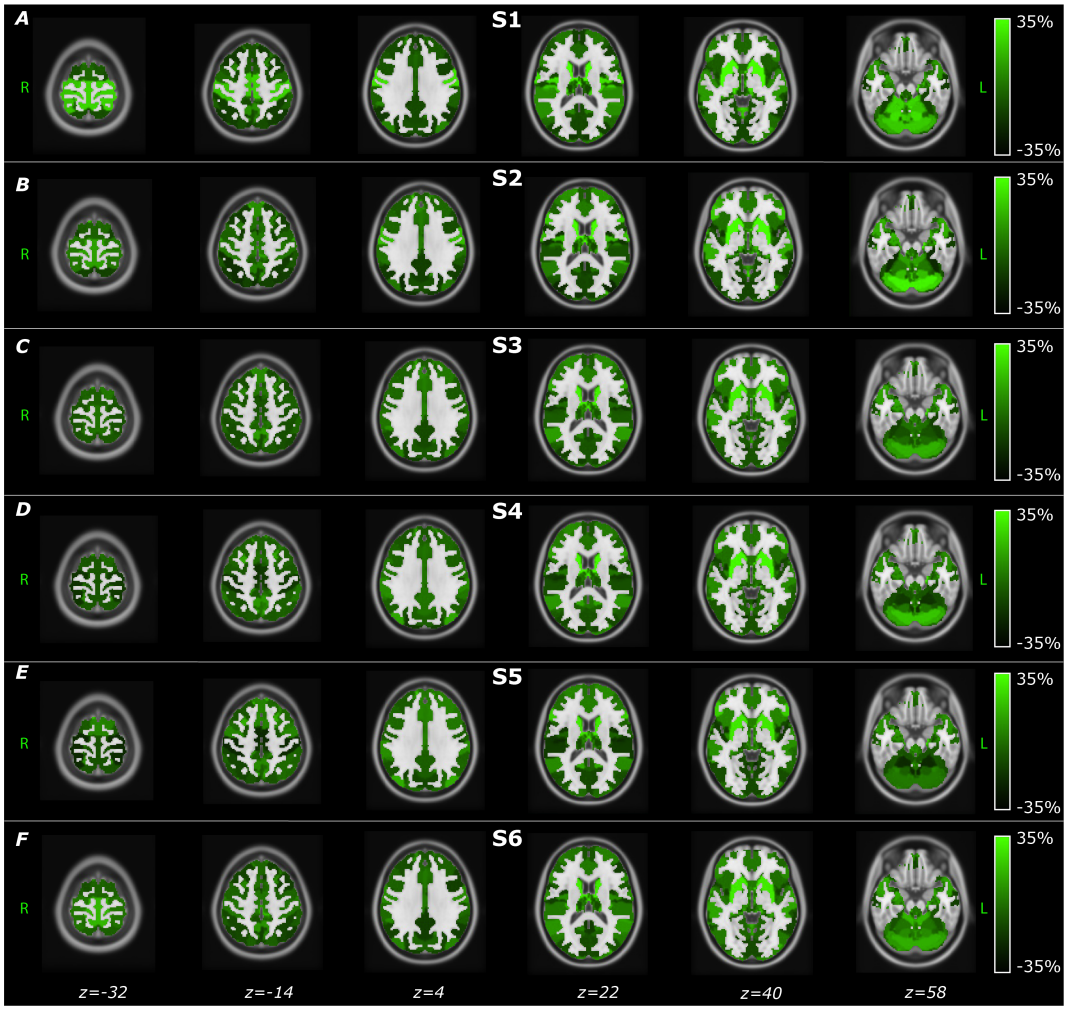

Figure 4.5: Spatial distribution of the distance between each IC's CV and the average CV among ICs within the same state (δCVs) obtained for each brain state. Since the model was inferred at the population level, that is, concatenating the IC time courses of young and old participants, these maps represent group-level estimates. Positive values represent an increment in CV with respect to the mean value of the CVs obtained in each state. Therefore, bright colors are associated with more uncertain ICs. The spatial distributions are overlaid to the MNI atlas, shown in grayscale.

Θ_k matrix), are reported for the two groups separately. Particularly for the young subjects (Figure 4.6 panel B and C), the probabilities are higher among S6 and S1 (prob=0.56), S4 and S1 (prob=0.48), S1 and S6 (prob=0.45). Whereas for the old subjects (Figure 4.6 panel E and F), the transition probabilities are higher among S2 and S3 (prob=0.63), S6 and S3 (prob=0.49), S3 and S2 (prob=0.47). Interestingly, both the dynamic of the transitions is characterized by the presence of one loop, composed by different states through the young and old, but with the same behavior, i.e., when a young subject reaches S1, he seems to circle between

S6 and S1 in a closed loop, while, when and old subject reaches S3, he holds in a circle between S2 and S3. As highlighted in the corresponding spatial maps, the first set of loops (Figure 4.6, panel C) involved mainly occipital and parietal regions, while the second set (Figure 4.6, panel F) frontal regions.

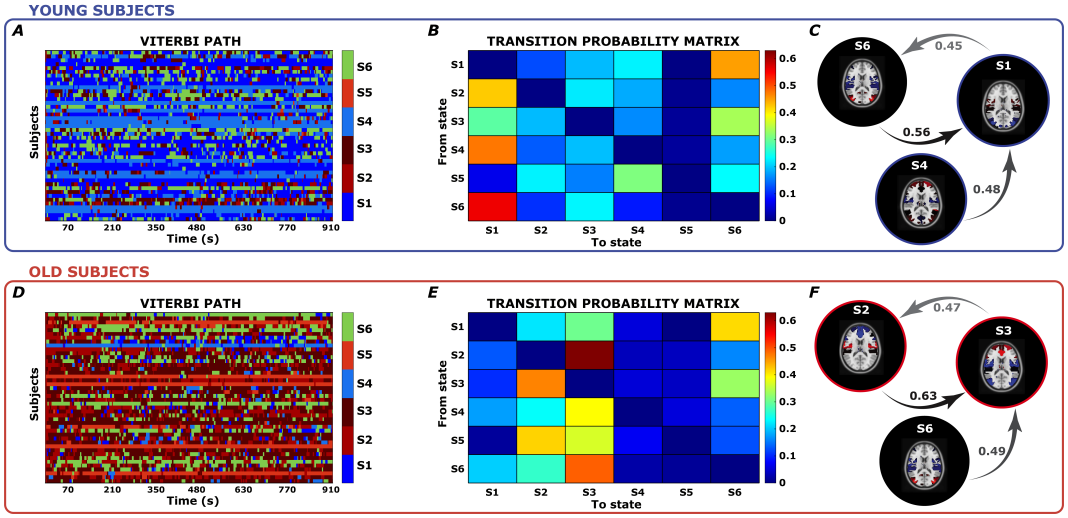

Figure 4.6: In panels (A) and (D), we report for the young and old respectively, the Viterbi path computed for each subject, in the y-axis, and for each time point, in the x-axis. Different colors are assigned to distinct states. In panels (B) and (E) the transition probabilities from one state (y-axis) to another (x-axis), for the young and old, are reported. Finally, panels (C) and (F) show the three top most likely transition probabilities and links.

Chronnectome

The differences between the two groups are evident when comparing the aforementioned state-relevant temporal metrics.
In Figure 4.7 we show the fractional occupancy distribution, obtained for the two groups in each brain state. On average, the time spent from the young subjects in S1 was 39% of total rs-acquisition and in S4 28%. While the old subjects spent 20% of the time in S2, 39% in S3 and 12% in S5. Instead, S6 was characterized in equal proportion by both the groups: 18% by young and 19% by old.
The K-S test pointed out statistical differences (p-value$<$0.01) between groups: young subjects spend more time in S1 and S4, whereas old subjects in S2, S3 and S5. Instead, the time spent in S6 did not significantly differ between young and old.

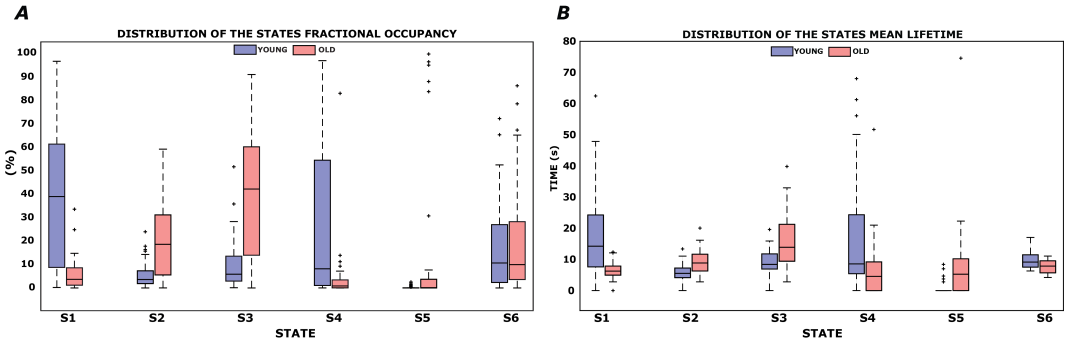

Figure 4.7: In Panels (A) and (B), the distribution in different states of fractional occupancy and mean LT, respectively, is reported in blue for the young subjects and in red for the old subjects. The bottom and top edges of each box indicate the 25^{th} and 75^{th} percentiles. The outliers are represented by the "+" symbol. In each boxplot, the solid line indicates the median, so for example, the median value of the FO for young subjects in S1 is 39%.

To give an overview of the states through the features described so far, in Figure 4.8 we report for each brain state, the group of subjects (young/old) most persistent in that state, resulting from the FO analysis, and an illustration of the μ_k patterns in each functional domain. These patterns were obtained by averaging the ICs absolute μ_k values within each functional domain and then percentualizing them on a scale from 0 to the maximum value obtained among the states (0.2). As can be seen by the labels above each panel, while S1, S2, S3 and S6 show high activation of RSNs belonging mostly from extrinsic domains, the remaining states, S4 and S5, exhibit an overall mean level of BOLD activation. To note that the states for which we registered the highest activations, have also the worst average CV, but across the states the highest activations are associated with the CON and AUD functional domains that have good precision and consequently reliability of the results (see Figure 4.5 for further details).

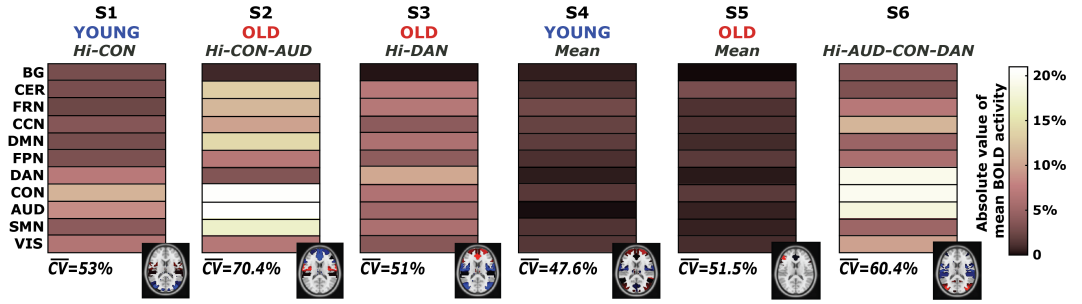

Figure 4.8: Characteristics of the inferred brain states. The 11-segment bars provide a summary of the mean absolute BOLD activation within each functional domain, expressed as a percentage distance from the mean level of activation. The labels above each image describe the group of subjects who most persist in that state (young/old) and the strongest functional domain in that state at the average activity level. Hi=high BOLD activation. The term "Mean" refers to baseline states where the RSNs present a mean level of BOLD activation. At the bottom, the average CV value within each state is also reported.

4.3.5 Brain states graph metrics

Strength and Local Efficiency

In Figure 4.9 we report the states FC matrices, from which, after proportional thresholding, we computed the STR, EL and modularity indices.
Since the FC matrices were obtained at the group-level, without distinction between the two subgroups of young and old subjects, the graph metrics and modularity indices are representative of the whole population.
The states did not differ in terms of global properties of the associated graph: no statistically significant difference was found in the node strength distribution. Nonetheless, for this metric, S4 and S5 resulted to have the highest values (on average: $STR_{S1} = 4.1$, $STR_{S2} = 4.02$, $STR_{S3} = 3.93$, $STR_{S4} = 4.73$, $STR_{S5} = 4.46$ and $STR_{S6} = 3.73$). On the contrary, statistically significant differences (p-value$<$0.01) were found at the local level, where the local efficiency of states S4 and S5 was significantly greater than in states S2, S3 (on average: $EL_{S1} = 0.36$, $EL_{S2} = 0.34$, $EL_{S3} = 0.34$, $EL_{S4} = 0.42$, $EL_{S5} = 0.38$ and $EL_{s6} = 0.33$).
In Figure 4.10 we report the results of the analysis carried out at the functional domain level, for the STR and the EL measures, respectively. Taking into account only the extreme values exceeding ± 1.5std, we found that in S1 the STR of DMN was significantly higher than in the remaining domains; in S4 the same happened for the VIS domain and in S5 in FPN domain, whereas negative deviations from the average (i.e., low STR) were found for S2 in FPN and for S6 in CON.
Considering the EL, we found only positive deviations and in particular for S4 in

AUD, CON and CCN, for S5 in FRN. Taken together, these results confirmed our hypothesis that moving to a more detailed characterization of the graph represented by the specific domains, a better description of the states in terms of STR and EL is possible. In particular, we were able to capture specific properties, especially for three states (S1, S4, S5), that presented more integrated behavior in different functional domains.
Furthermore, this analysis confirmed the added value of the information provided by the BOLD activation parameter (μ_k), with others derived from a deeper investigation of some properties of the nodes at the graph-level. In fact, even if some functional domains did not exhibit a high BOLD activation, they resulted to play a crucial role at the graph-level. For example, while the DMN showed low BOLD activation in S1, it was the only domain to present the highest STR, suggesting its potential role of hub in that particular state.

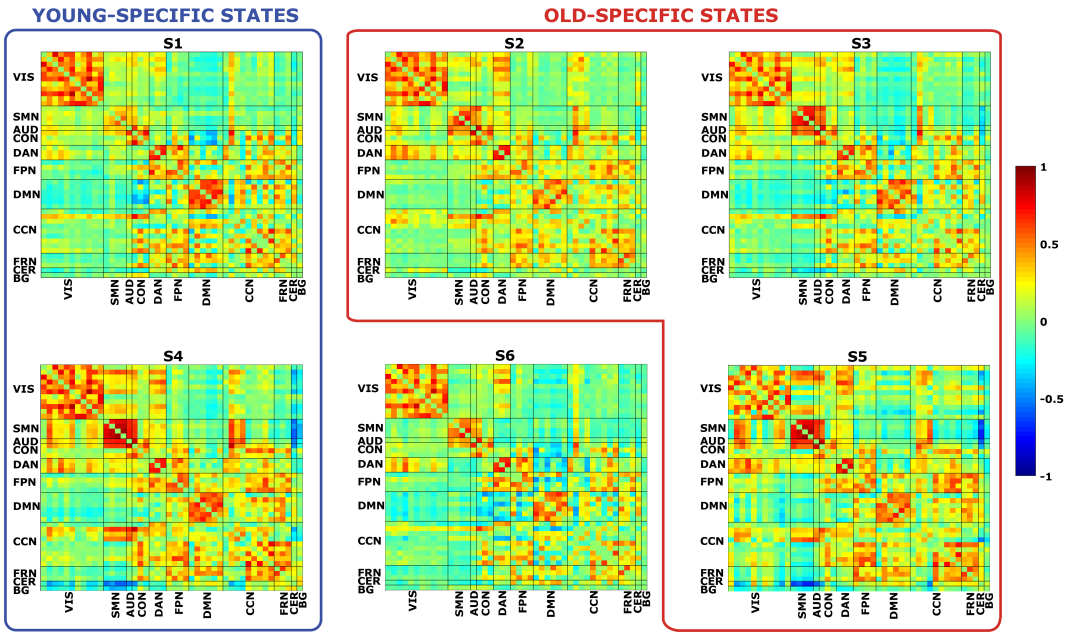

Figure 4.9: Each panel represents the FC matrix associated to a particular brain state (S1, S2, etc.). In both the x- and y-axis, we have the 46 ICs, divided in the 11 functional domains. Warm colors represent high positive correlations values between ICs, whereas cool colors represent high anti-correlations values. We grouped together states mostly populated by young subjects (blue box) and by old subjects (red box).

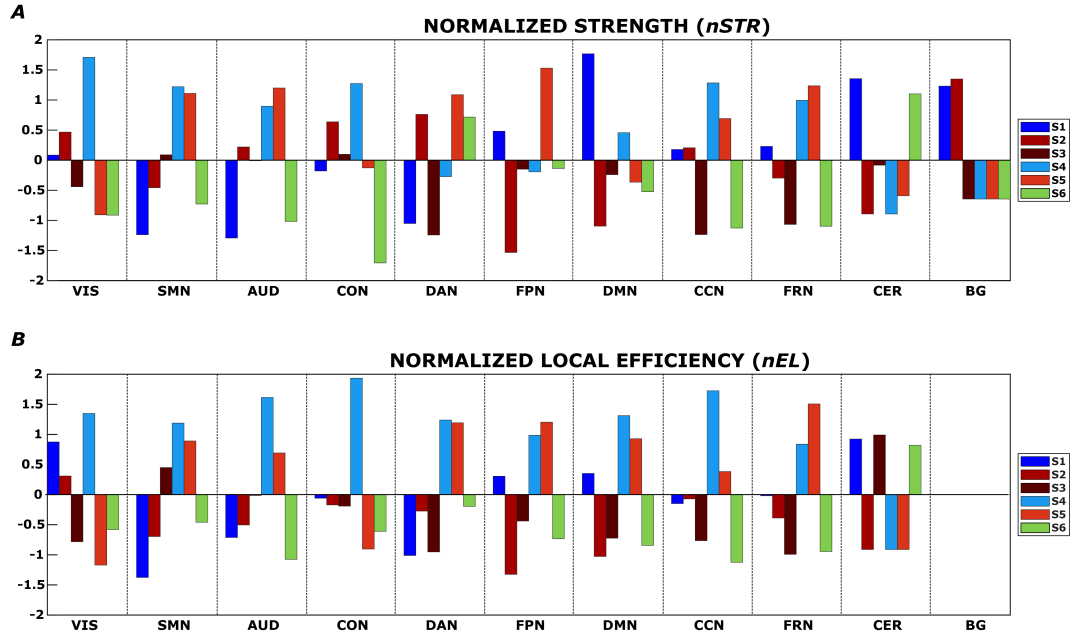

Figure 4.10: In Panels (A) and (B), we show the normalized values of the strength (nSTR) and local efficiency (nEL) for the states, colored differently, and in the functional domains. Given that, after proportional thresholding of the FC matrices, the local efficiency resulted to be 0 for the basal ganglia (BG) in all the states, in Panel (B) no values of nEL are reported for the BG. The labels S1, S2, and so forth refer to State 1, State 2, and so forth.

Modularity

In Figure 4.11, for each state we depict the modular organization derived from multiple repetitions of the Louvain's community detection algorithm. Instead of the classical graph representation for the module assignment, we arrange the results in a matrix form to better highlight the assignment of each IC to a specific module and how this relates to the assignment of the other ICs.
In the same figure we also report the states modularity index, obtained by averaging across the 50000 realizations. Even if no differences were found in this metric, we can notice a trend in our results, in particular, S5 assumes the lowest value of modularity, reflecting a situation of integration between networks, whereas S1 shows the highest value, reflecting a segregation of the networks, which is confirmed by the number of detected communities that resulted to be 4 for this state and 5 for all the others.
Interestingly, even if S5, an old-specific state, followed by S4, a young-specific state, presented a low modularity in comparison to the others, they also exhibited the highest values for STR and EL, as reported before.
We tested an upper threshold at the 10^{th} percentile of the distribution and another at the 15^{th} percentile. For the inter-Dice results, no differences were found between the two thresholds, whereas for the intra-Dice results the involved functional domains resulted to be the same (i.e., FPN, DMN and CCN) between the two thresholds, with some additional differences in the FPN and CCN for the threshold set at the 15^{th} percentile. Thus, to highlight the strongest differences, we fixed a threshold at the 10^{th} percentile of the DICE distribution which corresponded to an intra-Dice of 0.59 and an inter-Dice one of 0.
At the intra-domain level, we found differences between states only in cognitive domains, i.e. FPN, DMN and CCN. Indeed, S1 presented a disruption of the FPN, that is reflected in low intra-Dice values between this state and S2, S3, S5, S6. In S2, which differed from all the others, we observed a loss of segregation of the DMN and finally, in the CCN S5 differed from S1 while S3 from S4.
On the contrary, many more alterations were detected at the inter-domain level and in distinct domains, namely VIS, DAN, DMN, CER and BG. Specifically, S2 and S5, in contrast to the others, presented a VIS integrated with DAN components. The DAN differed notably across states at the inter-domain level, in fact except for the pair S2-S5, all the others presented an inter-Dice of 0, which can be explained by a segregated DAN in S1 and S6; a DAN integrated with various components of CON, FPN, CCN, FRN in S3 and a DAN integrated with only one component of CCN in S4.
Regarding the DMN, differences were found between S5 and S1, S4, S6 being these states more integrated. In the CER, the inter-Dice resulted to be 0 between states with a strong segregation of this network (S2, S4) and states with

high integration (S1, S3, S6). Furthermore, S5 differentiates from all other states. Finally, the inter-Dice of BG computed between S1, S2 and all other states resulted to be 0, being S1 and S2 integrated with many ICs.
The results of the modularity analysis performed at the functional domain level, are summarized in Figure 4.12.

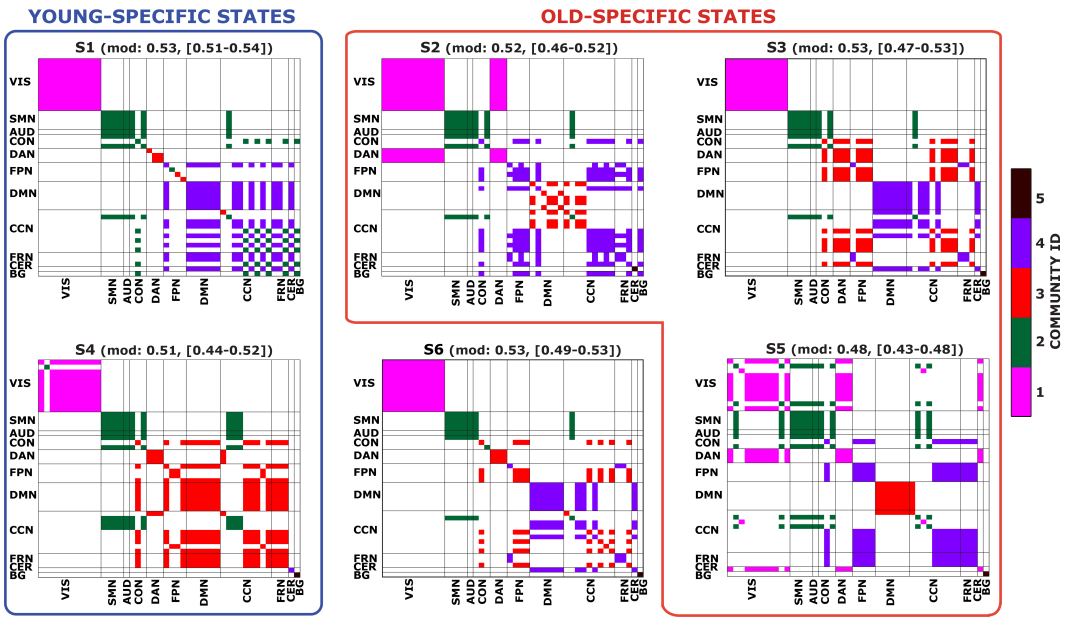

Figure 4.11: Each figure represents the modular organization of a brain state (S1, S2, etc.) obtained as explained in the main text. Different colors are representative of a distinct community. In both the x- and y-axis, we have the 46 ICs, divided in the 11 functional domains. In the title, we also report the mean modularity value, obtained across the 50,000 realizations, together with the minimum and maximum values. We grouped together states mostly populated by young subjects (blue box) and by old subjects (red box).

4.3.6 Relation between switching rate and behavior

Table 4.4 reports the PCA loadings, obtained on the cognitive data. Collinearity across predictors was checked by means of variance inflation factors (VIF), which were lower than 10, thus suggesting no potentially harmful collinearity (Bruce L. Bowermann 1990). The model resulted as significant ($\chi^2[4] = 10.33$, p=0.04, Cragg-Uhler's Pseudo-R^2=.15) and showed that SR was significantly related only with TMT score (z=-2.46, p=0.01). Specifically, a better (i.e., faster) performance was related to higher SR. We could speculate that an individual tendency to frequently switch between states could relate to a better task-switching ability. Interestingly, subjects with high SR (N=52; 28 O) tend to occupy more frequently state S3. As reported previously, S3 was characterized by high involvement of

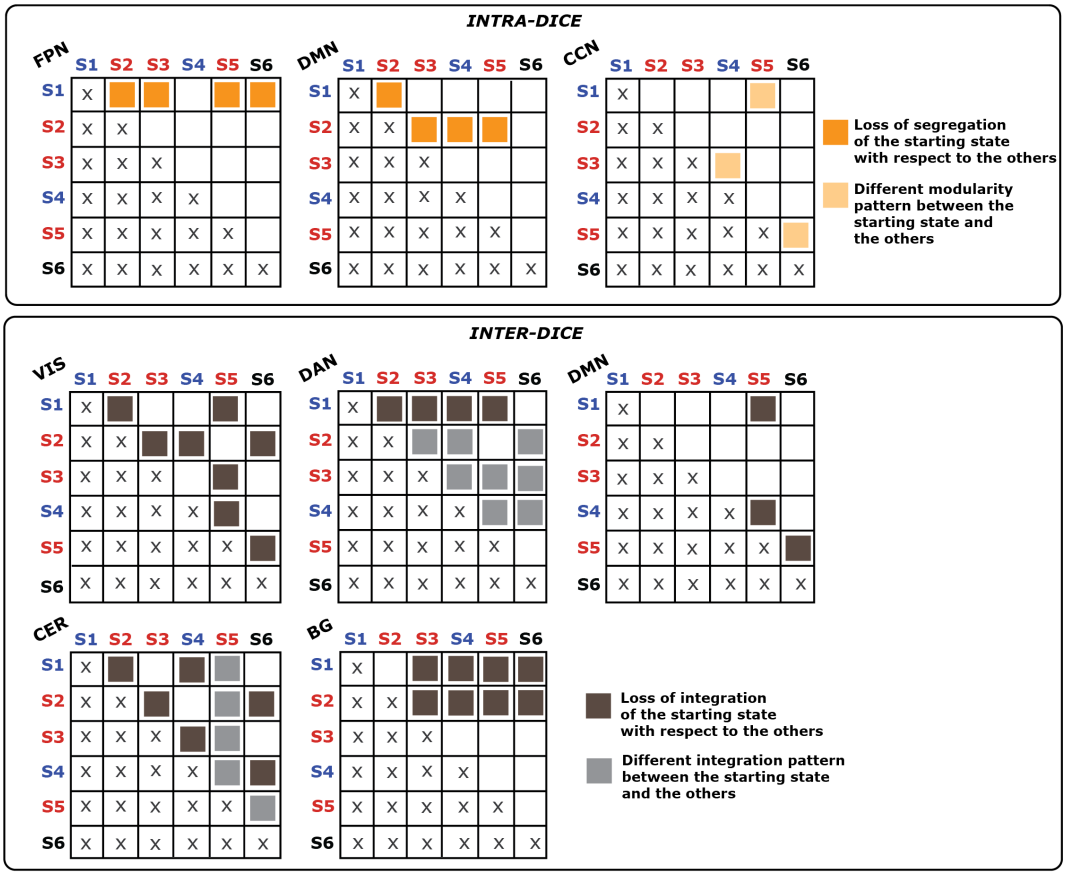

Figure 4.12: Summary of the intra/inter-Dice analysis. Each symmetric matrix shows for a specific functional domain (reported in the left corner), the pairs of states that resulted to have an inter-Dice below the 0.59 threshold or an intra-Dice of 0. Given that many differences were due not to a lack of domain segregation/integration in one state versus another, but rather to a different pattern of segregation/integration between RSNs, a dull color was used to represent these situations. States colored in blue are the young-specific and in red the old-specific. Domains not affected by this analysis are not reported. Given the symmetry of the matrices, the symbol "x" was placed on the lower triangular matrix.

the DMN, which has been related to task-switching performance (Crittenden, Mitchell, and Duncan 2015; V. Smith, Mitchell, and Duncan 2018), also in aging (J. Damoiseaux et al. 2008). This is also consistent with the role of the DAN in S3, which communicated with many ICs of cognitive domains.

On the other hand, CVLT, LPA and WST_IQ did not show significant effects. As a control analysis, we also repeated the same logistic model including age as covariate and the results were confirmed (TMT z=-2.44, p=0.01). This relative independence of SR from age suggests that SR could be considered as a trait, i.e.,

a relatively stable characteristic throughout the lifespan.

Metric	PC1	PC2	PC3
CVLT	**0.49**	0.34	0.002
LPS	**0.54**	0.05	-1.16
RWT_pho	0.19	0.59	0.08
RWT_sem	-0.09	0.64	-0.03
TAP_PA	0.13	0.01	0.44
TAP_Simon	-0.23	0.19	0.46
TAP_WM	0.08	-0.05	-0.58
WST_IQ	**-0.51**	0.29	-0.47
TMT	**-0.31**	0.02	0.003

Table 4.4: PCA loadings. Matrix of promax rotated loadings obtained in the PCA run on the cognitive data. Values in bold are those with absolute value higher than the chosen threshold = 0.3.

4.4 Discussion

In this chapter we have explored the effects of normal aging in the spatiotemporal organization of brain states, carrying out a data-driven analysis based on HMMs. After modelling the ICs time courses obtained at the whole-brain level, we implemented a novel method to select the optimal order of HMM in a quantitative manner by balancing the model complexity with the precision of the hidden parameter estimates. Then, we derived 6 states and characterized them by evaluating the properties of FC matrix of each state, and the mean level of BOLD activation of each RSN. In contrast to other approaches, one of the advantages of using this method is in that it allows the quantification of the CVs, an index about how uncertain the estimates of specific brain regions are. At the temporal scale, the states were described by the most frequent transition patterns between them. In this way we could derive the time spent in each state, the average duration of the state visits, and the frequency of transitions between different states. These metrics were compared between young and old subjects to investigate possible links between aging and temporal dynamics of brain states. From this analysis we could observe that two states, namely S1 and S4, were mostly occupied by young subjects, while three states, namely S2, S3 and S5, by old subjects. The remaining state, S6, was populated in equal proportion by the two groups. Moreover, given the extensive literature supporting the theory of increasing functional integration between networks with increasing age, we conducted a graph-based analysis that allowed us to distinguish states characterized by high network segregation rather than high integration. In particular, we found that

old-specific states exhibited an overall more integrated topology with respect to a more segregated in young-specific states. The findings reported are not expected to be driven by arousal differences between young and old subjects. Indeed, a recent study (Daneault 2021) has found no statistically significant differences in FC between young and old people and no interaction with age when comparing wakefulness and N1 during 100 minutes of eye-closed acquisition. It is of note that the subjects employed in our study were asked to keep their eyes-open for the entire duration of the acquisition and this should prevent N1 stage (Gu, Han, and Liu 2019). However, even if we assume that some of them fell into a N1 sleep stage, it does not foresee significant differences in FC between young and old, based on (Daneault 2021).

4.4.1 Model order choice

The choice to adopt HMM instead of others approaches to study dynamic FC, was driven by the possibility to select the model order in a quantitative way, exploiting the principle of parsimony that seeks to balance the goodness of the fit with the precision of the estimates. In fact, relying only on the free energy cost function, the optimal model would not be found, since with the increase of the model order, the free energy decreased, without showing minimum values able to lead us in the model selection. In contrast with free energy results, AIC and BIC indices showed their maximum value for model order equal to 2. To find the optimal model it was therefore necessary to introduce and evaluate other indices for different model orders, that are the average log-likelihood, as indicator of the goodness of the fit, and the CVs, as indicators of reliability of the estimates. To our knowledge, this is the first study that attempts to solve the model selection issue, making a compromise between the free energy, which pushes towards a hyper parameterized model and indices of parsimony that push towards a simplification of the model, also adding information about uncertainty of the estimates.

4.4.2 Group-level characteristics of brain states

At the spatial level, we obtained the maps of the mean level of BOLD activation, which allow us to distinguish high activation states (S1, S2, S3, S6) from baseline states (S4, S5) in which the RSNs present a mean level of activation. Almost all the spatial maps here presented show patterns in line with a previous work (Vidaurre, Abeysuriya, et al. 2018) that employed UK Biobank data and inferred 8 states, indicating that even with our small sample size, HMM application leads to reproducible results. Comparing our results with (Vidaurre, Abeysuriya, et al. 2018), we observed a match between: S2 and the SMN state; S3 and the DMN;

S6 and the VIS state. The only exception was for the primary visual that in our case are mapped in another state. This mismatch can be explained not only by the different sample sizes, but also by the different age of the sample and the different number of inferred states. The choice of the HMM for the study of the dynamic connectivity, also allowed us to quantify the uncertainty of the estimates through the CVs. Thanks to the introduction of this index in the study, we were able to distinguish areas associated with higher uncertainty, such as FRN, CER and BG, that were also consistent across brain states. As these three functional domains were found to be associated with worse CVs, the conclusions drawn about these domains in specific states should thus be taken with caution. From a physiological standpoint these results are not unexpected, as the BOLD signal in the basal ganglia and cerebellum has a quite different underpinning structure in comparison with cortical regions, both in terms of neuroreceptors (Palomero-Gallagher and Zilles 2018) and iron content (Cherubini et al. 2009).

4.4.3 Subject-specific temporal characteristics

In line with the study of Y. Xia et al. 2019 we found that the occupancy of the two groups in each state was statistically different: S1 and S4 populated mainly by young subjects, whereas S2, S3 and S5 by old subjects. This finding suggests a clear separation between occurring patterns of mean BOLD activation as well as FC in young people rather than in elderly. Even if no significant differences were found in the SR, we can note a positive trend with increasing age. This result is well in line with previous studies, which observed an increased SR in healthy elderly subjects (Malagurski et al. 2020) or a significant association between aging and SR increase in less performant older adults with low cognitive performances (Cabral et al. 2017). Moreover, in relation to the transition probabilities between states, we found for young subjects a main loop between S1 and S6 with high probability to remain in S1, the state with the highest segregation of RSNs, and on the other hand for old subjects, a main loop between S2 and S3, two very integrated states, where the DAN serves as a bridge for the integration between RSNs of different functional domain.

4.4.4 Brain states graph metrics

The graph-based analysis carried out on the sparse FC matrices, pointed out very interesting results, both considering the entire network or specific domains. Previous studies (Andrews-Hanna et al. 2007, J. Damoiseaux et al. 2008) suggested that the DMN components undergo a functional connectivity modification during aging. This result was confirmed by our analysis conducted at the functional domain level. Indeed, young-specific states had a much higher strength in the

DMN with respect to old-specific states. Many deviations from the average level were also found in the two baseline states: S4 exhibited the highest strength values in the VIS, and also local efficiency values in the AUD, CON and CCN. Instead, S5 revealed higher strength in the FPN and local efficiency in the FRN. The other two old-specific states, S2 and S3, did not show strongly above average behaviors, in fact both the strength and the local efficiency were in general below the average level, with a significant decrease of strength for S2 in the FPN. This network plays a central role in the executive functions, attentional processes and working memory, and many studies found an increased functional activity in the FPN during cognitively demanding tasks (M. D. Fox et al. 2006, S. M. Smith et al. 2009), but also a positive correlation between ageing and weaker within network connectivity (Betzel et al. 2014) and decreased local efficiency (Geerligs et al. 2015). Moreover, many groups detected an altered activation of the FPN both in mild cognitive impairment and Alzheimer disease (Agosta et al. 2012, Wang et al. 2012) that led to an impairment of the performances during cognitive tasks (Yetkin et al. 2006, Zanchi et al. 2017). Therefore, we suppose that the weak strength and local efficiency of the FPN in S2, could be associated with a cognitive decline due to age progression. In general, in literature an increased functional connectivity between RSNs in elderly has been reported (Betzel et al. 2014, Chan et al. 2014, Geerligs et al. 2015, J. Song et al. 2014) and it is hypothesized that this change is due to a loss of modularity and segregation between networks (Chan et al. 2014, J. Song et al. 2014). Our modularity analysis revealed that while S1, a young-specific state, was mostly characterized by a greater segregation of the networks, S5, populated only by the elderly, was the one that presented more integration between networks. The intra-Dice results highlighted loss of segregation in the CCN for S1, S4 and in the FPN for S1. This loss of FPN integrity together with the interaction between the BG and many ICs of cognitive domains, could shed light on the compensatory role of the BG for the maintenance of general cognition. Interestingly, in line with previous studies (Chong et al. 2019, J. Damoiseaux et al. 2008) that reported the association between older age and lower functional integrity in the DMN, we detected a loss of integrity of the DMN only for the old-specific S2. In summary, we found that young-specific states presented low segregation in the FPN and CCN, and high integration of the DMN, while old-specific states an overall more-integrated topology, especially between the DAN and many other domains, but also different patterns of integration rather than segregation of the DMN. The organization of RSNs in a more integrated-topology is confirmed by a previous study (Bagarinao et al. 2019), which performed analysis at the network-level and found a decrease in the shortest path length and an increase in global efficiency with age (J. Song et al. 2014).

4.4.5 Limitations

This study is not exempt from limitations. First, we inferred HMM to the time series of all the subjects together, without distinction between young and old, thus obtaining parameters estimates at the group-level. An alternative approach would have been to fit the model separately for the two groups and thus to describe properties specific to the population of interest. However, this would have significantly increased the number of parameters to be estimated and, with the relatively low sample size at disposal, no such reliable estimates would have been obtained. Moreover, it would not have allowed a direct comparison between state metrics of the two different models. Regarding limitations, some might raise the issue that movement may affect the results. However, we found low values of FD in both the groups (on average 0.11mm for young people and 0.17mm for old people) and the pre-processing we followed through ICA included discarding motion-related components and a subsequent despiking step on the IC's time courses. Thus, we cannot find any reason to support that our findings are driven by motion differences between young and old people.

4.5 Conclusions

In this study we performed a whole-brain dynamic functional connectivity analysis, through Hidden Markov Models, to characterize brain states in the healthy aging population. This approach embeds the entire population heterogeneity in the model and allows to decode the dynamics of the time-varying functional connectivity and to capture the individual transitions between brain states. We selected the best model in an automatic and mathematically reliable way and, to our knowledge for the first time, we provided a tool to quantify the uncertainty of the estimates. The results showed that different states and within them specific brain regions, have distinct levels of accuracy, therefore caution must be paid in the physiological interpretation of the results. Indeed, among the 6 inferred states, we found the DAN associated to the most accurate μ_k estimates, while the FRN, CER and BG to the least ones. Moreover, we found that the time spent in each state was different among groups, in fact in terms of fractional occupancy, a clear separation between states was observed. This allowed us to define young-specific states rather than old-specific states. The graph-based and modularity analysis revealed an overall more integrated networks topology in old-specific states. We also found an increase in strength with increasing age in the DMN, which can be explained by the highly integrated topology of this network in young-specific states. On the contrary, in old-specific states the DMN was found to be highly segregated or to lose its integrity. Furthermore, we observed that the transitions between states were not random, but more likely to occur between specific states

and following preferential paths. For young subjects these paths were characterized by states at high segregation of the networks. On the contrary, old subjects fell in a loop of states where the networks were very integrated, and the DAN acted as a connecting point for the network communication. Although previous studies assumed the stationarity of functional connectivity during the resting acquisition, our results instead suggested a continued transition between states, characterized by different patterns of connectivity between networks. Therefore, static approaches cannot be sufficient to capture the rich dynamics governing transient brain states in the aging population.

Chapter 5

Dynamic FC in patients with high-grade gliomas

5.1 Introduction

Patients with high-grade gliomas exhibit more pronounced cognitive deficits with respect to low-grade gliomas patients. The presurgical cognitive status has been shown to be strongly associated with patients' survival (Kessel et al. 2021; Meyers et al. 2000), highlighting the importance of cognitive functions assessment for patient care and treatment. The preservation of cognitive functions is one of the major goal in treatment and surgical planning (Klein, Duffau, and De Witt Hamer 2012) since it is of paramount importance with regard to the social integration and patients' quality of life, it should play a decisive role in treatment planning and surgical intervention.
In this regard, studying how functional networks distribute in the brain can be useful, as increasing evidence underlines that cognitive deficits in tumor patients exceed local tumor effects and rather depend on spatially-distant networks (Hacker et al. 2019; Harris et al. 2014).
Studies investigating possible alterations of resting-state FC within and between RSNs in brain tumor cases are very scarce and only a few number of papers have been published on this topic so far (Harris et al. 2014; R. Esposito et al. 2012; Ghumman et al. 2016; Maesawa et al. 2015; Jütten et al. 2020; De Baene, Rutten, and Sitskoorn 2019).
A common finding among studies is the decrease in overall DMN connectivity in patients as compared to control groups (Ghumman et al. 2016; Maesawa et al. 2015; Harris et al. 2014). Furthermore, compared to low-grade gliomas, high-grade gliomas seemed to cause a major impact on rs-FC, leading to largest reductions of DMN integrity (Harris et al. 2014).
Although some reports exist on this topic, studies on functional dynamics in brain

tumors are still missing in the literature. Indeed, all the studies reported before are based on static FC analyses and thus disregard the dynamic rearrangement of RSNs that happens even during resting conditions (Allen et al. 2014).
In chapter 3 we have presented a static FC analysis performed at the whole-brain level to assess resting state functional alterations in brain tumors patients. In this chapter we apply the dynamic FC approach of HMM (Vidaurre, Stephen M. Smith, and Woolrich 2017), using a subset of patients employed in chapter 3 that has been enriched from newly acquired data, to characterize brain states dynamics in patients suffering from high-grade gliomas. The result of the HMM are then compared with the state-of-the-art approach for dynamic FC analyses.

5.2 Materials and Methods

5.2.1 Dataset

Pre-surgical data of 33 patients (14 female, mean age 60.5±12.9y; average FD=0.16mm) suffering from high-grade gliomas were collected at the University Hospital of Padova.
As healthy controls (HC), we used 33 subjects (15 female, mean age 59.6±12.7y; average FD=0.16mm) from the publicly available MPI-Leipzig Mind-Brain-Body dataset (Babayan et al. 2019), described in the previous chapters.

5.2.2 Data acquisition

Since both patients and HC datasets were described previously, we refer the reader to section 3.2.2.

5.2.3 Pre-processing of the data

HCs data were preprocessed following the steps described in section 4.2.3. In particular, a further step consisting of interpolation was applied to the ICs time courses after regression and high-pass filtering. This was required because the TR of the rs-fMRI scans of oncological and healthy subjects was different (TR_{onco}=1.26s, TR_{HC}=1.4s).
For this reason, HCs data were interpolated in the time grid used for the patients and the last 20 volumes of patients acquisition were discarded to obtain the same duration for both the populations. After this step the two rs-fMRI scans resulted in 730 volumes.

5.2.4 Hidden Markov Model

Also for this study, the HMM-MAR toolbox was exploited for the model inference and a multivariate Gaussian distribution adopted for the observational model.
Since the field of view of rs-fMRI scan performed, was restricted for the patients with respect to that of the HC and did not included the cerebellum, the IC representative of the cerebellum was not taken into account in this study.
Prior to the inference, each subject-specific time course was standardized and then temporally concatenated across all participants, yielding a data matrix of dimensions 66 subjects×45 ICs×730 time points. In this way the model inference was performed at the population level.
The initialization with a mixture of Gaussian model was chosen, given that in the previous study no differences were found between the results provided by different model's initialization. Also in this study, 200 realizations of the model were performed.

Choice of the model order

Regarding the choice of the model order, we fit the model with a number of states ranging from 2 to 15. Then for each order we evaluated the FE and the avLL, as indices of goodness of the fit; the AIC and BIC as parsimony indices.
In addition, the uncertainty of the μ_k estimates was also assessed for each model order and for each IC within each state, by computing the CVs, as reported in equation 4.1. For each order K, we finally computed the ratio between the CV's mean standard deviation and CV's average value across states.
After fixing the model order, ΔCV, defined in equation 4.2, was assessed.

Chronnectome

For each subject, the Viterbi path, describing the most likely sequence of visited states, was computed.
Then, we evaluated for each state and population the three metrics defining the "chronnectome", which are the fractional occupancy (FO_HMM), the lifetime (LT) and the switching rate (SR). To compare these three indices among the two populations, we first averaged them within the group, then a two-sample K-S test followed by multiple comparison correction (FDR, α=0.05) was applied for statistical testing of differences between groups.
For the patients, we also tested whether a linear relationship could exist between SR and edema extension, tumor extension, lesion extension.

Brain states graph metrics

From each state's covariance matrix (Σ_k), we firstly derived the Pearson's correlation matrix (Σ_k=Ω_k^-1). On these FC matrices (FC_HMM), graph theory-based metrics were computed. Before evaluating them, a proportional threshold approach (Achard and Bullmore 2007) was applied to the FC matrix of each state. The 20% of the strongest edges were retained ensuring equal density across states. Five graph-based metrics were computed: at the global FC-level the global efficiency (EG) and the the assortativity (ASS), while at the level of single nodes the strength (STR), the local efficiency (EL), the clustering coefficient (CC) and the betweenness centrality (BC). The computation was performed with the BCT (Rubinov and Sporns 2010). A two-sample K-S test followed by multiple comparison correction (FDR, α=0.05) was applied to test for significant differences between states graph metrics.
We also quantified the graph measures at the level of the single RSNs, employing the equation 4.2.8 and extending it to the CC and BC metrics:

$$nCC = \frac{\overline{CC_{k,i}} - \overline{CC_{all,i}}}{std(CC_{all,i})} \qquad k = 1:6, i = 1:10 \tag{5.1}$$

$$nBC = \frac{\overline{BC_{k,i}} - \overline{BC_{all,i}}}{std(BC_{all,i})} \qquad k = 1:6, i = 1:10 \tag{5.2}$$

5.2.5 Sliding windows + clustering

To compare the results obtained through HMM with the gold-standard approach employed in the literature for dynamic connectivity analyses, we performed a SW +clustering analysis (Allen et al. 2014).

Sliding windows

In details, we chose a window size of 73 TR (92 seconds) and a step size of 1 TR. Thus, for each subject we obtained 584 windowed FC. For each windowed FC, only the values in the upper triangular part of the matrix (990) were retained after Z-Fisher transformation. At the population level we thus obtained a matrix of dimensions 66 subjects × 584 windows × 990 correlation values. All subjects

were then concatenated prior to performing the clustering analysis, thus obtaining a matrix of dimensions 38544×990.

K-means clustering

Then, a K-means clustering of windowed FC matrices was performed. We chose the Euclidean distance as distance measure, a number of replicates to repeat the clustering equal to 50 and we tested a number of clusters from 2 to 10.
After obtaining the clusters centroids, the FC matrix of them was created (FC_SW). The Silhouette criterion (Rousseeuw 1987) was employed for the choice of the optimal cluster size.

Clusters centroids chronnectome

After assessing each cluster's FC matrix, the proportion of time spent by each subject in each cluster was computed. We will refer to this quantity as FO_SW. To compare the FO_SW among the two populations, we first averaged the FO_SW within the group, then we applied a two-sample K-S test followed by multiple comparison correction (FDR, α=0.05) for statistical testing of differences between groups.
Starting from the FO_SW, we recreated the subject-specific pseudo-Viterbi path, assigning to each time point the cluster most visited by the subject.

Graph-based analysis applied to clusters FC

We repeated the graph-based analyses described in section 5.2.4, this time applied to the clusters FC matrices. Therefore, we quantified the *EG*, *ASS*, *STR*, *EL*, *CC* and *BC*. Then, we applied a two-sample K-S test followed by multiple comparison correction (FDR, α=0.05) to test for significant differences between clusters graph metrics.

5.2.6 Comparison between HMM and Sliding windows + clustering

To assess whether the two approaches (i.e., HMM and SW+clustering) could give comparable results in terms of connectivity and graph metrics associated to the states or clusters centroids, we matched each HMM state with a cluster centroid on the basis of the associated FC matrix.
In particular, the Pearson correlation and the structural similarity index between the states FC (FC_HMM) and the clusters centroids FC (FC_SW) were computed. Thus, after matching the two, we compared the fractional occupancies (i.e., FO_HMM with FO_SW) as well as the graph measures. For clarity we will

refer to the strength obtained from the HMM analysis as STR_HMM and to that obtained from the SW and clustering analysis as STR_SW, and so on for the other graph metrics.

5.3 Results

5.3.1 Patients characteristics

The demographics and clinical data of the patients are reported in Table 5.1. Figure 5.1 shows the frequency maps of the tumor in the patient population. The distribution is sparse with tumors involving predominantly the right frontal and left temporal lobes, with a low spatial overlaps (maximum value is 24.2% of patients).
No statistically significant differences were found between the patients' and healthy controls' group in head motion during rs-fMRI acquisition: the mean FD was 0.16mm for both the groups.

Age	60.5±12.9y
Gender	
Female	14
Male	19
Tumor histology	
High-grade glioma	6
Glioblastoma	25
n.a.	2
IDH-1/2 mutation status	
Wild type	26
Mutated	3
n.a.	4
Tumor site	
Left	18
Right	11
Bilateral	4

Table 5.1: Demographics and clinical variables collected for the patients. Abbreviations: n.a.=not available, IDH=isocitrate dehydrogenase gene.

5.3.2 Hidden Markov Model

Choice of the model order

The model was fitted for different model orders and, in particular, from 4 to 12 states. Table 5.2 reports the values of the indices evaluated for the choice of

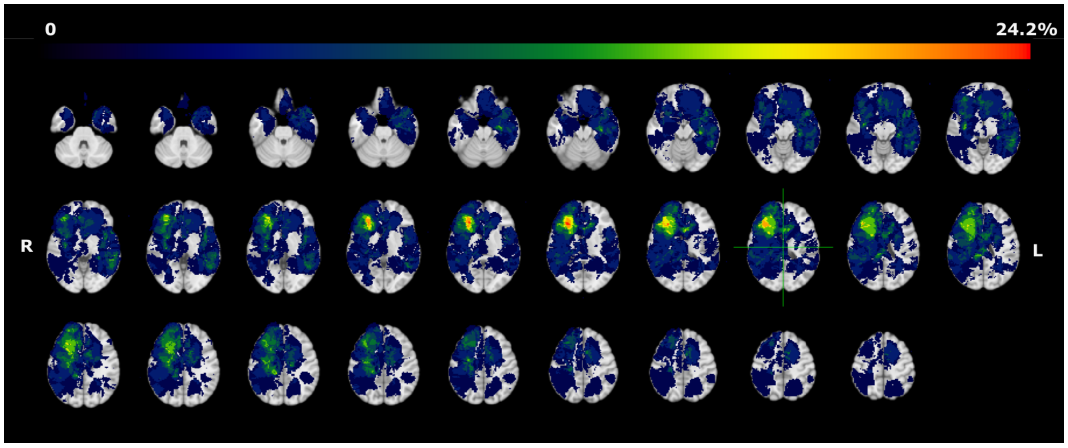

Figure 5.1: Frequency map of tumor core across patients. Maps are over imposed to the MNI atlas (grey scale). Radiological conventions.

the optimal order. While the FE showed a decreasing trend as the number of states increased, the avLL reached the maximum for K=4, followed by K=9,6. Considering only these three orders, the CVs ratio suggested K=6 followed by K=9 as the best.
Furthermore, the CVs obtained within each state, were, on average, lower for K=6 compared to K=9. Therefore, the number of states was set to K=6.

Model order	**FE**	**avLL**	**AIC**	**BIC**	**std/mean**
4	2412830	-16656	435715.6	2202803.5	0.23
5	2404905	-17920	538853.8	2747755.4	0.23
6	2397402	-17452	638531.8	3289264.6	0.23
7	2390761	-18779	741802.7	3834384.4	0.22
8	2384638	-19102	843071.1	4377519.2	0.22
9	2378470	-17115	939723.4	4916055.4	0.23
10	2374248	-18200	1042522.9	5460756.4	0.22
11	2368210	-18440	1143636.2	6003788.7	0.23
12	2363159	-18717	1244829.3	6546918.5	0.22

Table 5.2: The table reports the indices that were evaluated for the choice of the model order. In the first column the lowest free energy value, obtained among the 200 realizations is reported. Starting from this value, we computed the average log-likelihood (second column), Akaike (third column), Bayes Information Criterion (fourth column) and ratio between the std and mean values computed on the averaged CVs within a state (fifth column).

Group-level characteristics

Mean activation (μ_k)

For each brain state (henceforth referred to as S1, S2, S3, S4, S5 and S6) and each IC within the state, Figure 5.2 shows the associated mean activation value. The highest positive values in S1 are associated with the VIS and DAN domains, whereas the negative with the BG. In S2, the DMN and FRN show higher positive deviations from the average, whereas the AUD, CON and DAN higher negative ones. S3 highlights positive values for the SMN and CON, whereas negative values are associated with FRN. In S4, positive values are associated with the AUD and CON. S5 shows positive values associated with SMN, CON and negative values associated with DMN. S6 highlights positive values for the DMN, CER and for most ICs of the VIS and DMN. Negative mean values are associated with the VIS, AUD, CON.

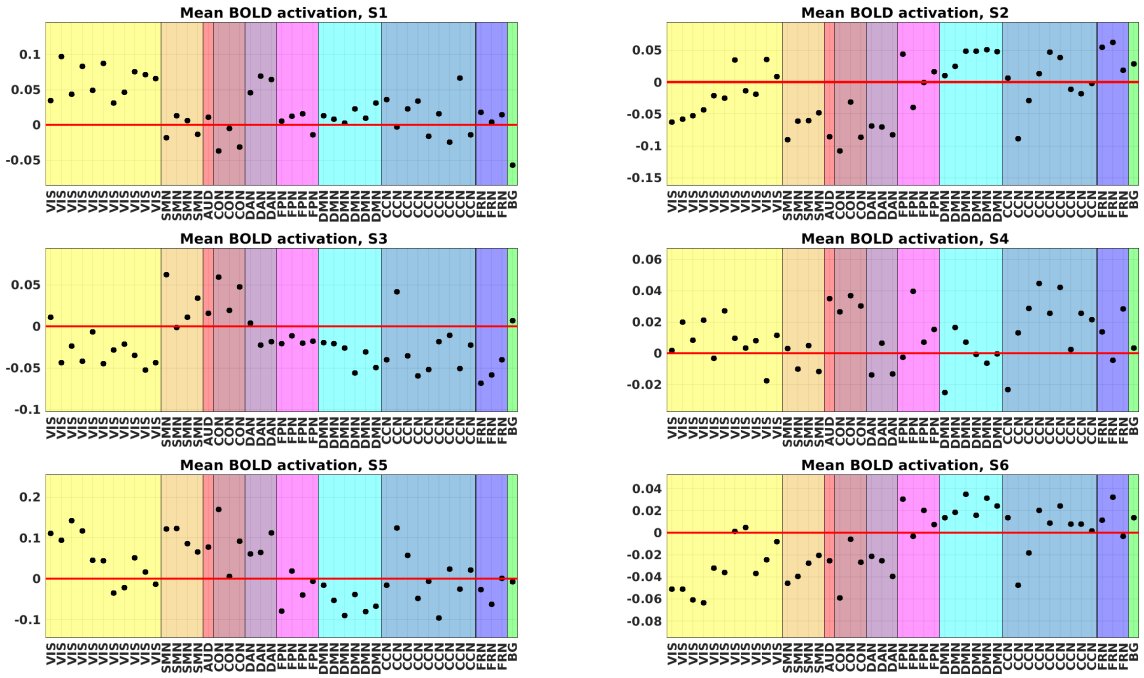

Figure 5.2: Each figure shows, for each brain state and each IC, the associated mean activation value, depicted by black dots. The red line, set at 0, separates positive and negative μ_k values.

Reliability of the states

The precision of the μ_k estimates was assessed through the computation of the CVs. In Figure 5.3, the CVs associated to each IC and within each state, are reported.

Ranking the most reliable states in terms of CVs, resulted in S2 ($\overline{CV} = 45.7\%$), S4 ($\overline{CV} = 52.4\%$), S1 ($\overline{CV} = 53.3\%$), S3 ($\overline{CV} = 58.6\%$), S6 ($\overline{CV} = 64.4\%$) and finally S5 ($\overline{CV} = 84.4\%$).

Overall, when comparing the reliability across states and within functional domains, the μ_k values associated with the DAN show the highest reliability, whereas those associated with FRN and BG are the least reliable in all the states with CVs above the average level.

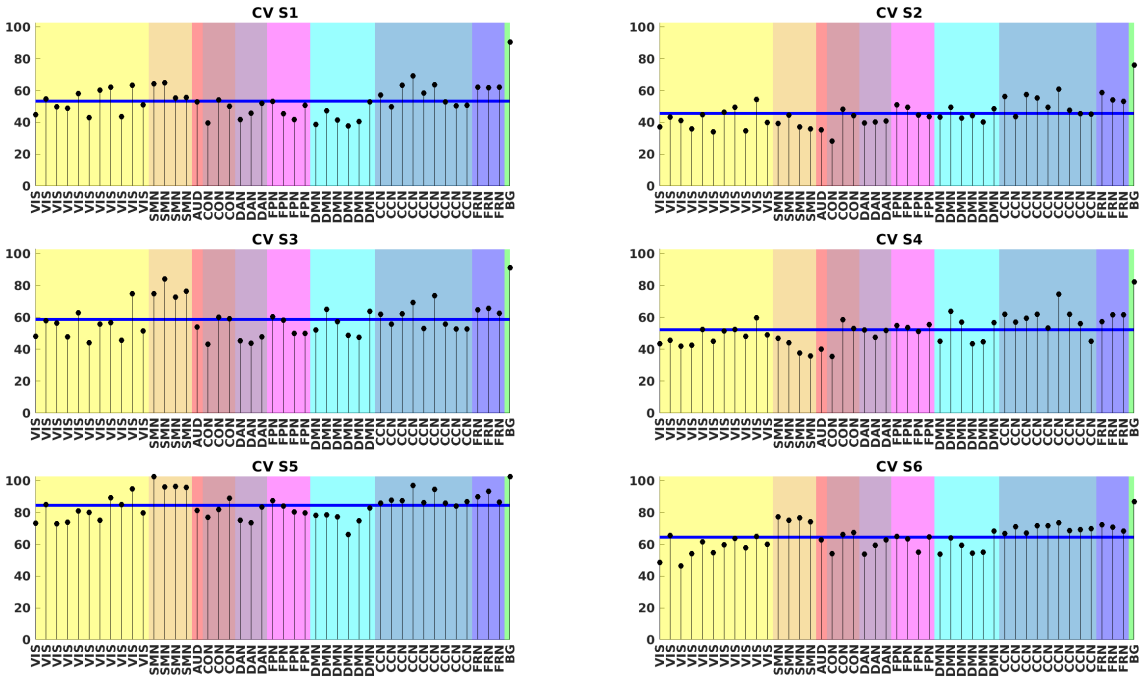

Figure 5.3: Each figure shows, for each brain state and each IC, the associated CVs, depicted by black stems. The blue line represents the average CV ($\overline{CV}$) within the state.

Chronnectome

In Figure 5.4 the fractional occupancy (FO_HMM) distribution, obtained for the two groups, is shown in each brain state. The average time spent from the patients in state 5 was 30% of the total rs-acquisition and 62% in state 6. While HCs spent 25% of the time in S1, 25% in S2, 29% in S3 and 13% in S4.

The K-S test pointed out statistically significant differences between groups in all the states.

Figure 5.5 reports the most likely sequences of states, (i.e., the Viterbi paths) for the two groups of subjects, and the transition probabilities among states.
Regarding SR, we did not find statically significant differences between patients and HCs. The median value of SR of patiens was 0.078Hz, whereas for HCs 0.083Hz. We also tested whether a linear relationship could exist between patient's SR and tumor features, but for all the features tested we did not find statically significant relationships.

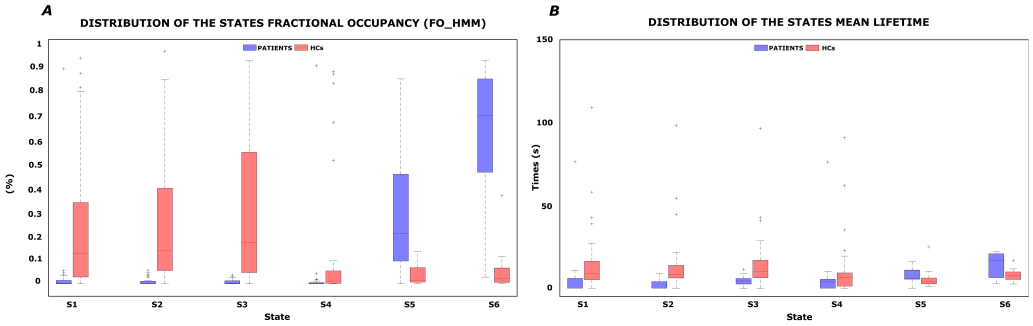

Figure 5.4: In Panels (A) and (B), the distribution in different states of fractional occupancy and mean LT, respectively, is reported in blue for the patients and in red for the HCs. The bottom and top edges of each box indicate the 25^{th} and 75^{th} percentiles. The outliers are represented by the "+" symbol. In each boxplot, the solid line indicates the median.

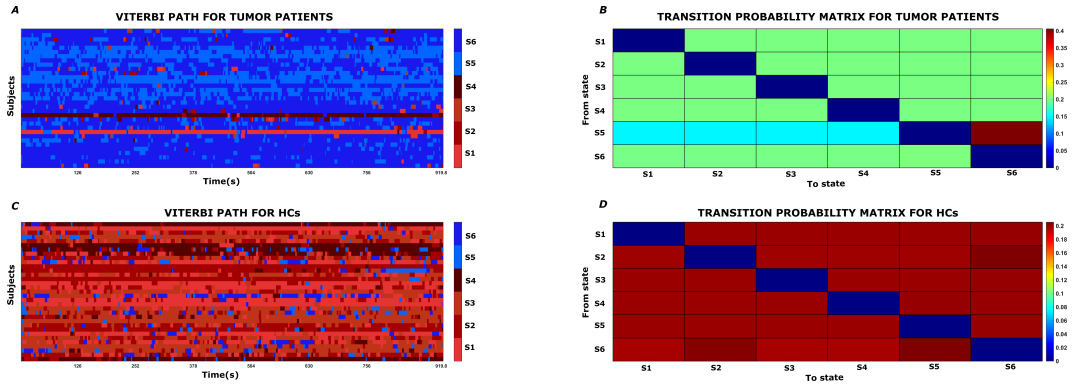

Figure 5.5: In panels (A) and (C), we report for patients and HCs respectively, the Viterbi path computed for each subject, in the y-axis, and for each time point, in the x-axis. Different colors are assigned to distinct states. In panels (B) and (D) the transition probabilities from one state (y-axis) to another (x-axis), for the patients and HCs, are reported.

Brain states graph metrics

Figure 5.6 shows the FC maps representative of each brain state. After proportional thresholding, we computed the six graph metrics.
Since the FC matrices were obtained at the group-level, without distinction between the two groups of patients and controls, the graph indices are representative of the whole population. The distribution of the *STR*, *EL*, *CC*, *BC* is displayed in Figure 5.7. The values obtained for the EG and ASS are reported in Table 5.3.
Statistically significant differences were found in the *STR*, *EL* and *CC* between S5, S6 and all the other states. For the *BC*, instead, no statistically significant differences were found between states.
In Figure 5.8 we report the results of the analysis carried out at the functional domain level, for the *STR*, *EL*, *CC* and *BC* measures. Taking into account only the extreme values exceeding ± 1.5std, we found that in S1 the *STR* of DMN was significantly higher than in the remaining domains; in S4 the same happened for the SMN domain.
Considering the *EL*, we found only negative deviations and in particular for S5 in VIS, AUD and DMN.
Also for the *CC* we found the same negative deviations for S5 in VIS, AUD and DMN.
Finally, for the *BC* we observed positive deviations for S4 in FRN, for S5 in DMN and for S6 in VIS and SMN, while negative deviations for S6 in AUD.

	EG	**ASS**
S1	0.21	0.05
S2	0.23	0.24
S3	0.22	0.16
S4	0.22	0.39
S5	0.15	0.12
S6	0.16	0.08

Table 5.3: Values of the global efficiency (*EG*) and assortativity (*ASS*) for the six brain states.

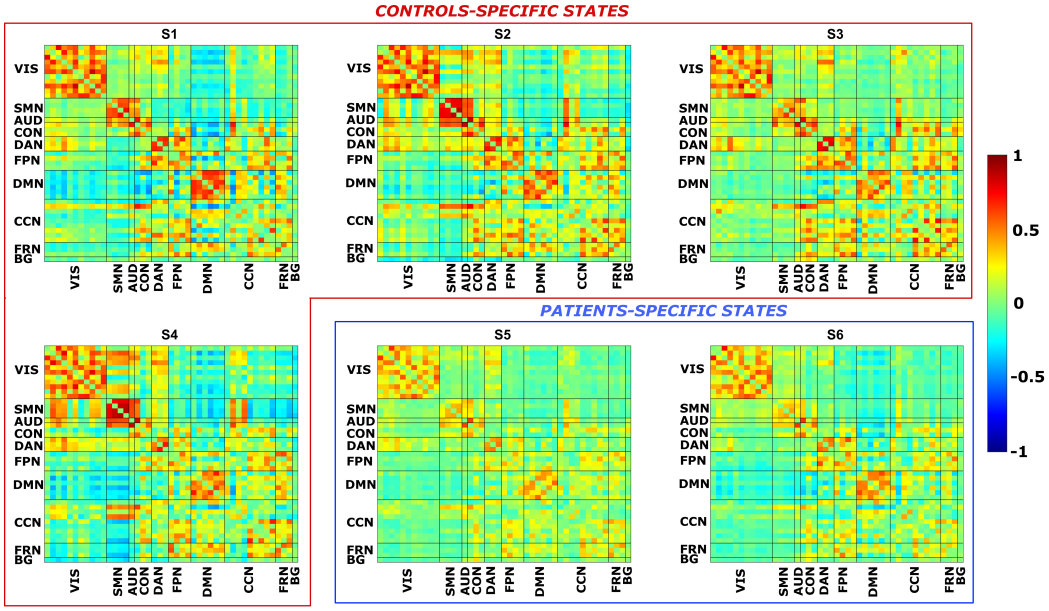

Figure 5.6: Each panel represents the FC matrix associated to a particular brain state (S1, S2, etc.). In both the x- and y-axis, we have the 45 ICs, divided in the 10 functional domains. Warm colors represent high positive correlations values between ICs, whereas cool colors represent high anti-correlations values. We grouped together states mostly populated by HCs (red box) and by patients (blue box).

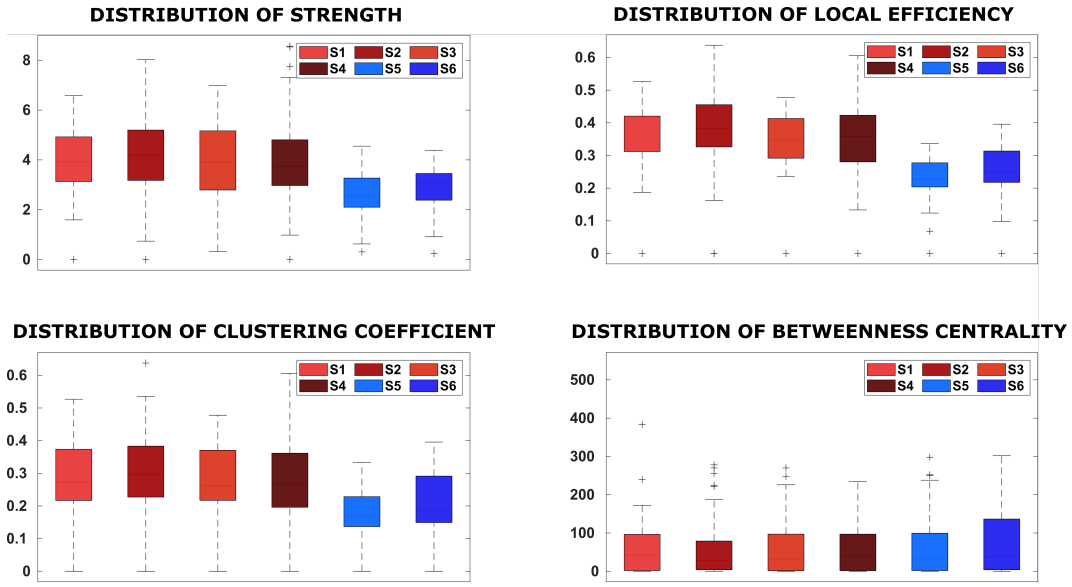

Figure 5.7: In each panel, the distribution in different states of each graph measure is reported.

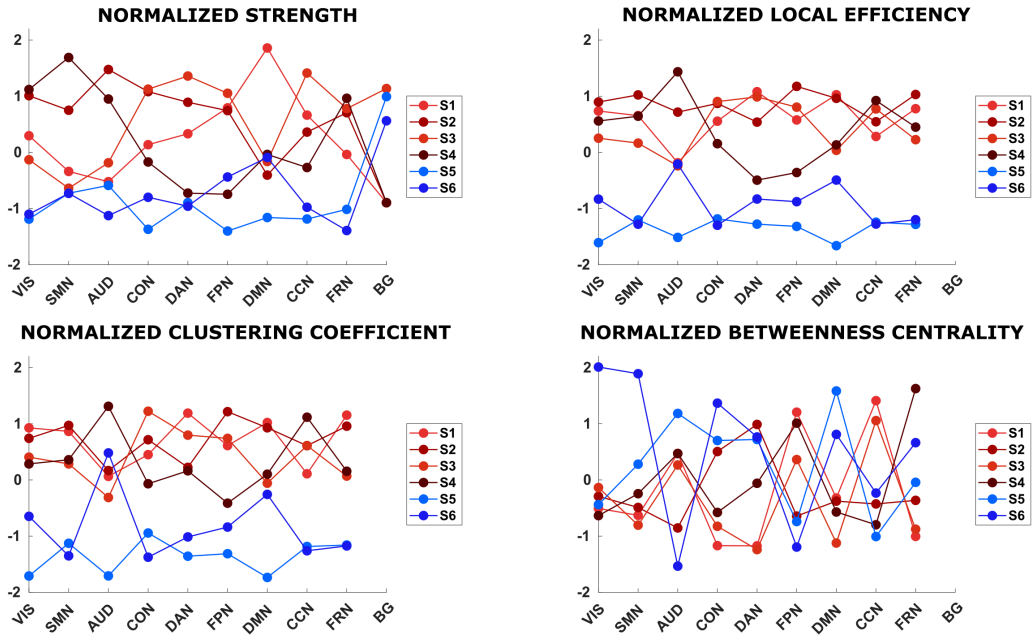

Figure 5.8: In each panel, the normalized values of graph metrics are reported for each state, colored differently, and for each RSNs.

5.3.3 Sliding windows + clustering

Choice of the cluster size

As shown in Figure 5.9, the Silhouette criterion suggested the optimal cluster size equal to 6. Thus we characterized the 6 clusters centroids FC matrices and we derived from them the same graph measures as done for HMM.

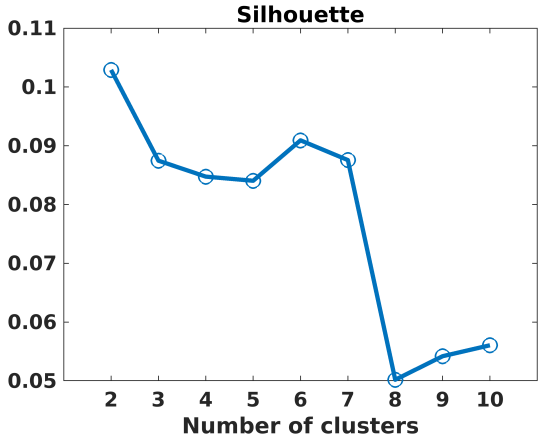

Figure 5.9: The figure reports the Silhouette's values obtained by varying the clusters size.

Clusters centroids graph metrics

In Figure 5.10 FC_SW maps of the clusters centroids are reported.
The distribution of the *STR*, *EL*, *CC*, *BC* is displayed in Figure 5.11. The values obtained for the *EG* and *ASS* are reported in Table 5.4.
Statistically significant differences were found in the *STR*, *EL* and *CC* between CL5 and all the others. Moreover we found differences in:

- *STR* in CL1 vs CL2; in CL2 vs CL1, CL4, CL6; in CL4 vs CL2; in CL6 vs CL2.
- *EL* in CL1 vs CL2, CL3; CL2 vs all the others; CL3 vs CL1, CL5; in CL4 vs CL2; in CL6 vs CL2.
- *CC* in CL1 vs CL2; in CL2 vs CL1, CL3,CL4; in CL3 vs CL2; in CL4 vs CL2.

For the *BC*, instead, no statistically significant differences were found between states.
In Figure 5.12 we report the results of the analysis carried out at the functional domain level. Considering only the the extreme values exceeding ±1.5std, we found that in CL2 the *STR* of AUD, CON, CCN was significantly higher than in the remaining domains; in CL3 higher in the FRN and in CL5 the same happened for the BG.
Considering the *EL*, we found positive deviations for CL2 in CON, DAN, CCN and FRN; negative deviations for CL5 in AUD, CON, FPN and DMN.
Regarding the *CC* we found positive deviations for CL2 in DAN, CCN, FRN and negative deviations for CL5 in AUD, CON, FPN, DMN.
Finally, for the *BC* we observed positive deviations for CL1 in SMN, for CL5 in CON and for CL6 in CCN, while negative deviations for CL2 in DAN, for CL4 in FRN.

	EG	**ASS**
CL1	0.21	0.47
CL2	0.33	0.27
CL3	0.24	0.25
CL4	0.20	0.07
CL5	0.15	0.06
CL6	0.22	0.31

Table 5.4: Values of the global efficiency (*EG*) and assortativity (*ASS*) for the six clusters.

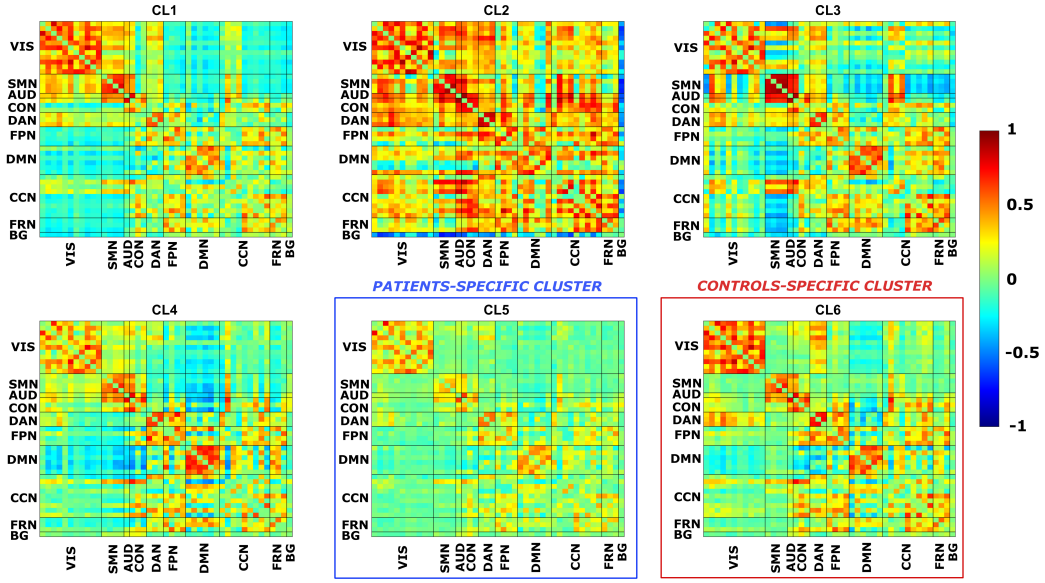

Figure 5.10: Each panel represents the FC matrix associated to a particular cluster (CL1, CL2, etc.). In both the x- and y-axis, we have the 45 ICs, divided in the 10 functional domains. Warm colors represent high positive correlations values between ICs, whereas cool colors represent high anti-correlations values. We grouped together clusters centroids mostly populated by HCs (red box) and by patients (blue box).

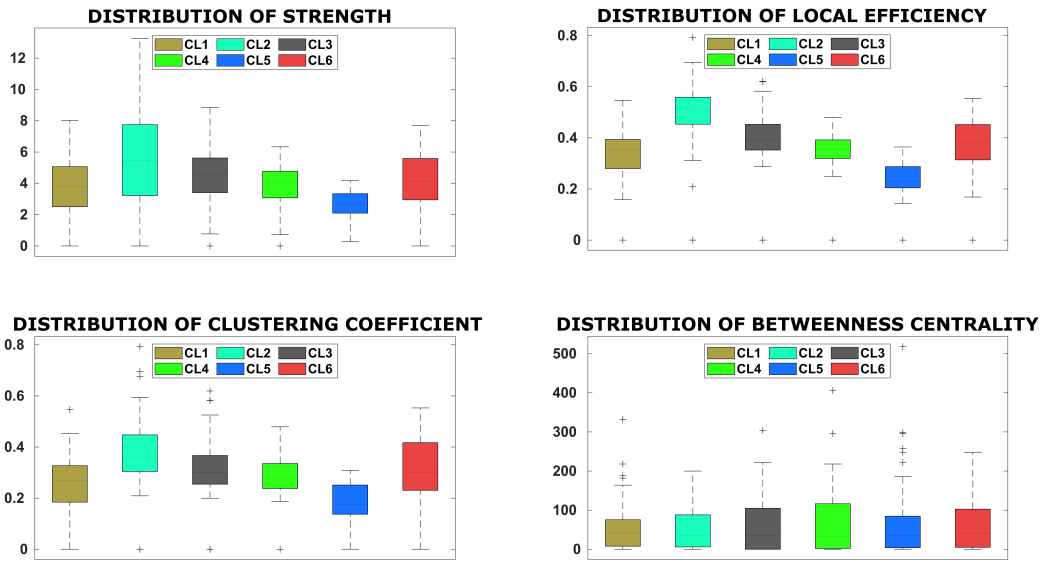

Figure 5.11: Each panel shows the distribution of each graph measure, within a specific cluster.

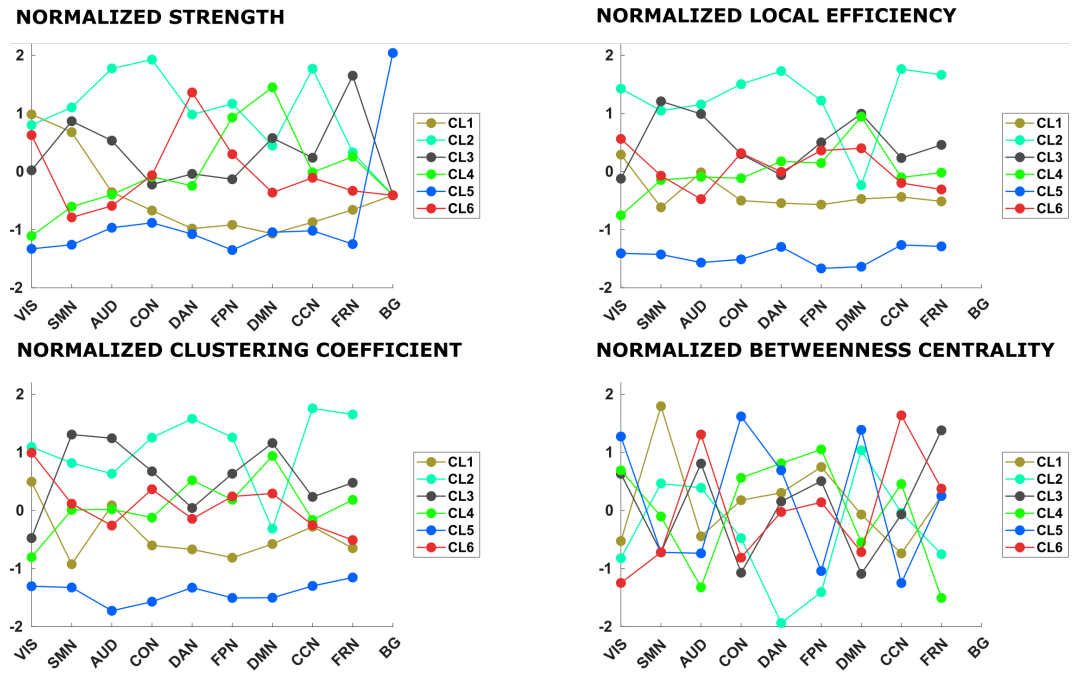

Figure 5.12: In each panel, the normalized values of graph metrics are reported for each cluster, colored differently, and for each RSNs.

Clusters centroids chronnectome

In Figure 5.13 the fractional occupancy (FO_SW) distribution, obtained for the two groups, within each cluster is shown. The average time spent from the patients in CL5 was 64.6% of the total rs-acquisition, 17.4% in CL1, 14.1% in CL4 and 3.9% in CL6. While HCs spent 39.8% of the time in CL6, 15.5% in CL4, 14.9% in CL3, 14.8% in CL1, 12.1% in CL5 and 2.9% in CL2.
The K-S test pointed out statistically significant differences between groups in CL5 and CL6. In fact, CL5 was mostly populated by patients, while CL6 by controls.
This can be well appreciated by the pseudo-Viterbi paths, reported in Figure 5.14.

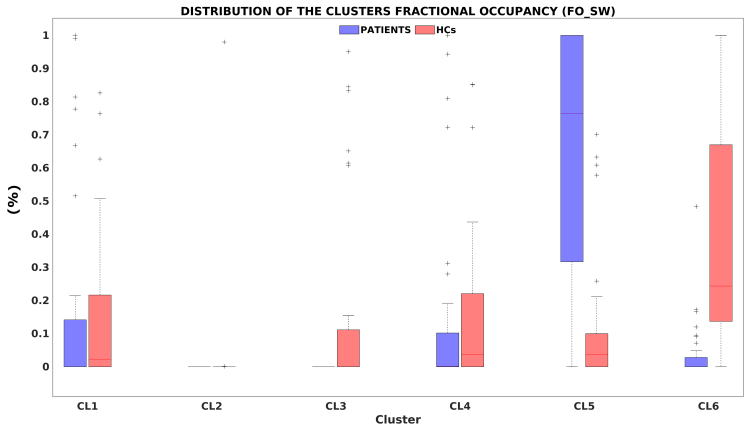

Figure 5.13: The figure reports the distribution in different clusters of fractional occupancy, in blue for patients and in red for HCs. The bottom and top edges of each box indicate the 25^{th} and 75^{th} percentiles. The outliers are represented by the "+" symbol. In each boxplot, the solid line indicates the median.

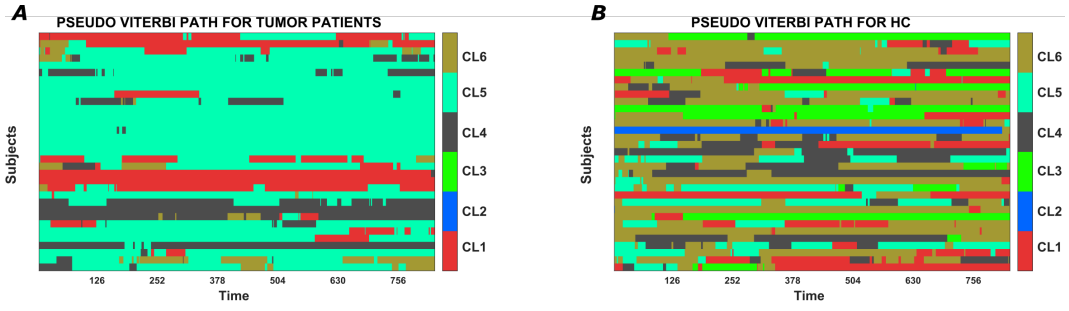

Figure 5.14: In panels (A) and (B) we report for patients and HCs, respectively, the pseudo-Viterbi path computed for each subject in the y-axis, and for each time point, in the x-axis. Different colors are assigned to distinct clusters.

5.3.4 Comparison between HMM and Sliding windows + clustering

In Table 5.5 and Table 5.6, the Pearson correlation and the structural similarity indices computed between the FC_HMM and the FC_SW are, respectively, reported. Taken together, these results led us to clearly associate CL2 to S2, CL3 to S2, CL5 to S5 and CL6 to S3. Instead, CL1 could be weakly associated to S4 and CL4 to S1.

Corr	S1	S2	S3	S4	S5	S6
CL1	0.58	0.58	0.59	0.59	0.61	**0.62**
CL2	0.55	**0.66**	0.62	0.60	0.60	0.58
CL3	0.54	**0.61**	0.58	**0.61**	**0.61**	0.60
CL4	0.49	0.48	**0.54**	0.44	0.52	0.53
CL5	0.63	0.61	0.67	0.57	**0.72**	0.68
CL6	0.71	0.68	**0.74**	0.65	0.73	0.70

Table 5.5: The table reports the correlation values between each FC_HMM map and each FC_SW map. The highest values for each comparison are highlighted in bold.

Ssim	S1	S2	S3	S4	S5	S6
CL1	0.36	0.43	0.37	**0.45**	0.33	0.34
CL2	0.15	**0.30**	0.25	0.17	0.13	0.08
CL3	0.29	**0.53**	0.28	0.44	0.24	0.20
CL4	**0.47**	0.39	0.36	0.32	0.25	0.38
CL5	0.30	0.29	0.36	0.24	**0.41**	0.38
CL6	0.44	0.40	**0.52**	0.28	0.25	0.26

Table 5.6: The table reports the structural similarity indices computed between each FC_HMM map and each FC_SW map. The highest values for each comparison are highlighted in bold.

5.4 Discussion

In the present study, we explored the impact of brain tumors on the dynamics of the BOLD signal acquired in resting conditions. First, we applied a HMM to the time courses of the 45 ICs obtained at the whole-brain level and then we characterized 6 dynamic brain states in terms of group-level features (mean BOLD activation, CVs, FC maps, graph metrics) and individual-level features (FO in each state, SR, Viterbi paths).
To compare the results obtained through HMM, with the most used approach in

literature for dynamic FC analyses, we conducted a SW+clustering analysis. In particular, after selecting the best cluster size (i.e., 6 clusters), we characterized clusters in terms of the same features computed for the HMM analysis.
Through the comparison of the results of the two approaches, we were able to understand which method, between HMM and SW, was the best to discriminate the two populations in terms of BOLD signal dynamics.

5.4.1 Hidden Markov Model

From Figure 5.2 we were able to distinguish high activation states (S1, S5) from baseline states (S4, S6) in which the RSNs present a mean level of activation.
Regarding the uncertainty of the estimates, quantified through the CVs, we were able to distinguish networks across states that were associated with higher uncertainty, such as FRN and BG. As explained before, this result is not unexpected, since the BOLD signal in the basal ganglia has a quite different underpinning structure in comparison with cortical regions, both in terms of neuroreceptors (Palomero-Gallagher and Zilles 2018) and iron content (Cherubini et al. 2009).
After comparing the occupancy in each state between patients and HCs, we could observe that two states, namely S5 and S6, were mostly occupied by patients, while the other four states, namely S1, S2, S3, S4 by HCs. Interestingly, the occupancy of patients in HCs-specific states, was almost zero. Taken together, these results highlight the ability of HMM to discriminate between the two groups of subjects and thus to separate the BOLD signal dynamics of different clinical populations.
When observing the FC patterns of patients-specific states (Figure 5.6), one could immediately note the overall decrease in FC in patients-specific states with respect to HCs-specific states.
The graph-based analysis carried out on the FC matrices, pointed out very interesting results, both considering the entire state or specific networks. The statistically significant decrease in *STR*, *EL* and *CC* in patients-specific states depicted a system where RSNs are less integrated and segregated. In addition, the lower *ASS* values associated to patients compared to HCs also indicated greater nodes resilience. The decrease in *EG* in S5 and S6 suggested a reduction in the overall capacity of the brain in transferring and integrating information among distributed nodes. The *BC* did not change between patients and HCs states, suggesting instead that nodes did not lose their centrality.
Moving to the analysis performed at the single network level, we could observe that S5, mostly occupied by patients, presented a VIS, AUD and DMN with both *EL* and *CC* under the threshold (-1.5std). Moreover, this state showed a decrease in *STR* for the DMN, even if it was not below the threshold. Interestingly, in the literature the DMN was one of the most commonly studied networks in brain

tumors patients with some of the most consistent findings results of decreases in overall FC. In line with our results, previous studies using ICA found a decrease in FC strength across DMN regions in brain tumors patients compared to HCs (R. Esposito et al. 2012; Ghumman et al. 2016; Maesawa et al. 2015).

5.4.2 Sliding windows + clustering

From the SW followed by clustering analysis we could describe six main clusters in which subjects tended to persist. Among the FC maps associated to clusters centroids, that of CL2 seemed not to truly represent a standard FC pattern, but rather an iper-connectivity system, thus suggesting that CL2 could be a cluster where all the noise ends up.
After computing the FO_SW and testing for statistically significant differences between groups, we could recognize only one patients-specific cluster (i.e., CL5) and one HCs-specific cluster (i.e., CL6).
When comparing the FC maps resulting from the HMM- and SW- analyses, we observed that both in terms of correlation and structural similarity, the map of CL5 was the one that best matched that of the two patients-specific states, i.e., S5 and S6. Thus, while through the HMM analysis we were able to find two brain states associated to patients, through the SW analysis we could only find one patients-specific cluster, which probably encapsulated the connectivity features of both S5 and S6. Thus, in contrast to HMM-based analysis, this approach was less sensitive in separating patients from controls. This can be also appreciated from Figure 5.14, where the Viterbi paths between the two groups of subjects are more similar with respect of those presented in Figure 5.5.
At the graph-level, the *STR*, *EL* and *CC* of CL5 were statistically lower than those associated to the other clusters. Moving to specific RSNs, in agreement with the results obtained through HMM, the *EL* and *CC* of the AUD and DMN resulted to be lower than -1.5std. Moreover, the *EG* and *ASS* of CL5 were the lowest among all.

5.5 Conclusions

In this study we applied the data-driven approach of Hidden Markov Model, to characterize differences in brain states functional dynamics between patients suffering from high-grade glioma and healthy controls. The analysis was performed at the whole-brain level, using the time courses of 45 ICs.
Firstly we performed the model selection, then we fit the model and finally we characterized the mean BOLD activation, its accuracy and the functional connectivity of six brain states. Furthermore, by computing the fraction of time spent

by each subject in each state, we could define patients-specific states (S5, S6) rather than controls-specific states (S1, S2, S3, S4). This result suggested that patients persisted in a few dynamic states and that HMM is a sensitive dynamic approach able to separate patients from controls.
By means of a graph-based analysis applied on the FC maps, we found that patients-specific states featured an overall lower FC and less efficient exchange of information between networks. In terms of integration and segregation, the DMN resulted to be one of the most altered networks.
The HMM results were, in part, confirmed by a standard SW+clustering analysis. Indeed, with this last approach we characterized six clusters, but only one of them was mainly associated to patients. In support of the previous results, however, this cluster was the only one to show significant decreases in functional connectivity.
In conclusion, we have proven evidence that even in brain tumor patients, resting-state functional dynamics exist and the connectivity patterns of brain states visited by patients are very different from those of healthy controls. A standard sliding windows approach is not enough to capture the granular features of dynamic brain states.

Chapter 6

Conclusions

In the last decades, the neuroscience community has paid growing attention to the study of functional brain connectivity to investigate statistical relationships between the activity of even spatially distant regions in the brain. Among the techniques that can be employed to investigate such relationship, rs-fMRI has been the most used, due to its reduced invasiveness and ease of applicability. In fact, this technique does not require the cooperation of the patient in performing specific tasks, thus it can be easily applied in the clinical practice.
Many approaches have been introduced to study functional connectivity and these can be roughly divided into static and dynamic approaches. Static approaches consist in assessing the connectivity among regions after averaging the fMRI BOLD signal over the entire acquisition scan, while dynamic approaches aim to assess the sequence of FC patterns (i.e., the brain states) that occur throughout the acquisition scan.
Dynamic approaches are increasingly used in research, when fMRI sequences are long enough to support such analysis, since they allow to understand how and how fast, different brain areas talk to each other and how much the neural dynamics slow down or up in a healthy or diseased brain. The possibility of extrapolating such important information has become possible thanks to the introduction in literature of the approach based on sliding windows followed by a clustering analysis. Indeed, it allows the identification of recurring FC patterns of correlation or anti-correlation between brain regions in specific time windows. Besides its simplicity, this technique carries some limitations, and among them, the choice of the window length has long been matter of debate. To date, there are no quantitative approaches to choose such length.
Recently, HMM has been introduced in this dynamic context. Defined in a probabilistic framework, it allows the quantitative choice of the number of brain states by monitoring the free energy cost function. After the model inference, a variety of features could be extrapolated to describe brain states, for example the mean

BOLD activation within the state, the FC patterns between regions in a state or, again, the probability of observing a state in a specific time instant of the acquisition.
With the aim of providing even more detailed information of dynamic brain states, in this work of thesis we developed a whole-brain data-driven framework based on HMMs, to describe at high spatial resolution how RSNs communicate.
To gain such high spatial resolution functional parcellation of RSNs we performed a group-level spatial ICA, presented in the first study of this dissertation (chapter 3). In the same chapter this parcellation was exploited to assess functional alterations caused by brain tumors in a cohort of 24 patients acquired at the University Hospital of Padova. To this end, we developed a novel method able to capture subject-specific changes in brain network topography and strength. The implemented analyses have allowed us to describe widespread alterations occurring far from the lesion or the edema, with cortical areas near the lesion that were potentially preserved.
After this study, we moved to the core of our research, so we employed HMMs to study healthy aging. We applied the developed functional parcellation to rs-fMRI data of healthy subjects, equally divided in young and old, to extrapolate the ICs time courses that served as input of the model. We fitted the HMM with different number of states and we performed model selection in a quantitative way, by balancing the goodness of the fit with the precision of the parameters estimates, evaluated through a novel index. To our knowledge, this is the first study that assess the uncertainty of the estimates. After performing the model order selection, six states were characterized at the population level in terms of FC patterns, mean BOLD activity, estimates accuracy and graph metrics and at the single-subject level in terms of time spent in each state and transitions between states.
The results were very promising, indeed, among the six inferred states we found a clear separation between the two groups of subjects in terms of fractional occupancy. This allowed us to define young-specific states rather than old-specific states.
The graph-based analysis applied on the six FC maps revealed a decrease in strength with the increase of age in the DMN and FPN, and an overall more integrated topology of states occupied by old subjects, in particular between the DAN and other RSNs. Moreover, the transitions between states were not random and followed preferential paths.
These findings suggested that HMM is very reliable approach to capture the complex brain's functional dynamics that occur with aging and can give a rich depiction of time-varying FC.
Once the analyses framework was optimized, it was applied to a cohort of patients

suffering from high grade gliomas, to investigate how and if the disease impacts brain's dynamics. Since this was the first study in the literature to present a dynamic connectivity analysis on this clinical population, we also performed a standard sliding window-based connectivity analysis. The results obtained were very exciting: by computing the fraction of time spent by each subject in each state, we found that among the six inferred states, two could be defined as patients-specific states, while the other four as controls-specific states. Moreover, in line with previous studies based on static FC analyses, we found that patients-specific states featured an overall lower FC, a less efficient exchange of information between networks and, in terms of integration and segregation, the DMN resulted to be one of the most altered networks.
The results obtained through the sliding windows analysis partially confirmed the HMM results. In particular, the optimal number of clusters resulted to be six even if, however, only one of them was mainly associated to patients. In support of the previous results, this cluster was the only one to show significant decreases in FC. These findings underlie the better capacity of the mathematically more robust approach of HMM to separate patients from controls.
With this thesis we have shown that the proposed framework was suitable to study the dynamic connectivity trajectories in healthy aging and in patients with brain tumors. Ongoing analyses in patients suffering from high grade glioma will lead to integrate functional, structural, and behavioral information in order to better characterize the underlying pathology.

Chapter 7

Appendix: other activities

In this section we briefly present two side projects that were carried out during the PhD program.

7.1 Structural disconnections in gliomas: atlas- VS tractography-based methodologies

In this study we investigated the impact of direct and indirect approaches in quantifying WM structural disconnections in a cohort of 50 high- and low-grade glioma patients. Gliomas are amongst the most common primary brain tumors in adults and are often associated with poor prognosis. Understanding the extent of WM which is affected outside the tumoral lesion may be of paramount importance to explain cognitive deficits and the clinical progression of the disease.
To this end, we explored both direct (i.e., tractography based) and indirect (i.e., atlas based) approaches to quantifying WM structural disconnections in our cohort of patients. While these methodologies have recently gained popularity in the context of stroke, to our knowledge this was the first time they are applied in patients with brain tumors.
More specifically, we performed a quantitative comparison of the disconnection maps provided by the two methodologies by applying well known metrics of spatial similarity, extension and correlation. Given the important role the edematous tissue plays in the physiopathology of tumors, we performed these analyses both by including and excluding it in the definition of the tumoral lesion. This was done to investigate possible differences determined by this choice.
We found that direct and indirect approaches offer two distinct pictures of structural disconnections in patients affected by brain gliomas, presenting key differences in several regions of the brain.

7.2 Tractography-based reconstruction of the FN in Vestibular Schwannoma

In this study we applied diffusion MRI tractography to preoperative facial nerve reconstruction in patients affected by vestibular schwannoma. Although tractography of the facial nerve based on single-shell diffusion MR imaging is thought to be helpful before surgery for resection of vestibular schwannoma, this paradigm can be vitiated by the isotropic diffusion of the CSF, the convoluted path of the facial nerve, and its crossing with other bundles. In this study we proposed a multi-shell diffusion MR imaging acquisition scheme combined with probabilistic tractography that has the potential to provide a presurgical facial nerve reconstruction uncontaminated by such effects.
Five patients scheduled for vestibular schwannoma resection underwent multi-shell diffusion MR imaging (bvalues= 0, 300, 1000, 2000 s/mm^2). Facial nerve tractography was performed with a probabilistic algorithm and anatomic seeds located in the brain stem, cerebellopontine cistern, and internal auditory canal. A single-shell diffusion MR imaging (b-value=0, 1000 s/mm^2) subset was extrapolated from the multi-shell diffusion MR imaging data. The quality of the facial nerve reconstruction based on both multi-shell diffusion MR imaging and single-shell diffusion MR imaging sequences was assessed against intraoperative videos recorded during the operation.
Single-shell diffusion MR imaging–based tractography was characterized by failures in facial nerve tracking (2/5 cases) and inaccurate facial nerve reconstructions displaying false-positives and partial volume effects. In contrast, multi-shell diffusion MR imaging–based tractography provided accurate facial nerve reconstructions (4/5 cases), even in the presence of ostensibly complex patterns.
In comparison with single-shell diffusion MR imaging, the combination of multi-shell diffusion MR imaging–based tractography and probabilistic algorithms proved to be a more valuable aid for surgeons before vestibular schwannoma resection, providing more accurate facial nerve reconstructions, which may ultimately improve the postsurgical patient's outcome.

Bibliography

Achard, Sophie and Ed Bullmore (Feb. 2, 2007). "Efficiency and Cost of Economical Brain Functional Networks". In: *PLoS Computational Biology* 3.2. Ed. by Karl J Friston, e17. ISSN: 1553-7358. DOI: 10.1371/journal.pcbi.0030017.

Adhikari, Mohit H. et al. (Apr. 1, 2017). "Decreased integration and information capacity in stroke measured by whole brain models of resting state activity". In: *Brain* 140.4, pp. 1068–1085. ISSN: 0006-8950, 1460-2156. DOI: 10.1093/brain/awx021.

Agosta, Federica et al. (Aug. 2012). "Resting state fMRI in Alzheimer's disease: beyond the default mode network". In: *Neurobiology of Aging* 33.8, pp. 1564–1578. ISSN: 01974580. DOI: 10.1016/j.neurobiolaging.2011.06.007.

Akaike, Hero (1973). "Information theory and an extension of the maximum likelihood principle". In: *2nd Internetional Symposium on Information Theory*. Akadémiai Kiadó, pp. 267–281.

Allen, Elena A et al. (2014). "Tracking Whole-Brain Connectivity Dynamics in the Resting State". In: p. 14.

Andersen, Sarah M., Steven Z. Rapcsak, and Pélagie M. Beeson (Oct. 2010). "Cost function masking during normalization of brains with focal lesions: Still a necessity?" In: *NeuroImage* 53.1, pp. 78–84. ISSN: 10538119. DOI: 10.1016/j.neuroimage.2010.06.003.

Andersson, Jesper L R, Stefan Skare, and John Ashburner (2003). "How to correct susceptibility distortions in spin-echo echo-planar images: application to diffusion tensor imaging". In: p. 19.

Andrews-Hanna, Jessica R. et al. (Dec. 2007). "Disruption of Large-Scale Brain Systems in Advanced Aging". In: *Neuron* 56.5, pp. 924–935. ISSN: 08966273. DOI: 10.1016/j.neuron.2007.10.038.

Ashburner, John and Karl J. Friston (July 2005). "Unified segmentation". In: *NeuroImage* 26.3, pp. 839–851. ISSN: 10538119. DOI: 10.1016/j.neuroimage.2005.02.018.

Avants, Brian B. et al. (Feb. 2011). "A reproducible evaluation of ANTs similarity metric performance in brain image registration". In: *NeuroImage* 54.3, pp. 2033–2044. ISSN: 10538119. DOI: 10.1016/j.neuroimage.2010.09.025.

Babayan, Anahit et al. (Mar. 2019). "A mind-brain-body dataset of MRI, EEG, cognition, emotion, and peripheral physiology in young and old adults". In: *Scientific Data* 6.1, p. 180308. ISSN: 2052-4463. DOI: 10.1038/sdata.2018.308.

Bagarinao, Epifanio et al. (Dec. 2019). "Reorganization of brain networks and its association with general cognitive performance over the adult lifespan". In: *Scientific Reports* 9.1, p. 11352. ISSN: 2045-2322. DOI: 10.1038/s41598-019-47922-x.

Banich, Marie T. et al. (Nov. 1, 2000). "fMRI Studies of Stroop Tasks Reveal Unique Roles of Anterior and Posterior Brain Systems in Attentional Selection". In: *Journal of Cognitive Neuroscience* 12.6, pp. 988–1000. ISSN: 0898-929X, 1530-8898. DOI: 10.1162/08989290051137521.

Barttfeld, Pablo et al. (Jan. 20, 2015). "Signature of consciousness in the dynamics of resting-state brain activity". In: *Proceedings of the National Academy of Sciences* 112.3, pp. 887–892. ISSN: 0027-8424, 1091-6490. DOI: 10.1073/pnas.1418031112.

Bassett, Danielle S. et al. (Feb. 2012). "Altered resting state complexity in schizophrenia". In: *NeuroImage* 59.3, pp. 2196–2207. ISSN: 10538119. DOI: 10.1016/j.neuroimage.2011.10.002.

Beckmann, Christian F et al. (May 29, 2005). "Investigations into resting-state connectivity using independent component analysis". In: *Philosophical Transactions of the Royal Society B: Biological Sciences* 360.1457, pp. 1001–1013. ISSN: 0962-8436, 1471-2970. DOI: 10.1098/rstb.2005.1634.

Betzel, Richard F. et al. (Nov. 2014). "Changes in structural and functional connectivity among resting-state networks across the human lifespan". In: *NeuroImage* 102, pp. 345–357. ISSN: 10538119. DOI: 10.1016/j.neuroimage.2014.07.067.

Bishop, Christopher M. (2006). *Pattern recognition and machine learning*. Information science and statistics. New York: Springer. 738 pp. ISBN: 978-0-387-31073-2.

Biswal, Bharat et al. (Oct. 1995). "Functional connectivity in the motor cortex of resting human brain using echo-planar mri". In: *Magnetic Resonance in Medicine* 34.4, pp. 537–541. ISSN: 07403194, 15222594. DOI: 10.1002/mrm.1910340409.

Biswal, Bharat B., Joel Van Kylen, and James S. Hyde (June 1997). "Simultaneous assessment of flow and BOLD signals in resting-state functional connectivity maps". In: *NMR in Biomedicine* 10.4, pp. 165–170. ISSN: 0952-3480, 1099-1492. DOI: 10.1002/(SICI)1099-1492(199706/08)10:4/5<165::AID-NBM454>3.0.CO;2-7.

Blondel, Vincent D et al. (Oct. 9, 2008). "Fast unfolding of communities in large networks". In: *Journal of Statistical Mechanics: Theory and Experiment* 2008.10, P10008. ISSN: 1742-5468. DOI: 10.1088/1742-5468/2008/10/P10008.

Bojak, Ingo et al. (June 2010). "Connecting Mean Field Models of Neural Activity to EEG and fMRI Data". In: *Brain Topography* 23.2, pp. 139–149. ISSN: 0896-0267, 1573-6792. DOI: 10.1007/s10548-010-0140-3.

Breakspear, Michael (Mar. 2017). "Dynamic models of large-scale brain activity". In: *Nature Neuroscience* 20.3, pp. 340–352. ISSN: 1097-6256, 1546-1726. DOI: 10.1038/nn.4497.

Brown, Timothy J. et al. (Nov. 1, 2016). "Association of the Extent of Resection With Survival in Glioblastoma: A Systematic Review and Meta-analysis". In: *JAMA Oncology* 2.11, p. 1460. ISSN: 2374-2437. DOI: 10.1001/jamaoncol.2016.1373.

Bruce L. Bowermann, Richard T O'Connel (1990). *Linear statistical models: An applied approach.* 2nd ed. Belmond (Calif.): Duxbury Press.

Bullmore, Ed and Olaf Sporns (Mar. 2009). "Complex brain networks: graph theoretical analysis of structural and functional systems". In: *Nature Reviews Neuroscience* 10.3, pp. 186–198. ISSN: 1471-003X, 1471-0048. DOI: 10.1038/nrn2575.

Cabral, Joana et al. (Dec. 2017). "Cognitive performance in healthy older adults relates to spontaneous switching between states of functional connectivity during rest". In: *Scientific Reports* 7.1, p. 5135. ISSN: 2045-2322. DOI: 10.1038/s41598-017-05425-7.

Calhoun, V.D. et al. (Nov. 2001). "A method for making group inferences from functional MRI data using independent component analysis". In: *Human Brain Mapping* 14.3, pp. 140–151. ISSN: 1065-9471, 1097-0193. DOI: 10.1002/hbm.1048.

Calhoun, Vince D. et al. (Oct. 2014). "The Chronnectome: Time-Varying Connectivity Networks as the Next Frontier in fMRI Data Discovery". In: *Neuron* 84.2, pp. 262–274. ISSN: 08966273. DOI: 10.1016/j.neuron.2014.10.015.

Cao, Bolin (2019). "Abnormal dynamic properties of functional connectivity in disorders of consciousness". In: p. 12.

Castellano, Antonella et al. (Oct. 2017). "Functional MRI for Surgery of Gliomas". In: *Current Treatment Options in Neurology* 19.10, p. 34. ISSN: 1092-8480, 1534-3138. DOI: 10.1007/s11940-017-0469-y.

Chan, Micaela Y. et al. (Nov. 18, 2014). "Decreased segregation of brain systems across the healthy adult lifespan". In: *Proceedings of the National Academy of Sciences* 111.46, E4997–E5006. ISSN: 0027-8424, 1091-6490. DOI: 10.1073/pnas.1415122111.

Chang, Catie and Gary H. Glover (Mar. 2010). "Time–frequency dynamics of resting-state brain connectivity measured with fMRI". In: *NeuroImage* 50.1, pp. 81–98. ISSN: 10538119. DOI: 10.1016/j.neuroimage.2009.12.011.

Chee, Michael W.L. et al. (1999). "Auditory and visual word processing studied with fMRI". In: *Human Brain Mapping* 7.1, pp. 15–28. ISSN: 1065-9471, 1097-0193. DOI: 10.1002/(SICI)1097-0193(1999)7:1<15::AID-HBM2>3.0.CO;2-6.

Chen, Yuanyuan et al. (Jan. 4, 2019). "The Transitions Between Dynamic Micro-States Reveal Age-Related Functional Network Reorganization". In: *Frontiers in Physiology* 9, p. 1852. ISSN: 1664-042X. DOI: 10.3389/fphys.2018.01852.

Cherubini, Andrea et al. (Oct. 2009). "Aging of subcortical nuclei: Microstructural, mineralization and atrophy modifications measured in vivo using MRI". In: *NeuroImage* 48.1, pp. 29–36. ISSN: 10538119. DOI: 10.1016/j.neuroimage.2009.06.035.

Chong, Joanna Su Xian et al. (July 10, 2019). "Longitudinal Changes in the Cerebral Cortex Functional Organization of Healthy Elderly". In: *The Journal of Neuroscience* 39.28, pp. 5534–5550. ISSN: 0270-6474, 1529-2401. DOI: 10.1523/JNEUROSCI.1451-18.2019.

Cordes, Dietmar, Vic Haughton, et al. (May 2002). "Hierarchical clustering to measure connectivity in fMRI resting-state data". In: *Magnetic Resonance Imaging* 20.4, pp. 305–317. ISSN: 0730725X. DOI: 10.1016/S0730-725X(02)00503-9.

Cordes, Dietmar, Victor M Haughton, et al. (2000). "Mapping Functionally Related Regions of Brain with Functional Connectivity MR Imaging". In: p. 9.

Crittenden, Ben M, Daniel J Mitchell, and John Duncan (Apr. 13, 2015). "Recruitment of the default mode network during a demanding act of executive control". In: *eLife* 4, e06481. ISSN: 2050-084X. DOI: 10.7554/eLife.06481.

d'Ambrosio, Alessandro et al. (Apr. 2020). "Reduced dynamics of functional connectivity and cognitive impairment in multiple sclerosis". In: *Multiple Sclerosis Journal* 26.4, pp. 476–488. ISSN: 1352-4585, 1477-0970. DOI: 10.1177/1352458519837707.

Dagli, Mandeep S., John E. Ingeholm, and James V. Haxby (Apr. 1999). "Localization of Cardiac-Induced Signal Change in fMRI". In: *NeuroImage* 9.4, pp. 407–415. ISSN: 10538119. DOI: 10.1006/nimg.1998.0424.

Damaraju, E et al. (2014). "Dynamic functional connectivity analysis reveals transient states of dysconnectivity in schizophrenia". In: p. 11.

Damoiseaux, J. S. et al. (Sept. 12, 2006). "Consistent resting-state networks across healthy subjects". In: *Proceedings of the National Academy of Sciences* 103.37, pp. 13848–13853. ISSN: 0027-8424, 1091-6490. DOI: 10.1073/pnas.0601417103.

Damoiseaux, J.S. et al. (Aug. 2008). "Reduced resting-state brain activity in the "default network" in normal aging". In: *Cerebral Cortex* 18.8, pp. 1856–1864. ISSN: 1460-2199, 1047-3211. DOI: 10.1093/cercor/bhm207.

Damoiseaux, Jessica S. (Oct. 2017). "Effects of aging on functional and structural brain connectivity". In: *NeuroImage* 160, pp. 32–40. ISSN: 10538119. DOI: 10.1016/j.neuroimage.2017.01.077.

Daneault, Véronique (2021). "Cerebral functional networks during sleep in young and older individuals". In: *Scientific Reports*, p. 12.

De Baene, Wouter, Geert-Jan M. Rutten, and Margriet M. Sitskoorn (Dec. 2019). "Cognitive functioning in glioma patients is related to functional connectivity measures of the non-tumoural hemisphere". In: *European Journal of Neuroscience* 50.12, pp. 3921–3933. ISSN: 0953-816X, 1460-9568. DOI: 10.1111/ejn.14535.

Deco, Gustavo et al. (Aug. 29, 2008). "The Dynamic Brain: From Spiking Neurons to Neural Masses and Cortical Fields". In: *PLoS Computational Biology* 4.8. Ed. by Olaf Sporns, e1000092. ISSN: 1553-7358. DOI: 10.1371/journal.pcbi.1000092.

Díez-Cirarda, María et al. (2018). "Dynamic functional connectivity in Parkinson's disease patients with mild cognitive impairment and normal cognition". In: *NeuroImage: Clinical* 17, pp. 847–855. ISSN: 22131582. DOI: 10.1016/j.nicl.2017.12.013.

Ding, Ju-Rong et al. (Apr. 2019). "Presurgical localization and spatial shift of resting state networks in patients with brain metastases". In: *Brain Imaging and Behavior* 13.2, pp. 408–420. ISSN: 1931-7557, 1931-7565. DOI: 10.1007/s11682-018-9864-6.

Doshi, Jimit et al. (Dec. 2013). "Multi-Atlas Skull-Stripping". In: *Academic Radiology* 20.12, pp. 1566–1576. ISSN: 10766332. DOI: 10.1016/j.acra.2013.09.010.

Du, Yuhui and Yong Fan (Apr. 2013). "Group information guided ICA for fMRI data analysis". In: *NeuroImage* 69, pp. 157–197. ISSN: 10538119. DOI: 10.1016/j.neuroimage.2012.11.008.

Esposito, Roberto et al. (July 9, 2012). "Modifications of Default-Mode Network Connectivity in Patients with Cerebral Glioma". In: *PLoS ONE* 7.7. Ed. by Yu-Feng Zang, e40231. ISSN: 1932-6203. DOI: 10.1371/journal.pone.0040231.

Essayed, Walid I. et al. (2017). "White matter tractography for neurosurgical planning: A topography-based review of the current state of the art". In: *NeuroImage: Clinical* 15, pp. 659–672. ISSN: 22131582. DOI: 10.1016/j.nicl.2017.06.011.

Ferreira, Luiz Kobuti (2013). "Resting-state functional connectivity in normal brain aging". In: *Neuroscience and Biobehavioral Reviews*, p. 17.

Ferrer, Valéria Pereira, Vivaldo Moura Neto, and Rolf Mentlein (Aug. 2018). "Glioma infiltration and extracellular matrix: key players and modulators". In: *Glia* 66.8, pp. 1542–1565. ISSN: 08941491. DOI: 10.1002/glia.23309.

Fonov, Vladimir et al. (Jan. 2011). "Unbiased average age-appropriate atlases for pediatric studies". In: *NeuroImage* 54.1, pp. 313–327. ISSN: 10538119. DOI: 10.1016/j.neuroimage.2010.07.033.

Fornito, Alex, Andrew Zalesky, and Michael Breakspear (Mar. 2015). "The connectomics of brain disorders". In: *Nature Reviews Neuroscience* 16.3, pp. 159–172. ISSN: 1471-003X, 1471-0048. DOI: 10.1038/nrn3901.

Fox, M. D. et al. (June 27, 2006). "Spontaneous neuronal activity distinguishes human dorsal and ventral attention systems". In: *Proceedings of the National Academy of Sciences* 103.26, pp. 10046–10051. ISSN: 0027-8424, 1091-6490. DOI: 10.1073/pnas.0604187103.

Fox, Michelle E. and Tricia Z. King (Sept. 2018). "Functional Connectivity in Adult Brain Tumor Patients: A Systematic Review". In: *Brain Connectivity* 8.7, pp. 381–397. ISSN: 2158-0014, 2158-0022. DOI: 10.1089/brain.2018.0623.

Fransson, Peter (Sept. 2005). "Spontaneous low-frequency BOLD signal fluctuations: An fMRI investigation of the resting-state default mode of brain function hypothesis". In: *Human Brain Mapping* 26.1, pp. 15–29. ISSN: 1065-9471, 1097-0193. DOI: 10.1002/hbm.20113.

Friston, K. J. et al. (Jan. 1993). "Functional Connectivity: The Principal-Component Analysis of Large (PET) Data Sets". In: *Journal of Cerebral Blood Flow & Metabolism* 13.1, pp. 5–14. ISSN: 0271-678X, 1559-7016. DOI: 10.1038/jcbfm.1993.4.

Friston, Karl J. (Jan. 2011). "Functional and Effective Connectivity: A Review". In: *Brain Connectivity* 1.1, pp. 13–36. ISSN: 2158-0014, 2158-0022. DOI: 10.1089/brain.2011.0008.

Geerligs, Linda et al. (July 2015). "A Brain-Wide Study of Age-Related Changes in Functional Connectivity". In: *Cerebral Cortex* 25.7, pp. 1987–1999. ISSN: 1460-2199, 1047-3211. DOI: 10.1093/cercor/bhu012.

Ghinda, Diana C. et al. (Jan. 2018). "How much is enough—Can resting state fMRI provide a demarcation for neurosurgical resection in glioma?" In: *Neuroscience & Biobehavioral Reviews* 84, pp. 245–261. ISSN: 01497634. DOI: 10.1016/j.neubiorev.2017.11.019.

Ghumman, Sukhmanjit et al. (July 2016). "Exploratory study of the effect of brain tumors on the default mode network". In: *Journal of Neuro-Oncology*

128.3, pp. 437–444. ISSN: 0167-594X, 1573-7373. DOI: 10.1007/s11060-016-2129-6.

Gillespie, Shawn and Michelle Monje (Sept. 3, 2018). "An active role for neurons in glioma progression: making sense of Scherer's structures". In: *Neuro-Oncology* 20.10, pp. 1292–1299. ISSN: 1522-8517, 1523-5866. DOI: 10.1093/neuonc/noy083.

Gleichgerrcht, Ezequiel et al. (2017). "Connectome-based lesion-symptom mapping (CLSM): A novel approach to map neurological function". In: *NeuroImage: Clinical* 16, pp. 461–467. ISSN: 22131582. DOI: 10.1016/j.nicl.2017.08.018.

Golland, Yulia et al. (2008). "Data-driven clustering reveals a fundamental subdivision of the human cortex into two global systems". In: *Neuropsychologia* 46.2, pp. 540–553. ISSN: 00283932. DOI: 10.1016/j.neuropsychologia.2007.10.003.

Golos, Mathieu, Viktor Jirsa, and Emmanuel Daucé (Dec. 28, 2015). "Multistability in Large Scale Models of Brain Activity". In: *PLOS Computational Biology* 11.12. Ed. by Christopher J Honey, e1004644. ISSN: 1553-7358. DOI: 10.1371/journal.pcbi.1004644.

Gonzalez-Castillo, Javier et al. (July 14, 2015). "Tracking ongoing cognition in individuals using brief, whole-brain functional connectivity patterns". In: *Proceedings of the National Academy of Sciences* 112.28, pp. 8762–8767. ISSN: 0027-8424, 1091-6490. DOI: 10.1073/pnas.1501242112.

Gordon, Evan M. et al. (Jan. 2016). "Generation and Evaluation of a Cortical Area Parcellation from Resting-State Correlations". In: *Cerebral Cortex* 26.1, pp. 288–303. ISSN: 1047-3211, 1460-2199. DOI: 10.1093/cercor/bhu239.

Greicius, M. D. et al. (Jan. 7, 2003). "Functional connectivity in the resting brain: A network analysis of the default mode hypothesis". In: *Proceedings of the National Academy of Sciences* 100.1, pp. 253–258. ISSN: 0027-8424, 1091-6490. DOI: 10.1073/pnas.0135058100.

Greve, Douglas N. and Bruce Fischl (Oct. 2009). "Accurate and robust brain image alignment using boundary-based registration". In: *NeuroImage* 48.1, pp. 63–72. ISSN: 10538119. DOI: 10.1016/j.neuroimage.2009.06.060.

Griffanti, Ludovica et al. (July 2014). "ICA-based artefact removal and accelerated fMRI acquisition for improved resting state network imaging". In: *NeuroImage* 95, pp. 232–247. ISSN: 10538119. DOI: 10.1016/j.neuroimage.2014.03.034.

Gu, Yameng, Feng Han, and Xiao Liu (Nov. 5, 2019). "Arousal Contributions to Resting-State fMRI Connectivity and Dynamics". In: *Frontiers in Neuroscience* 13, p. 1190. ISSN: 1662-453X. DOI: 10.3389/fnins.2019.01190.

Hacker, Carl D. et al. (Dec. 2019). "Resting-state network mapping in neurosurgical practice: a review". In: *Neurosurgical Focus* 47.6, E15. ISSN: 1092-0684. DOI: 10.3171/2019.9.FOCUS19656.

Harris, Robert J. et al. (Jan. 2014). "Altered functional connectivity of the default mode network in diffuse gliomas measured with pseudo-resting state fMRI". In: *Journal of Neuro-Oncology* 116.2, pp. 373–379. ISSN: 0167-594X, 1573-7373. DOI: 10.1007/s11060-013-1304-2.

Hart, Michael G., Stephen J. Price, and John Suckling (Sept. 2, 2016). "Connectome analysis for pre-operative brain mapping in neurosurgery". In: *British Journal of Neurosurgery* 30.5, pp. 506–517. ISSN: 0268-8697, 1360-046X. DOI: 10.1080/02688697.2016.1208809.

Heitmann, Stewart and Michael Breakspear (June 2018). "Putting the "dynamic" back into dynamic functional connectivity". In: *Network Neuroscience* 2.2, pp. 150–174. ISSN: 2472-1751. DOI: 10.1162/netn_a_00041.

Heuvel, M. van den et al. (Oct. 22, 2008). "Microstructural Organization of the Cingulum Tract and the Level of Default Mode Functional Connectivity". In: *Journal of Neuroscience* 28.43, pp. 10844–10851. ISSN: 0270-6474, 1529-2401. DOI: 10.1523/JNEUROSCI.2964-08.2008.

Heuvel, Martijn van den, Rene Mandl, and Hilleke Hulshoff Pol (Apr. 23, 2008). "Normalized Cut Group Clustering of Resting-State fMRI Data". In: *PLoS ONE* 3.4. Ed. by Björn Brembs, e2001. ISSN: 1932-6203. DOI: 10.1371/journal.pone.0002001.

Heuvel, Martijn P. van den and Hilleke E. Hulshoff Pol (Aug. 2010). "Exploring the brain network: A review on resting-state fMRI functional connectivity". In: *European Neuropsychopharmacology* 20.8, pp. 519–534. ISSN: 0924977X. DOI: 10.1016/j.euroneuro.2010.03.008.

Himberg, Johan, Aapo Hyvärinen, and Fabrizio Esposito (July 2004). "Validating the independent components of neuroimaging time series via clustering and visualization". In: *NeuroImage* 22.3, pp. 1214–1222. ISSN: 10538119. DOI: 10.1016/j.neuroimage.2004.03.027.

Hutchison, R Matthew et al. (2013). "Dynamic functional connectivity: Promise, issues, and interpretations". In: p. 43.

Hutchison, R. Matthew et al. (Dec. 2014). "Isoflurane induces dose-dependent alterations in the cortical connectivity profiles and dynamic properties of the brain's functional architecture: Dose-Dependent Isoflurane Effects". In: *Human Brain Mapping* 35.12, pp. 5754–5775. ISSN: 10659471. DOI: 10.1002/hbm.22583.

Jenkinson, Mark et al. (Oct. 2002). "Improved Optimization for the Robust and Accurate Linear Registration and Motion Correction of Brain Images". In:

NeuroImage 17.2, pp. 825–841. ISSN: 10538119. DOI: 10.1006/nimg.2002.1132.

Jo, Hang Joon et al. (2013). "Effective Preprocessing Procedures Virtually Eliminate Distance-Dependent Motion Artifacts in Resting State FMRI". In: *Journal of Applied Mathematics* 2013, pp. 1–9. ISSN: 1110-757X, 1687-0042. DOI: 10.1155/2013/935154.

Jones, David T. et al. (June 28, 2012). "Non-Stationarity in the "Resting Brain's" Modular Architecture". In: *PLoS ONE* 7.6. Ed. by Yong He, e39731. ISSN: 1932-6203. DOI: 10.1371/journal.pone.0039731.

Jütten, Kerstin et al. (Nov. 2020). "Asymmetric tumor-related alterations of network-specific intrinsic functional connectivity in glioma patients". In: *Human Brain Mapping* 41.16, pp. 4549–4561. ISSN: 1065-9471, 1097-0193. DOI: 10.1002/hbm.25140.

Kessel, Emma van et al. (Apr. 2021). "Cognitive impairments are independently associated with shorter survival in diffuse glioma patients". In: *Journal of Neurology* 268.4, pp. 1434–1442. ISSN: 0340-5354, 1432-1459. DOI: 10.1007/s00415-020-10303-w.

Kiviniemi, Vesa et al. (June 2003). "Independent component analysis of non-deterministic fMRI signal sources". In: *NeuroImage* 19.2, pp. 253–260. ISSN: 10538119. DOI: 10.1016/S1053-8119(03)00097-1.

Klein, Martin, Hugues Duffau, and Philip C. De Witt Hamer (June 2012). "Cognition and resective surgery for diffuse infiltrative glioma: an overview". In: *Journal of Neuro-Oncology* 108.2, pp. 309–318. ISSN: 0167-594X, 1573-7373. DOI: 10.1007/s11060-012-0811-x.

Koch, Walter et al. (Mar. 2012). "Diagnostic power of default mode network resting state fMRI in the detection of Alzheimer's disease". In: *Neurobiology of Aging* 33.3, pp. 466–478. ISSN: 01974580. DOI: 10.1016/j.neurobiolaging.2010.04.013.

Kocher, Martin et al. (2020). "Role of the default mode resting-state network for cognitive functioning in malignant glioma patients following multimodal treatment". In: *NeuroImage: Clinical* 27, p. 102287. ISSN: 22131582. DOI: 10.1016/j.nicl.2020.102287.

Kottaram, Akhil et al. (May 2019). "Brain network dynamics in schizophrenia: Reduced dynamism of the default mode network". In: *Human Brain Mapping* 40.7, pp. 2212–2228. ISSN: 1065-9471, 1097-0193. DOI: 10.1002/hbm.24519.

Kreth, F. -W. et al. (Dec. 2013). "Gross total but not incomplete resection of glioblastoma prolongs survival in the era of radiochemotherapy". In: *Annals of Oncology* 24.12, pp. 3117–3123. ISSN: 09237534. DOI: 10.1093/annonc/mdt388.

Kucyi, A., T. V. Salomons, and K. D. Davis (Nov. 12, 2013). "Mind wandering away from pain dynamically engages antinociceptive and default mode brain networks". In: *Proceedings of the National Academy of Sciences* 110.46, pp. 18692–18697. ISSN: 0027-8424, 1091-6490. DOI: 10.1073/pnas.1312902110.

Kwong, K. K. et al. (June 15, 1992). "Dynamic magnetic resonance imaging of human brain activity during primary sensory stimulation." In: *Proceedings of the National Academy of Sciences* 89.12, pp. 5675–5679. ISSN: 0027-8424, 1091-6490. DOI: 10.1073/pnas.89.12.5675.

LaBar, Kevin S. et al. (Dec. 1999). "Neuroanatomic Overlap of Working Memory and Spatial Attention Networks: A Functional MRI Comparison within Subjects". In: *NeuroImage* 10.6, pp. 695–704. ISSN: 10538119. DOI: 10.1006/nimg.1999.0503.

Lapointe, Sarah, Arie Perry, and Nicholas A Butowski (Aug. 2018). "Primary brain tumours in adults". In: *The Lancet* 392.10145, pp. 432–446. ISSN: 01406736. DOI: 10.1016/S0140-6736(18)30990-5.

Lee, M.H., C.D. Smyser, and J.S. Shimony (Oct. 2013). "Resting-State fMRI: A Review of Methods and Clinical Applications". In: *American Journal of Neuroradiology* 34.10, pp. 1866–1872. ISSN: 0195-6108, 1936-959X. DOI: 10.3174/ajnr.A3263.

Lee, Megan H. et al. (Feb. 2016). "Clinical Resting-state fMRI in the Preoperative Setting: Are We Ready for Prime Time?" In: *Topics in Magnetic Resonance Imaging* 25.1, pp. 11–18. ISSN: 0899-3459. DOI: 10.1097/RMR.0000000000000075.

Legéndy, C. R. (Jan. 1975). "Three Principles of Brain Function and Structure". In: *International Journal of Neuroscience* 6.5, pp. 237–254. ISSN: 0020-7454, 1543-5245. DOI: 10.3109/00207457509149497.

Lent, Roberto et al. (Jan. 2012). "How many neurons do you have? Some dogmas of quantitative neuroscience under revision: Neuroscience dogmas and brain cell numbers". In: *European Journal of Neuroscience* 35.1, pp. 1–9. ISSN: 0953816X. DOI: 10.1111/j.1460-9568.2011.07923.x.

Leonardi, Nora and Dimitri Van De Ville (Jan. 2015). "On spurious and real fluctuations of dynamic functional connectivity during rest". In: *NeuroImage* 104, pp. 430–436. ISSN: 10538119. DOI: 10.1016/j.neuroimage.2014.09.007.

Logothetis, Nikos K et al. (2001). "Neurophysiological investigation of the basis of the fMRI signal". In: 412, p. 8.

Lowe, Mark J. et al. (Nov. 2000). "Correlations in Low-Frequency BOLD Fluctuations Reflect Cortico-Cortical Connections". In: *NeuroImage* 12.5, pp. 582–587. ISSN: 10538119. DOI: 10.1006/nimg.2000.0654.

Lurie, Daniel J. et al. (Jan. 2020). "Questions and controversies in the study of time-varying functional connectivity in resting fMRI". In: *Network Neuroscience* 4.1, pp. 30–69. ISSN: 2472-1751. DOI: 10.1162/netn_a_00116.

Lv, H. et al. (Jan. 18, 2018). "Resting-State Functional MRI: Everything That Nonexperts Have Always Wanted to Know". In: *American Journal of Neuroradiology*, ajnr, ajnr.A5527v1. ISSN: 0195-6108, 1936-959X. DOI: 10.3174/ajnr.A5527.

Maesawa, Satoshi et al. (Feb. 6, 2015). "Evaluation of Resting State Networks in Patients with Gliomas: Connectivity Changes in the Unaffected Side and Its Relation to Cognitive Function". In: *PLOS ONE* 10.2. Ed. by Yu-Feng Zang, e0118072. ISSN: 1932-6203. DOI: 10.1371/journal.pone.0118072.

Malagurski, Brigitta et al. (Dec. 2020). "Longitudinal functional brain network reconfiguration in healthy aging". In: *Human Brain Mapping* 41.17, pp. 4829–4845. ISSN: 1065-9471, 1097-0193. DOI: 10.1002/hbm.25161.

Mayford, M., S. A. Siegelbaum, and E. R. Kandel (June 1, 2012). "Synapses and Memory Storage". In: *Cold Spring Harbor Perspectives in Biology* 4.6, a005751–a005751. ISSN: 1943-0264. DOI: 10.1101/cshperspect.a005751.

McConnell, Heather L. et al. (Jan. 2017). "The Translational Significance of the Neurovascular Unit". In: *Journal of Biological Chemistry* 292.3, pp. 762–770. ISSN: 00219258. DOI: 10.1074/jbc.R116.760215.

Mendes, Natacha et al. (Mar. 2019). "A functional connectome phenotyping dataset including cognitive state and personality measures". In: *Scientific Data* 6.1, p. 180307. ISSN: 2052-4463. DOI: 10.1038/sdata.2018.307.

Meyers, Christina A. et al. (Feb. 1, 2000). "Cognitive Function as a Predictor of Survival in Patients With Recurrent Malignant Glioma". In: *Journal of Clinical Oncology* 18.3, pp. 646–646. ISSN: 0732-183X, 1527-7755. DOI: 10.1200/JCO.2000.18.3.646.

Munck, J.C. de et al. (Aug. 2008). "A study of the brain's resting state based on alpha band power, heart rate and fMRI". In: *NeuroImage* 42.1, pp. 112–121. ISSN: 10538119. DOI: 10.1016/j.neuroimage.2008.04.244.

Munkres, James (Mar. 1957). "Algorithms for Assignment and Transportation Problems". In: Number 1 5.

Nenning, Karl-Heinz et al. (Dec. 2020). "Distributed changes of the functional connectome in patients with glioblastoma". In: *Scientific Reports* 10.1, p. 18312. ISSN: 2045-2322. DOI: 10.1038/s41598-020-74726-1.

Ogawa, S. et al. (Dec. 1, 1990). "Brain magnetic resonance imaging with contrast dependent on blood oxygenation." In: *Proceedings of the National Academy of Sciences* 87.24, pp. 9868–9872. ISSN: 0027-8424, 1091-6490. DOI: 10.1073/pnas.87.24.9868.

Palomero-Gallagher, Nicola and Karl Zilles (2018). "Cyto- and receptor architectonic mapping of the human brain". In: *Handbook of Clinical Neurology*. Vol. 150. Elsevier, pp. 355–387. ISBN: 978-0-444-63639-3. DOI: 10.1016/B978-0-444-63639-3.00024-4.

Pedersen, Mangor et al. (Nov. 2018). "On the relationship between instantaneous phase synchrony and correlation-based sliding windows for time-resolved fMRI connectivity analysis". In: *NeuroImage* 181, pp. 85–94. ISSN: 10538119. DOI: 10.1016/j.neuroimage.2018.06.020.

Pillai, J.J. (Feb. 2010). "The Evolution of Clinical Functional Imaging during the Past 2 Decades and Its Current Impact on Neurosurgical Planning". In: *American Journal of Neuroradiology* 31.2, pp. 219–225. ISSN: 0195-6108, 1936-959X. DOI: 10.3174/ajnr.A1845.

Power, Jonathan D. et al. (Feb. 2012). "Spurious but systematic correlations in functional connectivity MRI networks arise from subject motion". In: *NeuroImage* 59.3, pp. 2142–2154. ISSN: 10538119. DOI: 10.1016/j.neuroimage.2011.10.018.

Preti, Maria Giulia, Thomas AW Bolton, and Dimitri Van De Ville (Oct. 2017). "The dynamic functional connectome: State-of-the-art and perspectives". In: *NeuroImage* 160, pp. 41–54. ISSN: 10538119. DOI: 10.1016/j.neuroimage.2016.12.061.

Rabiner, L.R. (Feb. 1989). "A tutorial on hidden Markov models and selected applications in speech recognition". In: *Proceedings of the IEEE* 77.2, pp. 257–286. ISSN: 00189219. DOI: 10.1109/5.18626.

Raichle, M. E. et al. (Jan. 16, 2001). "A default mode of brain function". In: *Proceedings of the National Academy of Sciences* 98.2, pp. 676–682. ISSN: 0027-8424, 1091-6490. DOI: 10.1073/pnas.98.2.676.

Rashid, Barnaly, Laura M. E. Blanken, et al. (Aug. 2018). "Connectivity dynamics in typical development and its relationship to autistic traits and autism spectrum disorder". In: *Human Brain Mapping* 39.8, pp. 3127–3142. ISSN: 10659471. DOI: 10.1002/hbm.24064.

Rashid, Barnaly, Eswar Damaraju, et al. (Nov. 7, 2014). "Dynamic connectivity states estimated from resting fMRI Identify differences among Schizophrenia, bipolar disorder, and healthy control subjects". In: *Frontiers in Human Neuroscience* 8. ISSN: 1662-5161. DOI: 10.3389/fnhum.2014.00897.

Rezek, Iead and Stephen Roberts (2005). "Ensemble Hidden Markov Models with Extended Observation Densities for Biosignal Analysis". In: *Probabilistic Modeling in Bioinformatics and Medical Informatics*. Ed. by Dirk Husmeier, Richard Dybowski, and Stephen Roberts. Series Title: Advanced Information and Knowledge Processing. London: Springer-Verlag, pp. 419–450. ISBN: 978-1-85233-778-0. DOI: 10.1007/1-84628-119-9_14.

Rousseeuw, Peter J. (Nov. 1987). "Silhouettes: A graphical aid to the interpretation and validation of cluster analysis". In: *Journal of Computational and Applied Mathematics* 20, pp. 53–65. ISSN: 03770427. DOI: 10.1016/0377-0427(87)90125-7.

Rubinov, Mikail and Olaf Sporns (Sept. 2010). "Complex network measures of brain connectivity: Uses and interpretations". In: *NeuroImage* 52.3, pp. 1059–1069. ISSN: 10538119. DOI: 10.1016/j.neuroimage.2009.10.003.

Saha, Debbrata K. et al. (June 25, 2020). *A classification-based approach to estimate the number of resting fMRI dynamic functional connectivity states*. preprint. Neuroscience. DOI: 10.1101/2020.06.24.161745.

Sair, Haris I. et al. (Mar. 2016). "Presurgical brain mapping of the language network in patients with brain tumors using resting-state f MRI : Comparison with task f MRI". In: *Human Brain Mapping* 37.3, pp. 913–923. ISSN: 1065-9471, 1097-0193. DOI: 10.1002/hbm.23075.

Sakoğlu, Ünal et al. (Dec. 2010). "A method for evaluating dynamic functional network connectivity and task-modulation: application to schizophrenia". In: *Magnetic Resonance Materials in Physics, Biology and Medicine* 23.5, pp. 351–366. ISSN: 0968-5243, 1352-8661. DOI: 10.1007/s10334-010-0197-8.

Salimi-Khorshidi, Gholamreza et al. (Apr. 2014). "Automatic denoising of functional MRI data: Combining independent component analysis and hierarchical fusion of classifiers". In: *NeuroImage* 90, pp. 449–468. ISSN: 10538119. DOI: 10.1016/j.neuroimage.2013.11.046.

Salman, Mustafa S. et al. (2019). "Group ICA for identifying biomarkers in schizophrenia: 'Adaptive' networks via spatially constrained ICA show more sensitivity to group differences than spatio-temporal regression". In: *NeuroImage: Clinical* 22, p. 101747. ISSN: 22131582. DOI: 10.1016/j.nicl.2019.101747.

Salvador, Raymond et al. (Sept. 1, 2005). "Neurophysiological Architecture of Functional Magnetic Resonance Images of Human Brain". In: *Cerebral Cortex* 15.9, pp. 1332–1342. ISSN: 1460-2199, 1047-3211. DOI: 10.1093/cercor/bhi016.

Schlosser, R et al. (Apr. 1, 1998). "Functional magnetic resonance imaging of human brain activity in a verbal fluency task". In: *Journal of Neurology, Neurosurgery & Psychiatry* 64.4, pp. 492–498. ISSN: 0022-3050. DOI: 10.1136/jnnp.64.4.492.

Schneider, F.C. et al. (Jan. 2016). "Presurgical Assessment of the Sensorimotor Cortex Using Resting-State fMRI". In: *American Journal of Neuroradiology* 37.1, pp. 101–107. ISSN: 0195-6108, 1936-959X. DOI: 10.3174/ajnr.A4472.

Schwarz, Gideon (Mar. 1, 1978). "Estimating the Dimension of a Model". In: *The Annals of Statistics* 6.2. ISSN: 0090-5364. DOI: 10.1214/aos/1176344136.

Shappell, Heather et al. (May 2019). "Improved state change estimation in dynamic functional connectivity using hidden semi-Markov models". In: *NeuroImage* 191, pp. 243–257. ISSN: 10538119. DOI: 10.1016/j.neuroimage.2019.02.013.

Shen, Hui, Zhenfeng Li, et al. (Jan. 2016). "Changes in functional connectivity dynamics associated with vigilance network in taxi drivers". In: *NeuroImage* 124, pp. 367–378. ISSN: 10538119. DOI: 10.1016/j.neuroimage.2015.09.010.

Shen, Hui, Lubin Wang, et al. (Feb. 2010). "Discriminative analysis of resting-state functional connectivity patterns of schizophrenia using low dimensional embedding of fMRI". In: *NeuroImage* 49.4, pp. 3110–3121. ISSN: 10538119. DOI: 10.1016/j.neuroimage.2009.11.011.

Shirer, W. R. et al. (Jan. 2012). "Decoding Subject-Driven Cognitive States with Whole-Brain Connectivity Patterns". In: *Cerebral Cortex* 22.1, pp. 158–165. ISSN: 1460-2199, 1047-3211. DOI: 10.1093/cercor/bhr099.

Siegel, Joshua Sarfaty et al. (July 26, 2016). "Disruptions of network connectivity predict impairment in multiple behavioral domains after stroke". In: *Proceedings of the National Academy of Sciences* 113.30, E4367–E4376. ISSN: 0027-8424, 1091-6490. DOI: 10.1073/pnas.1521083113.

Smith, S. M. et al. (Aug. 4, 2009). "Correspondence of the brain's functional architecture during activation and rest". In: *Proceedings of the National Academy of Sciences* 106.31, pp. 13040–13045. ISSN: 0027-8424, 1091-6490. DOI: 10.1073/pnas.0905267106.

Smith, Stephen M. et al. (Jan. 2004). "Advances in functional and structural MR image analysis and implementation as FSL". In: *NeuroImage* 23, S208–S219. ISSN: 10538119. DOI: 10.1016/j.neuroimage.2004.07.051.

Smith, Verity, Daniel J Mitchell, and John Duncan (Oct. 1, 2018). "Role of the Default Mode Network in Cognitive Transitions". In: *Cerebral Cortex* 28.10, pp. 3685–3696. ISSN: 1047-3211, 1460-2199. DOI: 10.1093/cercor/bhy167.

Song, Jie et al. (Nov. 2014). "Age-Related Reorganizational Changes in Modularity and Functional Connectivity of Human Brain Networks". In: *Brain Connectivity* 4.9, pp. 662–676. ISSN: 2158-0014, 2158-0022. DOI: 10.1089/brain.2014.0286.

Song, Ming et al. (July 2008). "Brain spontaneous functional connectivity and intelligence". In: *NeuroImage* 41.3, pp. 1168–1176. ISSN: 10538119. DOI: 10.1016/j.neuroimage.2008.02.036.

Sporns, Olaf, Christopher J. Honey, and Rolf Kötter (Oct. 17, 2007). "Identification and Classification of Hubs in Brain Networks". In: *PLoS ONE* 2.10.

Ed. by Marcus Kaiser, e1049. ISSN: 1932-6203. DOI: 10.1371/journal.pone.0001049.

Stoecklein, Veit M et al. (Sept. 29, 2020). "Resting-state fMRI detects alterations in whole brain connectivity related to tumor biology in glioma patients". In: *Neuro-Oncology* 22.9, pp. 1388–1398. ISSN: 1522-8517, 1523-5866. DOI: 10.1093/neuonc/noaa044.

Supekar, Kaustubh et al. (June 27, 2008). "Network Analysis of Intrinsic Functional Brain Connectivity in Alzheimer's Disease". In: *PLoS Computational Biology* 4.6. Ed. by Olaf Sporns, e1000100. ISSN: 1553-7358. DOI: 10.1371/journal.pcbi.1000100.

Thirion, Bertrand, Silke Dodel, and Jean-Baptiste Poline (Jan. 2006). "Detection of signal synchronizations in resting-state fMRI datasets". In: *NeuroImage* 29.1, pp. 321–327. ISSN: 10538119. DOI: 10.1016/j.neuroimage.2005.06.054.

Thomas Yeo, B. T. et al. (Sept. 2011). "The organization of the human cerebral cortex estimated by intrinsic functional connectivity". In: *Journal of Neurophysiology* 106.3, pp. 1125–1165. ISSN: 0022-3077, 1522-1598. DOI: 10.1152/jn.00338.2011.

Tian, Lixia et al. (May 2018). "Changes in dynamic functional connections with aging". In: *NeuroImage* 172, pp. 31–39. ISSN: 10538119. DOI: 10.1016/j.neuroimage.2018.01.040.

Tomasi, D and N D Volkow (May 2012). "Aging and functional brain networks". In: *Molecular Psychiatry* 17.5, pp. 549–558. ISSN: 1359-4184, 1476-5578. DOI: 10.1038/mp.2011.81.

Tustison, Nicholas J et al. (June 2010). "N4ITK: Improved N3 Bias Correction". In: *IEEE Transactions on Medical Imaging* 29.6, pp. 1310–1320. ISSN: 0278-0062, 1558-254X. DOI: 10.1109/TMI.2010.2046908.

Uddin, Lucina Q. (Dec. 2013). "Complex relationships between structural and functional brain connectivity". In: *Trends in Cognitive Sciences* 17.12, pp. 600–602. ISSN: 13646613. DOI: 10.1016/j.tics.2013.09.011.

Valsasina, Paola et al. (July 10, 2019). "Characterizing Rapid Fluctuations of Resting State Functional Connectivity in Demyelinating, Neurodegenerative, and Psychiatric Conditions: From Static to Time-Varying Analysis". In: *Frontiers in Neuroscience* 13, p. 618. ISSN: 1662-453X. DOI: 10.3389/fnins.2019.00618.

Van Schependom, Jeroen et al. (Nov. 2019). "Altered transient brain dynamics in multiple sclerosis: Treatment or pathology?" In: *Human Brain Mapping* 40.16, pp. 4789–4800. ISSN: 1065-9471, 1097-0193. DOI: 10.1002/hbm.24737.

Varangis, Eleanna et al. (Sept. 4, 2019). "The Effect of Aging on Resting State Connectivity of Predefined Networks in the Brain". In: *Frontiers in Aging Neuroscience* 11, p. 234. ISSN: 1663-4365. DOI: 10.3389/fnagi.2019.00234.

Ven, Vincent G. van de et al. (July 2004). "Functional connectivity as revealed by spatial independent component analysis of fMRI measurements during rest". In: *Human Brain Mapping* 22.3, pp. 165–178. ISSN: 1065-9471, 1097-0193. DOI: 10.1002/hbm.20022.

Vergara, Victor M. et al. (2018). "Dynamic functional network connectivity discriminates mild traumatic brain injury through machine learning". In: *NeuroImage: Clinical* 19, pp. 30–37. ISSN: 22131582. DOI: 10.1016/j.nicl.2018.03.017.

Vidaurre, Diego, Romesh Abeysuriya, et al. (Oct. 2018). "Discovering dynamic brain networks from big data in rest and task". In: *NeuroImage* 180, pp. 646–656. ISSN: 10538119. DOI: 10.1016/j.neuroimage.2017.06.077.

Vidaurre, Diego, Andrew J. Quinn, et al. (Feb. 2016). "Spectrally resolved fast transient brain states in electrophysiological data". In: *NeuroImage* 126, pp. 81–95. ISSN: 10538119. DOI: 10.1016/j.neuroimage.2015.11.047.

Vidaurre, Diego, Stephen M. Smith, and Mark W. Woolrich (Nov. 28, 2017). "Brain network dynamics are hierarchically organized in time". In: *Proceedings of the National Academy of Sciences* 114.48, pp. 12827–12832. ISSN: 0027-8424, 1091-6490. DOI: 10.1073/pnas.1705120114.

Viterbi, A. J. (1967). "Error Bounds for Convolutional Codes and an Asymptotically Optimum Decoding Algorithm". In: *IEEE Transactions of Information Theory* 13, pp. 260–269.

Volz, Lukas J. et al. (Sept. 2018). "Functional magnetic resonance imaging in glioma patients: from clinical applications to future perspectives". In: *The Quarterly Journal of Nuclear Medicine and Molecular Imaging* 62.3. ISSN: 18244785, 18271936. DOI: 10.23736/S1824-4785.18.03101-1.

Wang, Lubin et al. (Aug. 30, 2012). "Decoding Lifespan Changes of the Human Brain Using Resting-State Functional Connectivity MRI". In: *PLoS ONE* 7.8. Ed. by Yu-Feng Zang, e44530. ISSN: 1932-6203. DOI: 10.1371/journal.pone.0044530.

Whitfield-Gabrieli, S. et al. (Jan. 27, 2009). "Hyperactivity and hyperconnectivity of the default network in schizophrenia and in first-degree relatives of persons with schizophrenia". In: *Proceedings of the National Academy of Sciences* 106.4, pp. 1279–1284. ISSN: 0027-8424, 1091-6490. DOI: 10.1073/pnas.0809141106.

Worsley, Keith J et al. (May 29, 2005). "Comparing functional connectivity via thresholding correlations and singular value decomposition". In: *Philosophical*

Transactions of the Royal Society B: Biological Sciences 360.1457, pp. 913–920. ISSN: 0962-8436, 1471-2970. DOI: 10.1098/rstb.2005.1637.

Xia, Liang et al. (Dec. 2018). "Relationship between the extent of resection and the survival of patients with low-grade gliomas: a systematic review and meta-analysis". In: *BMC Cancer* 18.1, p. 48. ISSN: 1471-2407. DOI: 10.1186/s12885-017-3909-x.

Xia, Yunman et al. (Feb. 15, 2019). "Tracking the dynamic functional connectivity structure of the human brain across the adult lifespan". In: *Human Brain Mapping* 40.3, pp. 717–728. ISSN: 1065-9471, 1097-0193. DOI: 10.1002/hbm.24385.

Yaesoubi, Maziar et al. (Oct. 2015). "Dynamic coherence analysis of resting fMRI data to jointly capture state-based phase, frequency, and time-domain information". In: *NeuroImage* 120, pp. 133–142. ISSN: 10538119. DOI: 10.1016/j.neuroimage.2015.07.002.

Yan, Lirong et al. (Nov. 4, 2011). "Loss of Coherence of Low Frequency Fluctuations of BOLD FMRI in Visual Cortex of Healthy Aged Subjects". In: *The Open Neuroimaging Journal* 5 (Suppl 1), pp. 105–111. ISSN: 1874-4400. DOI: 10.2174/1874440001105010105.

Yetkin, F. Zerrin et al. (Jan. 2006). "FMRI of working memory in patients with mild cognitive impairment and probable Alzheimer's disease". In: *European Radiology* 16.1, pp. 193–206. ISSN: 0938-7994, 1432-1084. DOI: 10.1007/s00330-005-2794-x.

Zalesky, Andrew and Michael Breakspear (July 2015). "Towards a statistical test for functional connectivity dynamics". In: *NeuroImage* 114, pp. 466–470. ISSN: 10538119. DOI: 10.1016/j.neuroimage.2015.03.047.

Zanchi, Davide et al. (2017). "Decreased Fronto-Parietal and Increased Default Mode Network Activation is Associated with Subtle Cognitive Deficits in Elderly Controls". In: *Neurosignals* 25.1, pp. 127–138. ISSN: 1424-862X, 1424-8638. DOI: 10.1159/000486152.

Zhang, Dongyang et al. (Dec. 1, 2009). "Preoperative Sensorimotor Mapping in Brain Tumor Patients Using Spontaneous Fluctuations in Neuronal Activity Imaged With Functional Magnetic Resonance Imaging: Initial Experience". In: *Operative Neurosurgery* 65 (suppl_6), ons226–ons236. ISSN: 2332-4252, 2332-4260. DOI: 10.1227/01.NEU.0000350868.95634.CA.

Zonneveld, Hazel I (2019). "Patterns of functional connectivity in an aging population: The Rotterdam Study". In: p. 13.

List of publications

Journals

[P1] Baro, V., Landi, A., Brigadoi, S., Castellaro, M., Moretto, M., Anglani, M., Ermani, M., Causin, F., Zanoletti, E., Denaro, L., Bertoldo, A., d'Avella, D. (2019). "Preoperative Prediction of Facial Nerve in Patients with Vestibular Schwannomas: The Role of Diffusion Tensor Imaging-A Systematic Review". *World neurosurgery*, 125, 24–31.

[P2] Castellaro, M.*, Moretto, M.*, Baro, V., Brigadoi, S., Zanoletti, E., Anglani, M., Denaro, L., Dell'Acqua, R., Landi, A., Causin, F., d'Avella, D., Bertoldo, A. (2020). "Multishell Diffusion MRI-Based Tractography of the Facial Nerve in Vestibular Schwannoma". *AJNR. American journal of neuroradiology*, 41(8), 1480–1486.
*Equally contribution

[P3] Moretto, M., Silvestri, E., Zangrossi, A., Corbetta, M., Bertoldo, A. (2021). "Unveiling whole-brain dynamics in normal aging through Hidden Markov Models". *Human brain mapping*, 2021 Nov 15.

[P4] Silvestri E.*, Villani U.*, Moretto M., Colpo M., Salvalaggio A., Anglani M., Cecchin D., Corbetta M., Bertoldo A. "Assessment of Structural Disconnections in Gliomas: Comparison of Indirect and Direct Approaches".
under review

[P5] Silvestri, E., Moretto M., Facchini, S., Castellaro, M., Anglani, M., Monai, E., D'Avella, D., Della Puppa, A., Cecchin, D., Bertoldo, A., Corbetta M. "Widespread cortical functional disconnection in gliomas: an individual network mapping approach".
under review
*Equally contribution

Conferences

[C1] Moretto, M., Silvestri, E., Corbetta, M., Bertoldo, A. "Whole-brain functional dynamics in normal aging during resting conditions". *BraYn - 4^{th} Brainstorming Research Assembly for Young Neuroscientists*

[C2] Silvestri, E., Moretto, M., Castellaro, M., Facchini, S., Monai, E., d'Avella, D., Della Puppa, A., Cecchin, D., Bertoldo, A., Corbetta, M. "A whole-brain approach to map the individual impact of gliomas on brain functions". *BraYn - 4^{th} Brainstorming Research Assembly for Young Neuroscientists*

[C3] Villani, U., Silvestri, E., Moretto, M., Colpo, M., Salvalaggio, A., Corbetta, M., Bertoldo, A. "Investigating patterns of white matter disconnections in gliomas: a single-subject tractography-based approach". *BraYn - 4^{th} Brainstorming Research Assembly for Young Neuroscientists*

[C4] Moretto, M., Silvestri, E., Castellaro, M., Anglani, M., Facchini, S., Monai, E., d'Avella, D., Della Puppa, A., Cecchin, D., Corbetta, M., Bertoldo, A. "An ICA-based approach to study altered resting state functional networks in brain tumors". *Proc. Intl. Soc. Mag. Reson. Med.* 28 (2020)

[C5] Silvestri, E., Moretto, M., Castellaro, M., Facchini, S., Monai, E., d'Avella, D., Della Puppa, A., Cecchin, D., Bertoldo, A., Corbetta, M. "Whole-Brain Resting-State Mapping to Measure the Effect of Gliomas on Brain Function". (2020), *145^{th} Annual Meeting American Neurological Association. Ann Neurol,* 88: S1-S280.

[C6] Moretto, M., Baro, V., Brigadoi, S., Castellaro, M., Anglani, M., Mazzoni, A., Zanoletti, E., Landi, A., Denaro, L., Causin, F., d'Avella, D., Bertoldo, A. "Optimized DTI acquisition and tractography pipeline for a reliable reconstruction of the facial nerve in patients with vestibular schwannoma". *Proc. Intl. Soc. Mag. Reson. Med.* 27 (2019)

Acknowledgements

During these three years I had the opportunity to work with people who have been a source of inspiration for my research work and who have supported me continuously.
Among them, I would first like to thank Prof. Alessandra Bertoldo for giving me the opportunity to undertake this journey and for her continuous support during these very intense years. Thanks also to Prof. Maurizio Corbetta for the support and the interesting discussion we had together.
A great thank must go to Erica, the biggest source of inspiration for me and my work. Without her I would not be where I am now.
Thanks to my colleagues and friends, Stefano and Umberto, with whom I have shared this journey and to all the 301's guys, Agnese, Danilo, Davide, Edoardo, Giorgia, Ilaria, Marco, Nunzio: I couldn't ask for better colleagues.
The last thank must go to my family for the endless support and, in particular, to Andrea who has always supported me in every choice and believed in me more than I did.
Thanks to everyone else who contributed to the realization of this thesis.
Padova, January 2022.